Effect of Ti doping on Structural, Magnetic and DC/AC Transport properties of $SrFeO_{3-\delta}$

A thesis submitted to

University of Hyderabad

In Partial Fulfillment of the Requirements for the Degree of

Doctor of Philosophy

By

A. SENDILKUMAR

06PHPH02

School of Physics

University of Hyderabad

Hyderabad – 500046

July 2012

Dedicated

To

All My Teachers

DECLARATION

I hereby declare that the work presented in this thesis has been carried out by me under the supervision of Dr. S. Srinath, School of Physics, University of Hyderabad, Hyderabad, India. I also declare that the said work has not been, in part or the whole thereof, submitted to any other University/ institution for the award of any other degree/diploma.

A. SENDILKUMAR

Date:

Place: Hyderabad.

CERTIFICATE

This is to certify that the research work compiled and presented in the thesis titled "**Effect of Ti doping on Structural, Magnetic and DC/AC Transport properties of $SrFeO_{3-\delta}$** " has been carried out by A. Sendilkumar under my supervision and the same has not been submitted for the award of degree by any other University.

Dr. S. SRINATH

RESEARCH SUPERVISOR
Reader, School of Physics
University of Hyderabad

Date:

Place: Hyderabad

DEAN

SCHOOL OF PHYSICS

ACKNOWLEDGMENTS

It gives me an immense pleasure and feeling of satisfaction to express my deep sense of gratitude to my Ph.D. Supervisor Dr. S. Srinath for providing me an opportunity to work with him. It has been a great privilege to work with him as a first Ph.D. student. I thank him for his continuous inspiration, motivation and keen guidance at various stages of my work.

I am grateful to my doctoral committee member Prof. S.N. Kaul for his constant support and encouragement. I feel privileged to be a part of his research group. His help and explanation are greatly acknowledged.

I am thankful to my other doctoral committee members Prof. V. Seshubai, Prof. C. S. Sunandhana and Prof. M. Ghanashyam Krishna for all their valuable suggestions and discussions at various stages of the work.

I thank the Dean of the school Prof. S. P. Tewari and the former deans Prof. C. Bansal and Prof. Vipin Srivastava for extending all the infrastructure and experimental facilities.

I thank Dr. P.D. Babu, IUC-DAE CSR, Mumbai, for Neutron diffraction measurements, for his help in data analysis and useful discussions.

I thank Dr. Alok Banerjee, IUC-DAE CSR, Indore for magnetization measurements, Dr.A.Gupta and Dr.V.R. Reddy , IUC-DAE CSR, Indore

for low temperature Mössbauer measurements and Dr. R. Rawat IUC-DAE, Indore for low temperature transport measurements.

I thank Dr. M. Manivel Raja , DMRL for room temperature Mössbauer measurements and help in data analysis.

I thank Prof. K.C. James Raju for Impedance measurements and useful discussions.

I thank all CIL members at University of Hyderabad for availing the facilities to carry out the measurements and especially Dr. Maqbool Ahmed, Principal Scientific Officer, and the staff members Mr. C. S. Murthy, Dr. Manjunatha Rao and Mr. Pavan.

The help from Mr. Ch. Suresh ,CIL in ESR measurements is greatly acknowledged.

I thank my seniors Dr.A. Basheed and Dr. S. P. Mathew for the help in analyzing the FMR data and other my seniors Dr.Sanjeev Kumar and Dr. Ashutosh Abhyangar.

I thank Prof. A. P. Pathak, former coordinator Centre for Advanced Studies (CAS), School of Physics and CAS staff members Mrs. Shailaja and Mr. Prasad.

I thank Centre for Nanotechnology for extending the PPMS facility.

I thank UGC for the BBL fellowship and UGC-CAS for RFSMS fellowship.

I thank all the staff members at the school office, particularly Mr. Abraham, Mr. Rajaratnam, and Mr. Chanderpal.

I was greatly inspired by Prof. S. R. Shenoy, Prof. S. N. Kaul, Prof. V. S. S. Sastry and Prof. V. Seshubai during the course of my research. I thank all of them for being such wonderful teachers of physics.

I also thank, Prof. Rajender Singh, Prof. G. Rajaram, Dr. James Raju, Dr.V. Nirmal Kumar and Dr. Ashoka Vudayagiri for teaching me various experiments as a part of the experimental techniques course.

I thank Mr. Lakshmi Narayana and Mr. Ravishankar and Mr. Thirumalaiah at the FESEM facility and XRD measurements. I thank my colleagues Mr. Yughandhar Bitla for helping me in various stages and useful discussions, Mr. K. Vasu for teaching AFM technique, Mr. A. Rambabu and Mr. K. Rama Obulesu for Impedance measurements. Mr. D. Sanjeev Kumar and Mr. Sekhar, School of Physics, UOH for their help in various ways is greatly acknowledged.

I thank all the other faculty members of the school of physics for all their help.

I thank my labmate Mr. P. Suersh for his help at all the stages. My other labmates Mr. Ravikumar, Mr. Pavanvenuprakash and Mr. Uma Shankar helped round the clock to carry out magnetization measurements are highly appreciated.

I thank all the fellow research scholars belonging to the 2006 PhD batch and my senior and junior colleagues from the school for all the support and help and especially my friends Mr. R. Parthasarathy for all the encouragement and moral support. I thank my friends Dr. Dr. Paul Joseph, Dr. E.Vishwanathan and Dr.Samba Sivam University of Madras M.Phil batchmates, Dr.K. Praveena PDF in our lab, Dr. Srinivan, School

of Chemistry ,UOH and Mr. Kovendhan, Presidency college, Madras. I thank G. Thirupathi, School of Physics for helping me in various ways.

I would like to take this opportunity to thank my parents, brother, sister, family members and other relatives for their encouragement.

A. Sendilkumar.

Table of Contents

CHAPTER 1

Introduction

1.1 Transition Metal Oxides (TMO)

For the past two decades there has been a lot of interest in solid oxide fuel cells, sensors, actuators, catalysts and cathode applications. On the other hand understanding the fundamental phenomenon in CMR related oxides like charge, orbital, spin ordering and phase separation is in progress. This renewed interest of scientists to focus their attention on transition metal oxides in particular ABO_3-type perovskite oxides with A=Sr,Ca,La,Ba; and B=Fe,Co,Cr,Mn,Ni. The structural and physical properties of these pervoskites largely depend on defect chemistry. These TMO systems are classified into two types namely, stoichiometric and non-stoichiometric oxides.

1.2 Perovskite Structure

ABO_3 stoichiometric materials mostly stabilize in perovskite structure. In ABO_3 formula, generally A is a cation with 2+ valence state and B is a transition metal cation. A is the larger of the three ions. If there is a distortion in perovskites due to external parameters such as temperature, field, pressure and chemical strain induced by doping, the

structure transform from cubic symmetry depending upon the ratio of ionic radii of A and B. The transformations may take place from cubic to tetragonal, rhombohedral, or monoclinic depending upon the amount of distortion. To sustain a cubic structure the three ions A, B and O should satisfy two conditions simultaneously. The lattice parameter of the unit cell 'a' should be equal to(r_B+r_O) and $a=\sqrt{2}*(r_A+r_O)$, where r_A,r_B and r_O are the ionic radii of A, B and O. Figure 1.1 shows the typical cubic perovskite structure.

For an ideal contact distance of A and B cations,

$$(r_B+r_O) = 1/\sqrt{2}\ (r_A+r_O)$$

The above condition is difficult to satisfy, if satisfied the existing ions show a perfect perovskite structure for a tolerance factor $t = 1$ (in an ideal case) where t is defined as

$t*(r_B+r_O) = 1/\sqrt{2}*(r_A+r_O)$.

In practice the structure normally remains cubic for t in the range from 0.9 to 1.0.

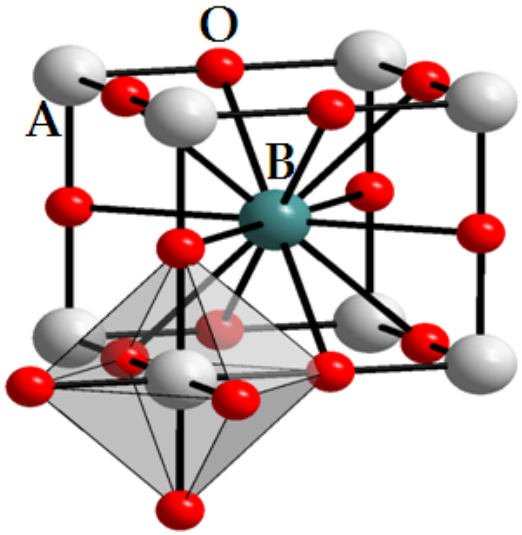

Figure 1.1 The cubic ABO_3 perovskite structure with B cation body center

1.3 Effect of Non-stoichiometry and Defects in structural and physical properties of TMO

A wide range of non-stoichiometric oxides have been studied for the past several decades with the development of new experimental techniques. On the basis of results obtained from various characterization techniques like Electron diffraction, x-ray, neutron and other electron microscopy better understanding is developed and three types of non-stoichiometric behavior is distinguished.

The first type is near the stoichiometric region when the defect concentrations are very small and such defects are classified as point

defects. For these small concentrations there will be no interaction between them. e.g $Fe_{1-\delta}$ O. When the defect concentrations exceeds 0.1 at% there will be interaction between the point defects leading to the second type known as extended defects (called clusters). In $ABO_{3-\delta}$ system, the ionic bonding is dominant over the covalent bonding. One oxygen defect will reduce two B^{n+} ions in to two $B^{(n-1)+}$ ions . Removal of one oxygen atom from the lattice leaves a net positive charge of 2+. In ionic compound the charge (electrostatic) interaction is present between B and O. Every oxygen ion is bound to two B ions and four A ions. The reduction occurs in B cation only, modifying the B-O interaction significantly leaving the A-O interaction unaffected.

If the concentration of clusters (extended defects) becomes too high, the clusters themselves will interact forming a large cluster resulting in a new ordered phase. In perovskite $ABO_{3-\delta}$ systems there are two ways in which the clusters can interact and they are linear clustering and stepwise clustering. In a linear cluster (figure 1.2a) oxygen ions in a B-O-B-O-B-O-B row are removed in one dimension. The octahedral coordination of B ion changes to square planar by removal of two oxygen ions in one dimension. In stepwise clustering (figure 1.2b), two oxygen ions next to each other are removed in BO_6 octahedral coordination, this will result in a tetragonal coordination and

the B ion will rearrange at the centre of the tetrahedron. In figure 1.2a shows the octahedral coordinated B cation and figure 1.2b shows the point defect. [1]

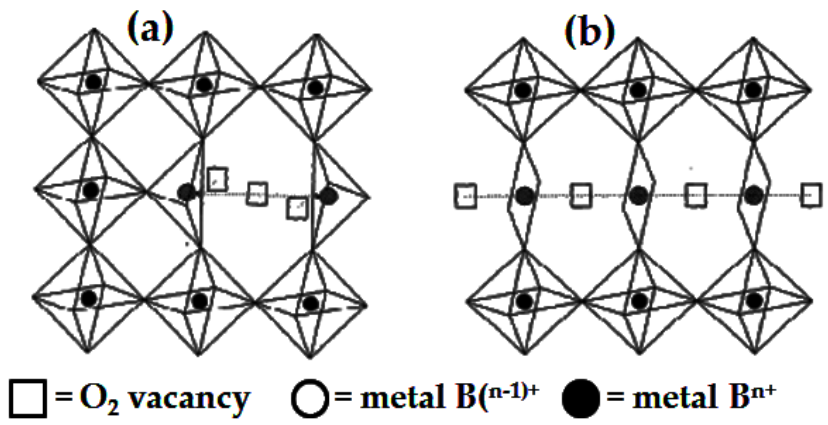

Figure 1.2 (a) Linear interaction between clusters and (b) Stepwise interaction between clusters

1.4 Crystal Field Splitting

Crystal field splitting occurs in TMO systems, basically the transition metal ion with d^n configurations is perturbed by their chemical environment. If the B cation is in octahedral symmetry then the degeneracy splits 3d orbitals into two different sets, triply degenerate t_{2g} and doubly degenerate e_g orbitals, with an energy difference of Δ_{CF} (figure 1.3). Based on Hund's rule the electrons in B cation are accommodated in t_{2g}-e_g orbitals up to the maximum. If the crystal field splitting is larger (Δ) than the pairing energy (U), the electrons first fill up the t_{2g} orbitals completely. The strength of the crystal field decides the electron configuration, if $\Delta > U$ leads to low spin state and if $\Delta < U$ gives rise to high spin state [2].

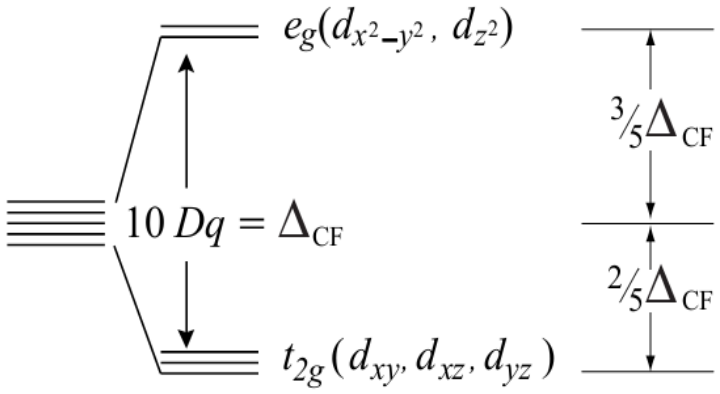

Figure 1.3.Splitting of five fold degenerate d-orbital of an isolated ion in an octahedral crystal field environment.

1.4.1 Jahn-Teller Distortion

The 3d electron configuration in TMO is decided by the internal crystalline fields. In an octahedral coordination (cubic symmetry) two fold degenerate is present. Jahn and Teller (JT) pointed out that to lower the energy of the crystalline fields at $3d^4$ cations distort the cubic symmetry. Distortion of orbitally degenerate configuration to achieve lower energy is known as static JT effect whereas dynamic JT effect is switching of the distortion from one orientation to the other (figure 1.4) [3].

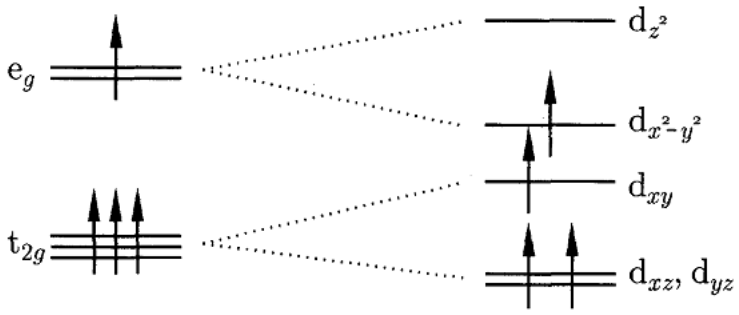

Figure 1.4. Splitting of d-orbital of an TM ion in an octahedral crystal field environment and Jahn-Teller splitting of weak field d^4 configuration.

1.5 Comparison with Isoelectronic configuration in TMO

The electronic and magnetic properties of a material depend on valence electrons. In perovskite structure the B cation has octahedral coordination (BO_6) surrounded with six oxygen atoms. Each oxygen is shared by two B cations in one dimension. The octahedral coordination lifts the 3d orbital degeneracy and favors triply degenerate t_{2g} and doubly degenerate e_g orbitals. The e_g orbitals points directly along the axis and form σ^* bond and t_{2g} orbitals point between the axes and form a π^* bond. The strength of the covalent bonding, the transition metal ion and the oxygen decides the physical properties of the system. If the interaction between the metal (M) and the oxygen (O) is weak, the valence electrons gets localized and the system becomes magnetic-insulator type. If the strength of M-O interaction is sufficiently large, then the increase in spatial overlap of the metal and oxygen orbitals leads to delocalization of valence electrons exhibiting metallic like conductivity.

$LaMnO_3$, $CaFeO_3$ and $SrFeO_3$ are isoelectronic in nature with the electronic configuration of $t_{2g}^3e_g^1$ .Jahn-Teller (JT) theorem suggests that single electron in e_g orbital is not a stable state. $LaMnO_3$ undergoes cooperative JT distortion of MnO_6 octahedra with two long and four short Mn-O bonds. In this compound, Mn exists only in Mn^{3+} state with A-type antiferromagnet. $CaFeO_3$ undergoes charge disproportination,

$2Fe^{4+}(t_{2g}^3e_g^1) \rightarrow Fe^{3+}(t_{2g}^3e_g^2) + Fe^{5+}(t_{2g}^3e_g^0)$. Based on Mössbauer, synchrotron x-ray and neutron powder diffraction the crystal structure of $CaFeO_3$ is found to have two chemically and crystallographically distinct Fe sites and incommensurate antiferromagnetic ground state with Nèel temperature of 120 K[4]. $SrFeO_3$ which is the subject of present investigation is completely different from the above systems as there is no JT distortion and charge disproportination. Moreover, the valence state of 4+ makes the metal-oxygen interaction strong enhancing the width of the σ^* band which is responsible for metal like conductivity in ground state. The tables 1.1 and 1.2 compares the crystal structure, transport and magnetic properties of several trivalent and tetravalent ABO_3 compounds.

Table 1.1 Electronic and structural behavior of some of the Trivalent ABO_3 compounds

Compound	Electronic configuration	Spin state	Crystal structure	Magnetic structure	Transport	Neel Temperature	Ref
$LaMnO_3$	$t_{2g}^3e_g^1$	High	Orthorhombic	A	Insulator	141K	[5,6]
$LaFeO_3$	$t_{2g}^3e_g^2$	High	Orthorhombic	G	Insulator	750K	[7,8]
$LaCoO_3$	$t_{2g}^6e_g^0$	Low	Rhombohedral	Paramag.	Insulator	-	[9]
$LaCrO_3$	t_{2g}^3	High	Orthorhombic	G	Insulator	320K	[10,11]
$LaNiO_3$	$t_{2g}^6e_g^1$	Low	Rhombohedral	Paramag.	Metal	-	[12]

Table 1.2 Electronic and structural behavior of some of the Tetravalent ABO_3 compounds

Compound	Electronic configuration	Spin state	Crystal structure	Magnetic structure	Transport	Neel Temperature	Ref
$CaMnO_3$	t_{2g}^3	High	Orthorhombic	AFM	Insulator	110K	[13]
$CaFeO_3$	$t_{2g}^3e_g^1$	High	Orthorhombic	Incommensurate AFM	Metal	120K	[4]
$SrCoO_3$	$t_{2g}^3e_g^2$	High	Cubic	AFM	Metal	210K	[14,15]
$SrFeO_3$	$t_{2g}^3e_g^1$	High	Cubic	Helical AFM	Metal	134K	[14,16]]

1.6 Magnetic Interactions in TMO

The different types of magnetic orders that are present in materials can be broadly classified based on the presence and type of interaction between the magnetic moments. Absence of unpaired electrons (any permanent magnetic dipoles) leads to diamagnetism, which can be understood on the basis of Lenz's law of electromagnetism. Presence of unpaired electrons leads to permanent magnetic dipoles, and if these magnetic dipoles do not interact with one another, they are oriented at random and give rise to paramagnetism. Depending on the type and range of interaction between the magnetic dipoles, different kinds of magnetic order such as ferromagnetic, antiferromagnetic and

ferrimagnetic order can arise. We will briefly discuss these different types of possible interactions between the magnetic moments.

1.6.1 Exchange interaction

The interactions operating between magnetic moments in solids can be be broadly classified into two types: direct short-range interactions and indirect long-range exchange interactions.

Exchange interactions are basically electrostatic in nature. Let us consider two electrons (on two atoms 'a' and 'b') having spatial coordinates r_1 and r_2 with respect to nuclei. The wave function for the joint state is the product of single electron states. If the first electron is in a state $\psi_a(r_1)$ and the second electron in state $\psi_b(r_2)$, the joint wave function for the two electrons $\psi_a(r_1)\psi_b(r_2)$. This product wave function does not satisfy the condition that overall wave function must be antisymmetric under the exchange of electrons. For electrons the total wave function must be antisymmetric so the spin part of the wave function must be an antisymmetric singlet state χ_S (S = 0) for the symmetric spatial part and if the spatial part is antisymmetric then the spin part is a symmetrical triplet state χ_T(S = 1).

The total wave function which includes both the spatial part and the spin part for the singlet state ψ_S and the triplet case ψ_T can be written as:

$$\psi_S = \frac{1}{\sqrt{2}}[\psi_a(r_1)\psi_b(r_2) + \psi_a(r_2)\psi_b(r_1)]\chi_S$$

$$\psi_T = \frac{1}{\sqrt{2}}[\psi_a(r_1)\psi_b(r_2) - \psi_a(r_2)\psi_b(r_1)]\chi_T$$

The exchange constant (or exchange overlap integral) J is defined as

$$J = \int \psi_a^*(r_1)\psi_b^*(r_2)\boldsymbol{H}\psi_a(r_1)\psi_b(r_2)dr_1\,dr_2$$

The Hamiltonian $H = -2\sum_{i>j} J_{ij}(S_i * S_j)$. If two electrons are on same atom, the exchange integral is usually positive stablizing the triplet state which ensures the antisymmetric spatial part. This minimizes the Coulomb repulsion between the two electrons by keeping them apart. When the two electrons are on neighbouring atoms, the exchange integral is negative [3].

1.6.2 Direct exchange

The exchange interaction between two neighboring spin moments arises as a consequence of the overlap between the magnetic orbitals of the two adjacent atoms. This so-called direct exchange interaction is strong in 3d metals, because of the comparatively large extent of the 3d electron charge cloud. Bethe-Slater semi empirical curve (Fig. 1.5) describes as to how the magnetic moment coupling changes when the interatomic distance between the corresponding atoms changes. The exchange

integral J_{ij} is positive for ferromagnets and negative for antiferromagnets [17].

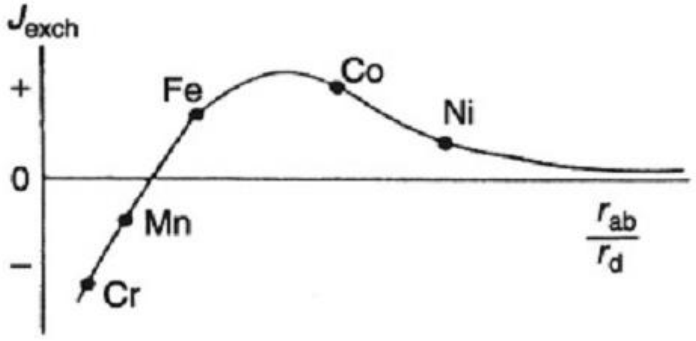

Figure 1.5 Bethe-Slater curve describing the variation of the exchange constant with interatomic separation r_{ab} and the radius r_d of the incompletely filled shell.

1.6.3 Super Exchange Interaction

Most of the transition metal oxides are insulators and electrons are localized. The probability of direct overlap between 3d-3d orbital is less, but the hybridization between metal 3d and oxygen 2p orbitals is possible. Figure 1.6 shows the super exchange bond. In the case of singly occupied 3d orbital or half filled shell (Fe^{3+}, Mn^{2+}) configuration (b) is lower in energy than configuration (a), because both the electrons in an oxygen 2p orbital spread out into unoccupied 3d orbitals. The

superexchange interaction J involves simultaneous virtual transfer of two electrons with instantaneous formation of a $3d^{n+1}2p^5$ excited state. J depends on interatomic separation and M-O-M (M stands for the transition metal ion) bond angle. The occupancy and orbital degeneracy of the 3d orbital decides the strength and sign of superexchange. Goodenough –Kanamori [18] proposed a set of rules for superexchange interaction to mediate and they are as follows.

(1) When the cations have lobes of singly occupied 3d orbitals which point towards each other, giving large overlap and hopping integrals, the exchange is strong and antiferromagnetic. Bond angle between M-O-M is 120˚ -180˚.

(2) If two cations have an overlap integral between singly occupied 3d orbitals, then the exchange is ferromagnetic and relatively weak. The bond angle between M-O-M is 90˚.

(3) When two cations have an overlap between singly occupied 3d orbitals and empty or doubly occupied orbitals of the same type, the exchange is ferromagnetic and relatively weak.

Superexchange is more commonly antiferromagnetic than ferromagnetic, because the overlap integrals are more likely to be larger than zero [18].

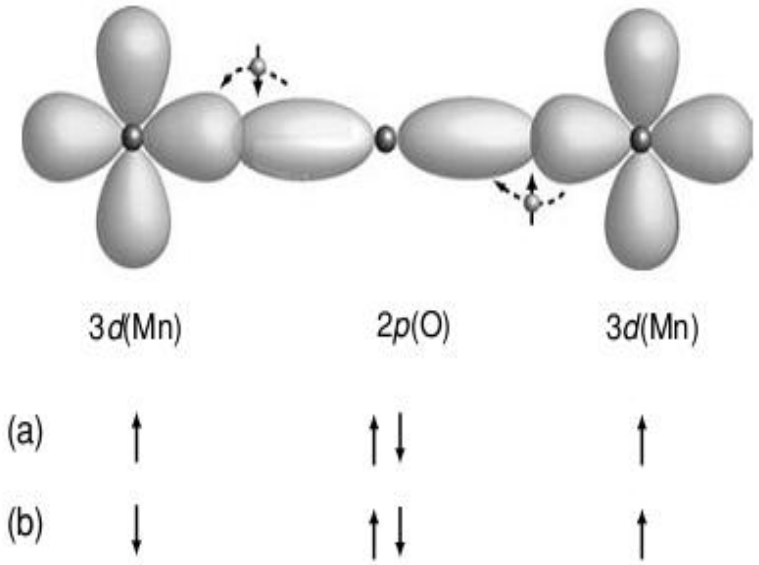

Figure 1.6 A typical super exchange bond. Configuration (b) is lower in energy than configuration (a).

1.6.4 Double exchange

This interaction arises between 3*d* ions which have both localized and delocalized *d* electrons. Mixed valence configuration is required for double exchange. For example, $La_{0.7}Ca_{0.3}MnO_3$ has both Mn^{3+} and Mn^{4+} ions (d^3 and d^4) present on octahedral sites. The d^3 core electrons for both octahedrally coordinated ions are localized in a narrow $t_{2g}\uparrow$ band, but the fourth *d* electron inhabits a broader $e_g\uparrow$ band, hybridized with

oxygen, where it can hop from one d^3 core to another (figure 1.7). Double exchange leads to a ferromagnetic order as electrons can hop freely if the core spins are parallel, but when they are antiparallel there is strong energy barrier due to the Hund's rule [18].

Figure 1.7 Double exchange interaction. The electron hops with spin memory from one localized ion core to the next.

1.7 Spin glass

Spin system with both FM and AFM interactions competing with each other finds it difficult to decide among various collinear magnetic orders in the ground state due to randomness and frustration of spins resulting from the competing interactions. As a consequence, the frustrated spins freeze in random orientations below a certain temperature (called the

freezing or spin glass temperature) in the spin glass state. A spin glass can arise in two ways. (i) If a small amount of magnetic impurities are added to a non-magnetic metallic host, the interactions between the magnetic atoms are mediated by the conduction electrons. In this situation, the magnetic interaction oscillates between ferromagnetic and antiferromagnetic depending upon the distance between the magnetic ions. This type of interaction is termed as RKKY interaction. (ii) In an amorphous solid, the nearest neighbor distance between the atoms has a distribution. Thus, exchange integral J which sensitively depends on distance and angle between the magnetic atoms, also has a distribution. If this distribution in J is peaked at J = 0, the competing ferromagnetic and antiferromagnetic interactions establish a spin glass state [19].

The net magnetic moment is zero in both paramagnetic and spins glass state. But below the spin glass (SG) transition temperature, the time average moment on a site is non- zero. Below the SG transition temperature, the spins are frozen in random directions whereas in the paramagnetic state spins are oriented at random but they fluctuate in time around mean random directions. Therefore, spin glass transition occurs without spontaneous symmetry breaking. Spontaneous magnetization (M_s) cannot be the order parameter for the spin glass

phase transition because above and below transition temperature M_S is zero.

1.8 Temperature coefficient of Resistance (TCR)

The electrical conductivity of semiconductors (σ) can be expressed as $\sigma = qμp$, where q is the charge, μ is the mobility and p is the concentration of charge carriers. The temperature coefficient of the semiconducting metal-oxide is decided by the temperature dependence of the mobility and the concentration of the charge carriers. The increase in electrical resistivity with increasing temperature is called positive temperature coefficient of resistivity (PTCR).

Materials with zero TCR (temperature independent resistivity) are most sought after in automotive industry for oxygen sensing applications without cross sensitivity to temperature. $SrTi_{1-x}Fe_xO_{3-\delta}$ (STF) solid solutions were found to shift their coefficient of resistance (TCR) from negative to positive as Fe increasingly substitutes for Ti. $SrTiO_3$ (STO) is a wide band gap semiconductor with a band-gap of 3.2 eV and the band gap decreases with increasing Fe doping. It is reported in the literature [20] that the variation in the bandgap energy as a function of Fe content is responsible for the change in TCR of Fe doped STO.

1.9 Review of earlier work in $SrFe_{1-x}Ti_xO_{3-\delta}$ systems

Synthesis of stoichiometric Transition Metal Oxides (TMO) is a challenge and usually non-stoichiometry is observed which leads to interesting physical properties. Depending upon the concentration of oxygen defects different crystal structures are stabilized. If the concentration of the defects is up to 0.1at%, the interaction between the point defects still retains the original crystal structure of the defect-free TMO. In $SrFeO_{3-\delta}$ (ABO_3 cubic perovskite family), the Fe-O bonding is ionic rather than covalent. The stoichiometric $SrFeO_3$ ($\delta = 0$) has a cubic perovskite structure and is a helical antiferromagnet with Nèel temperature, T_N =130 K. For a small concentration of oxygen deficiency ($\delta \sim 0.03$), the cubic structure is retained.

Non-stoichiometric $SrFeO_{3-\delta}$ forms four crystallographically distinct phases depending upon the oxygen deficiency [21]. The different phases can be realized based on the interaction mediated through the defects. In the $SrFeO_{3-\delta}$ compound, Fe exists in the valence states of 4+ and 3+. Mixed valence nature makes this system to exhibit interesting electric, magnetic and transport properties. With the increase in oxygen deficiency as the defect concentration increases beyond a threshold value, the defects start to interact with each other forming

extended point defects. In $SrFeO_{3-\delta}$, every oxygen ion is bound to two Fe ions and four Sr ions. The interaction is mostly Fe-O rather than Sr-O as the valence state of only Fe is effected by the oxygen deficiency. If the concentration of the Fe-V_O-Fe (V_O- Oxygen vacancy) clusters becomes too high, then clusters themselves will interact over a long range forming a different crystal structure. These clusters can interact in two ways [1]. The first type is a linear cluster interaction observed for an oxygen deficiency of $\delta \sim 0.125$, which crystallizes the system in to tetragonal structure, as observed in $Sr_8Fe_8O_{23}$ ($SrFeO_{2.875}$). For $\delta \sim 0.25$, the interaction of the clusters is stepwise leading to orthorhombic $Sr_4Fe_4O_{11}$ ($SrFeO_{2.75}$) structure. With further increase in the oxygen deficiency, i.e., for $\delta \sim 0.5$, $SrFeO_{3-\delta}$ has Brown Millerite structure [21]. Hodges et.al. [21] determined the crystal structure for the undoped $SrFeO_{3-\delta}$ system (for all the 4 phases) by comparison of Rietveld refined data of several closely related structural models proposed in the literature. The stoichiometric $SrFeO_3$ is found to be of simple cubic structure with Pm-3m space group. The space group for $SrFeO_{3-\delta}$ with $\delta = 0.125$ and tetragonal structure is found to be I4/mmm.

1.10 Motivation and objectives of the present work

Synthesizing a completely single phase of $SrFeO_{3-\delta}$ is a challenge as the traces of minor phases are observed even in single crystals of $SrFeO_{3-\delta}$. One way to address this issue is by partially doping Fe with another TM such as Ti. One of the motivations for the present work is to stabilize the single phase $SrFeO_{3-\delta}$. Doping of Ti is found to stabilize $SrFeO_{3-\delta}$ in the tetragonal structure with space group I4/mmm.

$SrFe_{1-x}Ti_xO_{3-\delta}$ (STF) is an interesting solid solution [22] system as the Fe-rich phase is a good electronic and ionic conductor and the Ti-rich phase is an acceptor - doped large band gap insulator. These mixed conductors hold a key to multi-functional materials that can be used in fuel cells, electrochemical sensors, permeation membranes and catalysts [23-26]. By partial replacement of Fe^{4+} in $SrFeO_{3-\delta}$ with a non-magnetic ion of Ti^{4+} , the $SrFe_{1-x}Ti_xO_{3-\delta}$(x =0 - 0.3) system is prepared. In this system, Ti^{4+} replaces Fe in the oxidation states of Fe^{3+} and Fe^{4+}; the actual Fe^{3+}/Fe^{4+} concentration depends on the total Fe concentration and applied oxygen partial pressure during synthesis. It is also reported in the literature that the charge compensation for Fe^{3+} occurs mainly by the mobile oxygen vacancies. Even though it is a well-established fact that the structure of parent $SrFeO_{3-\delta}$ system depends critically on the

stoichiometry of oxygen, so far there are no reports of non-cubic Ti^{4+} doped $SrFeO_{3-\delta}$ system [27-37].

There are a number of reports on Mössbauer effect studies (ME) [20, 38, 39] of $SrFeO_{3-\delta}$ because ME determines the coordination of Fe ion, valence state, magnetic alignment and also the interaction of specific ion with its coordination. ME data give the complimentary information regarding the site occupancy and the valence state of Fe.

In this work, the crystal structure of $SrFe_{1-x}Ti_xO_{3-\delta}$(x =0 - 0.3) system is established through neutron diffraction data refinement. The Mössbauer data is analyzed taking in to account the existence of Fe in three different sites.

Ti substitution is expected to affect the structure and physical properties of $SrFeO_{3-\delta}$ host drastically. This prompted us to undertake an extensive investigation of structural, magnetic and transport properties of $SrFe_{1-x}Ti_xO_{3-\delta}$ system with the following objectives in mind.

1. $SrFeO_{3-\delta}$is known to have different phases with completely different structural and magnetic properties. The first aim is to synthesize $SrFeO_{3-\delta}$, characterize its structure, microstructure, magnetic and transport properties.
2. To investigate the crystal structure of $SrFe_{1-x}Ti_xO_{3-\delta}$

3. In tetragonal $SrFeO_{3-\delta}$ (T-$SrFeO_{3-\delta}$), Fe occupies different sites, what is the cation distribution in $SrFe_{1-x}Ti_xO_{3-\delta}$?
4. T-$SrFeO_{3-\delta}$ is a helical antiferromagnet,what is the effect of Ti^{4+} on the magnetic properties such as H_C, ordering temperature and exchange bias.
5. What is the magnetic ground state of Ti doped T-$SrFeO_{3-\delta}$?
6. $SrFeO_3$ is a metal, the other end of the Ti doped solid solution $SrTiO_3$ is an insulator. What is the effect of Ti doping on the transport and magneto-transport properties?
7. $SrFe_{1-x}Ti_xO_{3-\delta}$is of interest for high temperatures applications in sensors, electrodes for fuel cells, etc. To investigate the high-temperature conductivity and study the nature of temperature coefficient of resistance (TCR).

1.11 Scope of present work

The first chapter describes briefly about oxygen defects in transition metal oxides and different magnetic interactions present in this type of oxides. The second chapter describes about various experimental techniques which are used to investigate the present thesis work.

Chapter 3 describes the synthesis, results of the microstructure and structural characterization of $SrFeO_{3-\delta}$ with and without Ti doping

using X-ray diffraction, Neutron diffraction, Mössbauer spectroscopy and TGA techniques. The structural parameters like bond-length, bond angles and cation distribution in each coordination is established. With the help of low temperature Mössbauer and neutron diffraction, it is established that Fe occupies three different coordinations both crystallographically and magnetically.

Chapter 4 describes describes the results of the studies on $SrFe_{1-x}Ti_xO_{3-\delta}$ (x=0 to 0.3) by AC Susceptibilty, Magnetization, and low temperature Neutron diffraction techniques. Based on all the three sets of data, it is established that the undoped system exhibits the long-range helical antiferromagnetic order while the Ti doped systems behave as a cluster spin-glass.

Chapter 5 describes the results of the transport and magneto-transport studies on $SrFe_{1-x}Ti_xO_{3-\delta}$ (x = 0 to 0.3) carried out by the standard four probe technique using the dc transport option of PPMS. These systems have defects (vacancies) originating from the oxygen deficiency and site disorder caused by a partial substitution of Ti^{4+} at Fe sites. Large change in resistivity due to charge ordering is observed when lowering the temperature. In all the above systems, semiconducting like decrease in resistivity with increase in

temperature is observed. The temperature dependence of resistivity is well described by the three dimensional Variable Range Hopping (3D-VRH) model. Magneto-resistance is measured by applying a field of 80 kOe and the results are discussed.

Chapter 6 describes the composition dependence of ac conductivity of Ti doped $SrFeO_{3-\delta}$ measured from room to high temperature of 450 °C. Complex impedance spectroscopy data are analyzed based on Cole-Cole type impedance response function and σ_{dc} (dc conductivity) and activation energy are calculated. The measured data are analyzed using Jonscher's universal power law to explain the observed dispersive behavior of the electrical conductivity. Positive temperature coefficient of resistance (PTCR) for x =0.2 and 0.3 is observed for the first time at ambient pressure and moderate temperature. The correlation between TCR and electrical modulus is observed. The non linear variation of the conductivity with increase in Ti doping is attributed to the change in Fe-O bond distances and also the increase in site disorder.

References

[1] J.A.M Van Roosmalen and E.H.P.Cordfunke, Journal of Solid State Chemistry 93 (1991) 212.

[2] J.M.D. Coey, Magnetism and Magnetic materials, Cambridge University Press (2010).

[3] Stephan Blundell, Magnetism in Condensed Matter, Oxford University Press (2001).

[4] Patrick M.Woodward ,David E. Cox , EvagaliaMoshopoulou and Arthur W.Sleight, Research Highlights, NIST Center for Neutron Research.

[5] G. Matsumoto J.Phys.Soc.Jpn. 29,606 (1970).

[6] J.B.A.A Elemans, B. Van Laar, K.R. Van der Veen and B.O. Loopstra, J.Solid State Chem.3, 238 (1971).

[7] P. Border et al ,J.Solid State. Chem. 106 ,253 (1993).

[8] M. Marezio and P.D.Dernier Mat.Res.Bull.6,23 (1971)

[9] V.G.Rojaria, C.N.R. Rao, G.Rama and V.G.JadhoPhys.Rev.B 12, 2832 (1975).

[10] W.C. Kohler and E.O. Wollan, J.Phys.Chem.Solids 2, 100 (1957)

[11] C.P. Khattak and D.E Cox Mat.Res.Bull.12, 463 (1977).

[12] J.L. Gracia-Munoz, J. Rodriguez-Carvajal, P.Lacoore and J.B.Torrance, Phys.Rev.B 46, 4414 (1992).

[13] J. Briatico, B. Alascio, R. Allub, A. Butera, A. Caneiro, M.T. Causa and M. Tovar, Phys.Rev.B 53, 14020 (1996).

[14] S. Kawasaki, M. Takano and Y. Takeda J.Solid State Chem. 121, 174 (1996)

[15] T. Takeda and H.WatanabeJ.Phys.Soc.Jpn. 33, 973 (1972)

[16] T. Takeda, S. Komura and H. FujiiJ.Mag.Mag.Mat.31, 797 (1983).

[17] K.H.J. Buschow, F.R. de Boer, Physics of Magnetism and Magnetic Materials, Kluwer Academic Publishers (2003)

[18] Ralph Skomski, Simple models of Magnetism, Oxford University Press (2008).

[19] A.C Muller, A.J. van Duyneveldt and J.A. MydoshPhys.Rev.B 23,1384 (1981).

[20] Avner Rothschild, Scott J. Litzelman, Harry L.Turner, Wolfgang Mensklou, Thomas Schneider and Ellen Ivers-Tiffee, Sensors and Actuators B: Chemical , 108, 223 (2005).

[21] J.P.Hodges ,S.Short, J.D.Jorgensen, X.Xiong,B.Dabrowski, S.M.Mini and C.W.Kimball Journal of Solid State Chemistry 151(2000) 190.

[22] Wolfgang Menesklou, Hans-Jurgen Schreiner, Karl Heinz Hardtl and Ellen Ivers- Tiffee , 'High temperature oxygen sensors based on doped $SrTiO_3$', Sensors and Actuators B:Chemical 59[2-3]184-189(1999).

[23] B.C.H Steele, Ceramic ion conducting membranes, Current Opinion in Solid State and Material Science 1, (1996) 684.

[24] William C. Maskell, Solid State Ionics 134 (2000) 43.

[25] G. Sberveglieri, Sensors and Actuators B 23 (1995) 103.

[26] A.V.Kovalevsky, V.V. Kharton, F.M.M.Snijkers, J.F.C.Cooymans, J.J.Luyten, F.M.B.Marques Journal of Membrane Science 301(2007) 238.

[27] E.Mashkina, A.Magerl, J.Ollivier, M.Gobbels and F.Seifert Phys. Rev. B 74 (2006) 214106.

[28] H.D. Zhou and J.B. Goodenough Journal of Solid State Chemistry 177(2004) 1952.

[29] Hyun –Suk Kim, Lei Bi, Dong Hun Kim, Dae-Jin Yang, Yoon Jeong Choi, Jung Woo Lee, Yun Chang Park, Gerald F.Dionne and Caroline A.RossJ.Mater.Chem., 21(2011)10364.

[30] S.Srinath ,M.Mahesh Kumar, K.Sahner, M.L.Post, M.Wickles, R.Moos and H.Srikanth Journal of Applied Physics 99 (2006) 08S904.

[31] M.Vracar, A.Kuzmin, R.Merkle, J.Purans, E.A.Kotomin, J.Maier and O.Mathon Phys. Rev. B 76(2007)174107.

[32] Chen Ang, J.R.Jurado, Zhi Yu, M.T.Colomer, J.R.Frade and J.L.Baptista , Phys. Rev B 57 (1998)11858.

[33] Avner Rothschild, Wolfgang Menesklou, Harry L.Tuller, and Ellen Ivers-Tiffee Chem.Mater.,18 (2006) 3651.

[34] A.Wattiaux ,L.Fournes, A.Demourgues, N.Bernaben, J.C.Grenier, and M.Pouchard 77 (1991) 489.

[35] V.V. Kharton ,A.P.Viskup, A.V.Kovalevsky, J.R.Jurado, E.N.Naumovich, A.AVecher, and J.R.Frade , Solid State Ionics 133 (2000) 57.

[36] Peter Alder and Sten Eriksson Z.Anorg.Allg.Chem. 626 (2000) 118.

[37] J.R.Jurado ,F.M.Figueiredo and J.R.Frade Solid State Ionics 122 (1999) 197.

[38]Y.Takeda, K.Kanno ,T.Takada, O.Yamamoto, M.Takano, N.Nakayama and Y.Bandol, J.Solid State Chemistry 63(1986) 237.

[39] M.Takano, T.Okita, N.Nakayama, Y.Bando, Y.Takeda, O.Yamamoto and J.B.Goodenough, J.Solid State Chemistry 73(1988) 140.

CHAPTER 2

Experimental Techniques

In this chapter, we briefly explain the experimental techniques which are used to investigate the structural, magnetic and transport properties of $SrFeO_{3-\delta}$ *with and without Ti doping presented in this thesis.*

2.1 Introduction

Characterization techniques play an important role to study the materials in order to understand their properties. Fundamental properties of the materials inherit from their internal structures such as defects, microstructure, grain boundaries and crystal structure. Various characterization techniques are employed in the study of structural, magnetic, transport and dielectric properties of materials. The present chapter describesa brief introduction of powder X ray and Neutron diffraction, Mössbauer, Physical Property Measurement System (PPMS-VSM, ACMS and DC resistivity), Impedance analyzer, Field Emission Scanning Electron Microscope (FE-SEM), and Thermogravimetric analyzer (TGA).

2.2 X-ray Powder diffraction

The powder diffraction method (Debye and Scherrer method) is one of the the most useful diffraction methods and when properly employed, can yield a great deal of structural information about the material under investigation. The powder diffraction of a substance is characteristic of the substance and forms a sort of fingerprint [1] of the substance to be identified. Powder diffraction method involves the diffraction of monochromatic x-rays by a powder specimen.

Selection of K_α renders the incident beam to be a highly monochromatised one. The focusing monochromatic geometry results in narrower diffracted peaks and low background at low angles. INEL x-ray diffractometer with Co target x-ray tube is used to do all x-ray diffraction measurements in this thesis. Position Sensitive Detector (PSD) filled with P10-gas (10% methane in Argon) is employed to record the counts.

The peaks of the x-ray diffraction pattern of known samples for which the data is available can be compared with the standard available data for the confirmation of the structure. For the purpose of comparison, many standards are available [2], some of which are Willars Hand book, Joint Committee on Powder Diffraction Standards (JCPDS) Pcpdf win and National Bureau of Standards.

A beam of x-rays of wavelength λ, incidents on the crystal at an angle θ to the atomic planes. In Bragg's law, the interaction between x-rays and the electrons of the atoms is visualized as a process of reflection of x-rays by the atomic planes. This is an equivalent description of the diffraction effects produced by a three dimensional grating. The atomic planes are considered to be semi-transparent, that is, they allow a part of the x-ray to pass through and reflect the other part, the incident angle θ (called the Bragg angle) being equal to the reflected

angle. Referring to Fig. 2.1, there is a path difference between the x-rays reflected from plane 1 and the adjacent plane 2 in the crystal. The two reflected x-rays will reinforce each other, only when this path difference is equal to an integral multiple of the wavelength. If "d_{hkl}" is the inter-planar spacing, the path difference is twice the distance d sinθ, as indicated in figure 2.1. The Bragg condition for reflection can therefore be written as $2d_{hkl}\sin\theta = n\lambda$ 2.1

where, n is an integer (order of diffraction), λ is the wavelength of the x-ray used, θ is the Bragg angle.

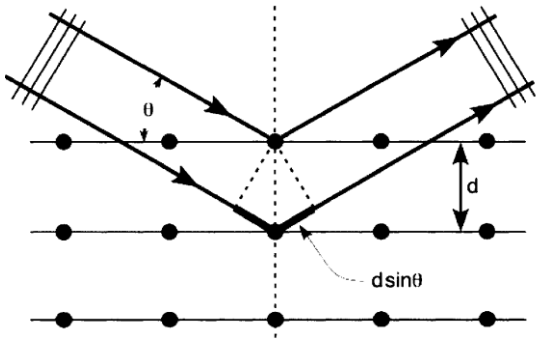

Figure 2.1 Illustration of Bragg's law

2.3 Neutron Powder Diffraction

A neutron beam is highly penetrating and thus gives details about not only the surface but also about the bulk of the sample.The oxygen ions have weak presence in the x-ray diffraction pattern. Neutron scattering amplitudes depends on how neutrons are scattered by the nucleus. Most of the nuclei scatter neutrons equally well. In neutron scattering, amplitudes for neighboring Z values could differ from each other unlike x-ray. For example, the scattering amplitude for x-rays is nearly the same for Mn and Fe but for neutron the scattering amplitudes are -0.39 p cm/atom and 0.95 p cm/atom respectively [3,4]. Unlike x-rays, for neutrons the scattering amplitudes fall off rapidly with increasing $\sin(\theta)/\lambda$, where 2θ is the scattering angle and λ is the wavelength of the incident radiation. In x-ray scattering the wavelength is comparable to the dimensions of the scatterer but in neutron case nucleus is very small in comparison to the wavelength of neutrons [5,6].

In general, X-ray scattering amplitude is directly related to the atomic number of the scattering element. In the present $SrFe_{1-x}Ti_xO_{3-\delta}$ system the atomic numbers of the four elements are: 8 for Oxygen, 26 for Iron, 22 for Titanium and 38 for Sr. Neutron powder diffraction can detect the presence of oxygen as the scattering takes place from the nucleus and depends on mass number rather than the atomic number.

The magnetic moment of the neutron interacts with the magnetic moment associated with unpaired electrons of the sample giving rise to the magnetic scattering. X-rays and neutrons are extensively used to study the structural properties. In the case of magnetic materials (antiferromagnetic, ferrimagnetic and ferromagnetic), neutron diffraction can reveal both the magnitude and direction of the moments.

2.3.1 High Resolution powder neutron diffractometer

The neutron diffraction measurements presented in this thesis were carried out using Multi-PSD, high throughput, high resolution neutron powder diffractometer at Dhruva Reactor, Trombay, Mumbai, designed and developed [7] by UGC-DAE CSR Mumbai Centre, India (Fig. 2.2). The instrument employs open beam geometry (i.e., no Soller collimators), doubly bent perfect and asymmetrically cut Si single crystal to enable high flux at the sample position and good resolution over wide scattering angular range. It is possible to change the wavelength of monochromatic beam by computer controlled goniometer within couple of minutes. The usable wavelengths on this instrument are 1.1 Å, 1.48 Å, 1.76Å & 2.31 Å. The standard wavelength for is 1.48 Å. For all the neutron diffraction measurements reported in this thesis a wavelength of 1.48 Å was used.

The diffractometer is equipped with a cryogen free magnet (CFM) driven by closed cycle refrigerator (CCR). Using this CFM, neutron diffraction measurements can carried out at any temperature from 1.6K to 300K and magnetic fields up to 7 Tesla. The neutron results presented in this thesis were measured using this CFM.

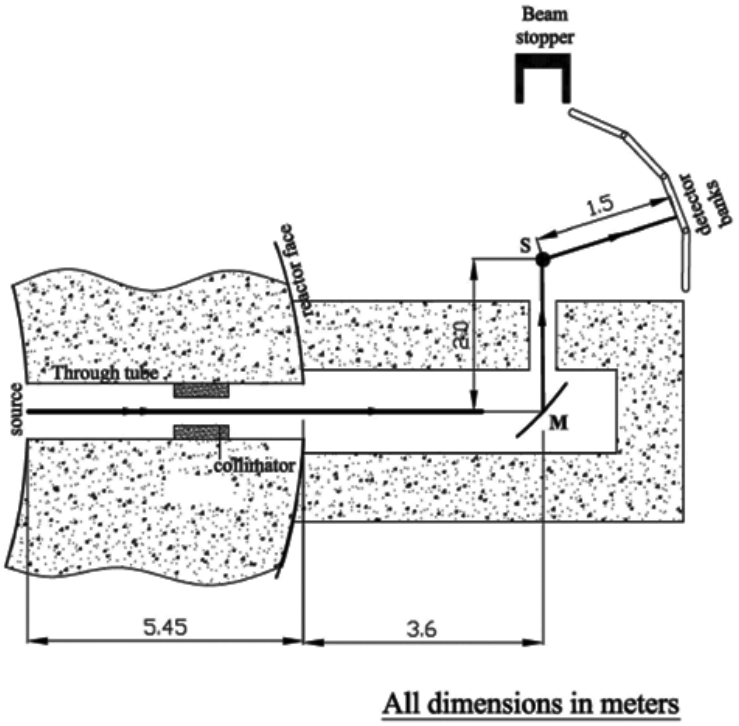

Figure 2.2 The schematic lay-out of the neutron diffractometer based on focusing monochromator

The powder samples were filled Vanadium sample holder, which then attached with to sample holder that is inserted into the CFM. Sample is cooled by the Helium gas that is flowing through the sample chamber. This diffractometer is equipped with oscillating radial collimator (ORC) between the CFM and the detectors, which eliminates contamination from the CFM shrouds apart from reducing general background and improving S/N ratio.

Neutron scattering on magnetic materials consists of two parts namely nuclear and magnetic. For the nuclear scattering, the form factor is angular independent and the scattering intensity will not decrease with increase in angle and even at higher angles there is a sizable contribution. Whereas, the magnetic scattering is not isotropic and decreases sharply with increase in angle (s-wave type). Figure 2.3 shows the atomic form factor for x-ray, neutron (nuclear and magnetic) versus angle and figure 2.4 shows the neutron scattering amplitude versus atomic weight.

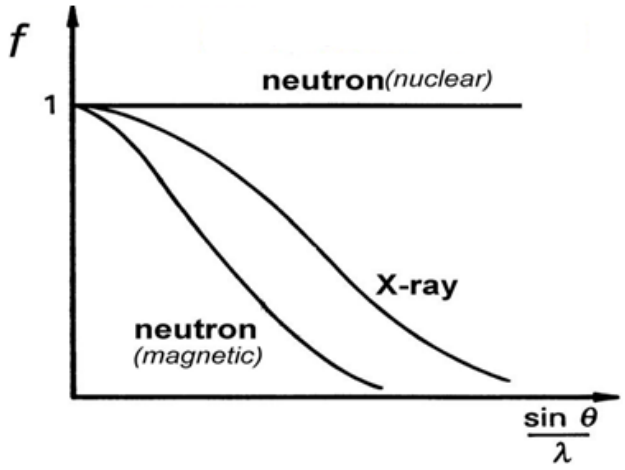

Figure 2.3 The atomic form factor for x-ray, neutron (nuclear and magnetic) against angle.

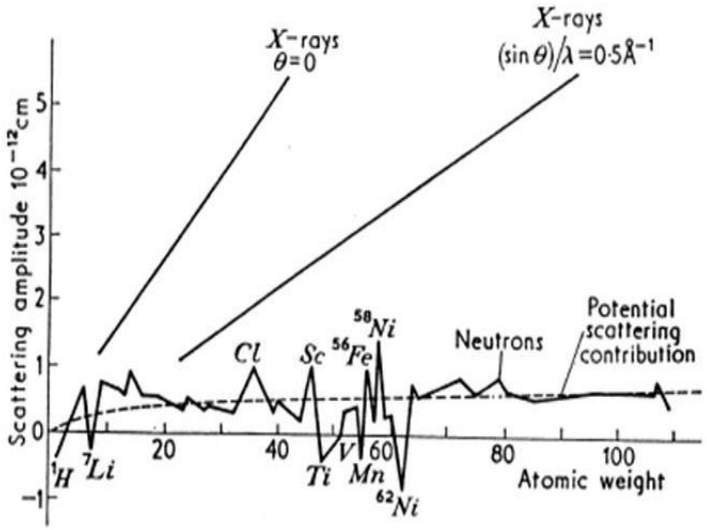

Figure 2.4 The neutron scattering amplitude versus atomic weight

2.4 Mössbauer Spectroscopy

^{57}Fe Mössbauer spectroscopy is one of the most important local probes to understand the structural and magnetic properties of the materials containing iron. The phenomenon of recoilless emission and resonant absorption of nuclear gamma rays in solids is called the Mössbauer effect.

During the interaction between the sample and gamma ray there is a possibility of exciting lattice vibrations, i.e., creation or annihilation of phonons. These lattice vibrations are quantized and if the free atom recoil energy is less than the phonon energy, statistically, there is a fraction *f* of events that take place without lattice vibrations.

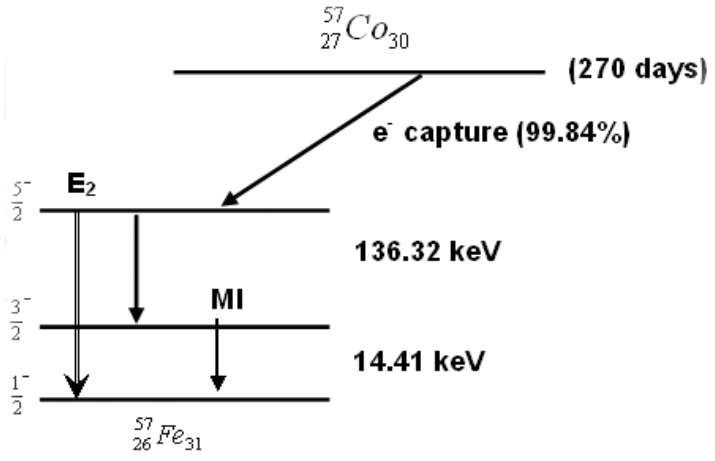

Figure 2.5 Decay scheme of ^{57}Co source.

These events, which are called zero phonon transitions, have the spectrum centered on $E_t$with the natural line width [10,11]. This is called the Mössbauer effect. Since ^{57}Fe Mössbauer isotope is used in the present study, all illustrations in this thesis are confined to ^{57}Fe Mössbauer spectroscopy only. The decay scheme of ^{57}Co decaying into ^{57}Fe is shown in figure 2.5.

2.4.1 Mössbauer parameters

The values of the different Mossbauer parameters yield valuable information about the crystal field associated with the Fe at a particular coordinate site depending on the interaction of the crystal symmetry and magnetic moment associated at a particular Fe site with the gamma rays. There are three main hyperfine interactions (i) isomer shift (electric monopole interaction), (ii) quadrupole splitting (electric quadrupole interaction) and (iii) nuclear Zeeman effect (magnetic dipole interaction). These parameters are important to understand magnetism and other structural information of the nuclei which are embedded in the lattice [12-15]

2.4.1. (a) Isomer shift (electric monopole interaction)

Isomer shift (I.S.) arises due to the difference in the electrostatic interaction between the nuclear charge and the electronic charge of

source and the absorber in the excited and ground states of the Mössbauer nucleus (figure 2.6). This interaction causes a shift in the resonance peak from the zero velocity position in absence of electric quadrupole and magnetic dipole interactions. This shift is known as the isomer shift or centre shift. When electric quadrupole and magnetic dipole interactions are present, the position of the centre of gravity of the spectrum from the zero velocity is a measure of the isomer shift.

$$I.S. = (\delta E)_e - (\delta E)_g \quad {}_a - \left[(\delta E)_e - (\delta E)_g\right]_s \qquad 2.2$$

It can be shown that

$$I.S. = (4\pi/5)Ze^2R^2(\delta R/R)\left[\,|\Psi(0)|_a^2 - |\Psi(0)|_s^2\,\right] \qquad 2.3$$

with $R = (R_e + R_g)/2$ and $\delta R = R_e - R_g$. Here Ze is the nuclear charge, R_e and R_g are nuclear radius in its excited and ground states, respectively. δR is negative for ^{57}Fe and $-e\,|\psi(0)|^2$ is the electronic charge density at the nucleus. The suffixes *a* and *s* represent the terms for the absorber and the source respectively. From isomer shift, one can find (i) the sign and magnitude of $\delta R/R$, (ii) the s-electron density at the nuclear site and (iii) the spin and charge states of metal ions in solids.

2.4.1. (b) Quadrupole splitting (electric quadrupole interaction)

The interaction of the nuclear quadrupole moment eQ with the electric field gradient eq due to other charges in the crystal is called quadrupole interaction. The quadrupole interaction can be expressed by the Hamiltonian

$$H = Q.\nabla \mathrm{E} \qquad with \qquad Q_{ij=} \int \rho_n(r)\mathbf{x_i}.\mathbf{x_j}\, dv \qquad (2.4)$$

where ρ_n is the nuclear charge density and x_i and x_j are the Cartesian coordinates of **r**. The field gradient $\nabla \mathrm{E}$ a 3 x 3 tensor. The Eigen value

$$E_Q = \frac{e^2 qQ}{4I(2I-1)}\left[m_I^2 - I(I+1)\right]\left[1 + \frac{\eta^2}{3}\right]^{1/2} \qquad (2.5)$$

equation for the interaction Hamiltonian is

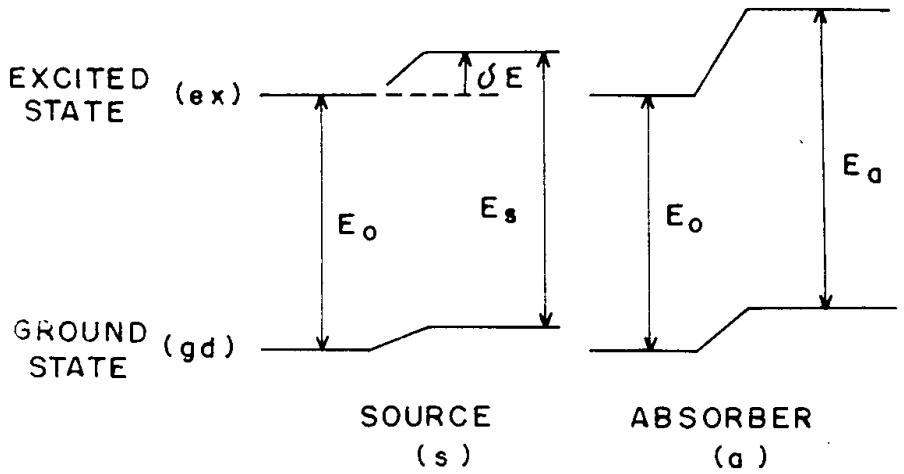

Figure 2.6The effect of electric monopole interaction on nuclear energy levels.

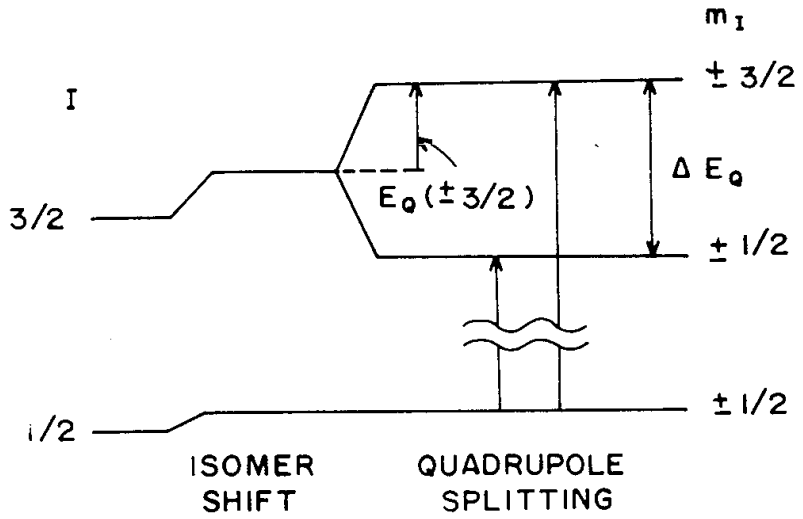

Figure 2.7The effect of electric quadrupole interaction on nuclear energy levels.

With the magnetic spin quantum number $m_I = I,\ I-1,\ldots,\ -I$ and the asymmetry parameter η, Nuclear state with $I > 1/2$ is having $(2I + 1)$ fold degeneracy and it will split into sub states $|I, \pm m_I\rangle$ without shifting the centre of gravity. The excited state with $I = 3/2$ splits into two sub states $|3/2 \pm 1/2\rangle$ and $|3/2 \pm 3/2\rangle$ as shown in figure 2.7. Therefore, two resonance lines are observed and the separation between these two lines is called the quadrupole splitting. The separation (Q.S.) is given by,

$$\text{Q.S.} = \left(\frac{1}{2}\right) e^2 Qq \left[1 + \frac{\eta^2}{3}\right]^{1/2} \qquad (2.6)$$

The resonance lines are equal in intensity for an isotropic system. The anisotropic vibrations of the lattice give raise to asymmetric doublets. The quadrupolemoment $e\boldsymbol{Q}$, is constant for a given Mössbauer nucleus while quadrupole splitting depends on the electric field gradient (EFG). The quadrupole splitting would give information about the electronic structure, bonding and molecular symmetry.

2.4.1. (c) Nuclear Zeeman effect (magnetic dipole interaction)

The interaction of the nuclear magnetic moment, $\boldsymbol{\mu}$, with the internal magnetic field $\boldsymbol{H}$at the nucleus due to the atom's own electrons is called the nuclear Zeeman effect or magnetic hyperfine interaction. The Hamiltonian for this interaction is,

$$H_m = -\boldsymbol{\mu}.\boldsymbol{H} = -g_N \beta_N \boldsymbol{I}.\boldsymbol{H} \qquad (2.7)$$

where g_N and β_N are the nuclear g-factor and the nuclear magneton, respectively. The energy levels are given by,

$$E_m = -\mu H m_I / I = -g_N \beta_N H m_I \quad (2.8)$$

where $m_I = I, I-1, \ldots, -I$.

There are $(2I+1)$ equally spaced energy levels and the splitting between adjacent level is $g_N \beta_N H$. Transition between the sublevels of the excited state and those of the ground state are governed by selection rules. For magnetic dipole interaction, transitions (for ^{57}Fe) with $\Delta I = 1$, and $\Delta m_I = 0, \pm 1$ are allowed, giving six transitions as shown in figure 2.8.The net effective magnetic field is,

$$H_a - DM + (4\pi/3)M + H_S + H_L + H_D \quad (2.9)$$

where H_a is the external applied magnetic field, DM is the demagnetising field and $(4\pi/3)M$ is the Lorentz field.

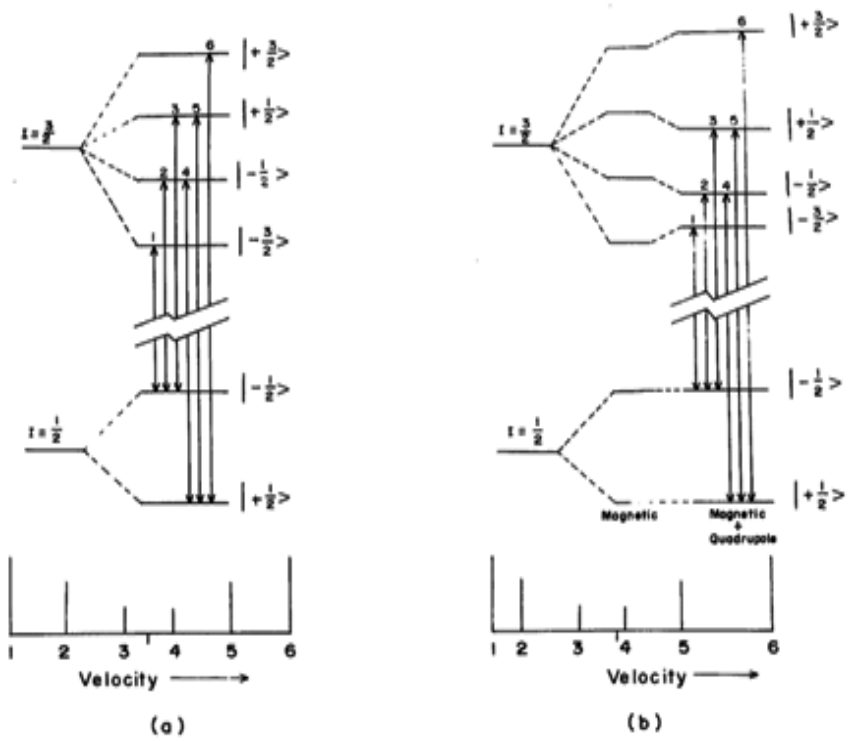

Figure 2.8 Magnetic dipole splitting (a) without electric quadrupole perturbation and (b) with electric quadrupole perturbation. The relative intensities of the transitions are given by the vertical bars at the bottom.

The Fermi contact interaction term H_S (arises due to a direct coupling of the nucleus with an imbalance in the s-electron spin density at the nucleus) and H_L refers to the contribution arising from non-zero orbital magnetic moment of the parent atom. The dipolar interaction of the nucleus with the spin moment of the parent atom is H_D.

2.5 Physical Property Measurement System (PPMS)

Magnetization, AC Susceptibility, DC resistivity and magneto-resistance are carried out using PPMS-6000 with a maximum field of 9T (Quantum Design). The principle and operation of each technique will be discussed one by one [16].

2.5.1 Vibrating Sample Magnetometer (VSM)

The VSM option for the PPMS (Quantum design, U.S.A) consists primarily of a VSM linear motor transport (head) for vibrating the sample, a coil set puck for detection, electronics for driving the linear motor transport and detecting the response from the pickup coils. The basic measurement is accomplished by oscillating the sample near a detection (pickup) coil and synchronously detecting the voltage induced from sample. The system is able to resolve magnetization changes even less than 10^{-6} emu.

The basic principle of operation for a vibrating sample magnetometer is a changing magnetic flux induces a voltage in a pickup coil. The time-dependent induced voltage is given by the following equation

$$V_{coil} = d\Phi / dt$$
$$= d\Phi / dz \quad dz / dt \qquad 2.10$$

In equation (2.10), Φ is the magnetic flux enclosed by the pickup coil, *z* is the vertical position of the sample with respect to the coil, and *t* is time. For a sinusoidally oscillating sample position, the voltage is based on the following equation

$$V_{coil} = 2\pi f C m A \sin(2\pi f t) \qquad (2.11)$$

In equation (2.11), *C* is a coupling constant, mis the DC magnetic moment of the sample, *A* is the amplitude of oscillation, and fis the frequency of oscillation. The acquisition of magnetic moment measurements involves measuring the coefficient of the sinusoidal voltage response from the detection coil.

2.5.2 AC Measurement System (ACMS)

The ACMS option has possibility to be used as both a DC magnetometer or an AC susceptometer. The ACMS contains an AC-drive coil set that provides an alternating excitation field and a detection coil set that

inductively responds to the combined sample moment and excitation field. The copper drive and detection coils are situated within the ACMS insert, concentric with the superconducting DC magnet of the PPMS. The drive coil is wound longitudinally around the detection coil set. The field amplitude that can be applied depends on the frequency of the alternating field and the temperature within the PPMS probe, but, at any temperature, the drive coil can generate alternating fields of up to ±10 Oe in a frequency range of 10 Hz to 10k Hz. Both the amplitude and phase of this response are reported. Alternatively, the ACMS can report the in-phase and quadrature components of the sample's response. The dynamic or ac susceptibility χ_{ac} = dM/dH, where dM is amplitude of change in magnetic moment and dH the amplitude of alternating field.

2.5.3 DC Resistivity and Magneto-resistance

The Resistivity option consists of a configurable resistance bridge board, called the user bridge board, to the Model 6000 PPMS Controller[16]. Samples for four-wire resistance measurements may be mounted on standard resistivity sample pucks. Resistivity sample pucks have four contacts, one positive and one negative contact for current and voltage for each user bridge board channel to which a sample may be conventionally wired. Up to three samples may be mounted on a resistivity puck, so the resistivity option can measure up to three

samples at one time. The resistivity of the samples can be measured as a function of temperature and also with and without applied field so that using this option one can measure the DC resistivity and also the Magneto resistance. The maximum compliance voltage of 95 mV with a minimum current of ±0.01 μamp sets an upper limit on the resistance value that can be measured.

2.6 Impedance spectroscopy

Impedance is a more general concept than resistance because it takes phase difference between current and voltage. Impedance spectroscopy is one of the powerful methods for studying the electrical properties of materials. To investigate the dynamics of bound or mobile charges in the bulk or in the interfacial regions of any kind of solids or liquid materials impedance analyzer is used [17-19]. The study of electrical conductivity (σ) and dielectric properties like dielectric constant, ε' and dielectric loss (tanδ) as a function of frequency is called as impedance spectroscopy. The processes (phenomenon in the material) can be represented by a complex combination of resistance (R), a capacitance (C) and an inductance (L). Agilent 4294A impedance analyzer is used with the frequency range of about 40 Hz to 1 MHz to collect the data. Two identical electrodes (silver paste) applied to the faces of a sample in the form of a circular pellet (rectangular also possible).

The applied a.c. voltage and the measured current in an electrical network are given by,

$$V(t) = V_0 \exp(j\omega t) \qquad 2.12$$

$$I(t) = I_0 \exp(j\omega t + \varphi) \qquad (2.13)$$

where ϕ is the phase angle and j = $\sqrt{-1}$.

The impedance $Z(\omega)$ of the circuit is given by

$$\begin{aligned} Z(\omega) = V(t)/I(t) &= |Z| \exp(-j\varphi) \\ &= |Z| \cos\varphi - j|Z| \sin\varphi \\ &= Z_r - jZ_i \end{aligned} \qquad (2.14)$$

Where Z_r and Z_i are the real and imaginary parts of the complex impedance.

The relations that relate these two quantities are,

$|Z| = \sqrt{Z_r^2 + Z_i^2}$ with $\tan\phi = Z_i / Z_r$

Conductance $\sigma_{ac} = Z_r / (Z_r^2 + Z_i^2)$.

The real and imaginary parts of the impedance of the samples are plotted in a complex plane and their frequency dispersion curves possess information about the effects of electrode - electrolyte interface,

grain and grain boundary resistances etc. In a parallel RC combination, the real and imaginary parts are,

$$Z_r = R/(1+(\omega RC)^2) \quad and \quad Z_i = \omega R^2 C/(1+(\omega RC)^2)$$

Elimination of $\omega$from the above equations leads to,

$$\left(Z_r - \frac{R}{2}\right)^2 + Z_i^2 = (R/2)^2 \quad \textbf{(2.15)}$$

which is the equation of a circle of radius $R/2$ with center at $(R/2,0)$ [17]. The typical impedance spectrum in the complex impedance plane corresponding to the circuit in figure 2.9(a) is shown in figure. 2.9(b).

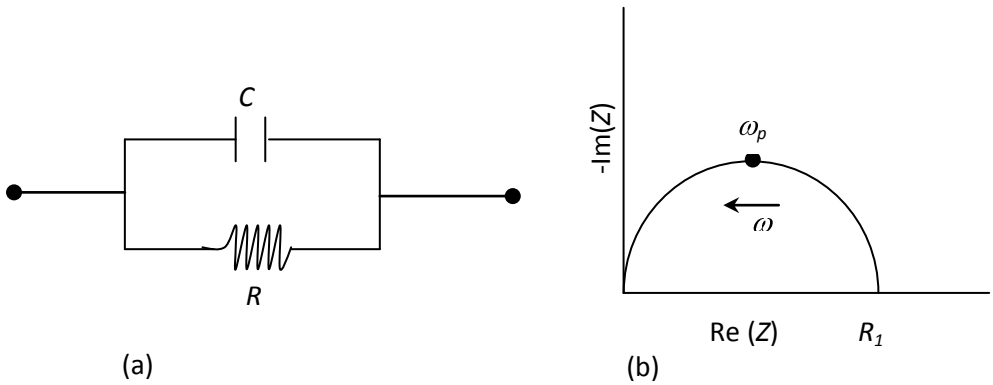

Figure 2.9. (a) A common RC circuit and (b) its impedance plane plot.

2.7 Thermogravimetric Analysis

Thermogravimetric Analysis (TGA) measures the amount and rate of change in the weight of a material as a function of temperature or time

in a controlled atmosphere. Measurements are used primarily to determine the composition of materials and to predict their thermal stability up to higher temperatures. Because most events that occur in a TGA are kinetic in nature (they are dependent on absolute temperature and time spent at that temperature), any experimental parameter like material type of the pan (shape and size), ramp rate, purge gas, sample mass, volume/form and morphology that can effect the reaction rate will change the shape / transition temperatures of the curve.

Thermo gravimetric (TGA) measurements are useful to study the phase transition, melting point, crystallization, glass transition and decomposition of the materials. TGA is used to find the weight loss with temperature of a sample. We used Mettler TGA (Model 851 LF). Weight is measured accurately with thermobalance and the controlled heating was achieved by a microfurnace (with an accuracy of ± 0.5 K) and the accuracy of the thermobalance is 0.10 μg. The maximum temperature that can be achieved in the furnace is 1350 °C. An inert gas atmosphere (N_2/Ar) is maintained for the balance chamber and the sample.

2.8 Field Emission – Scanning Electron Microscope

The grain size and surface morphology of the powder samples were investigated using Carl-Zeiss FESEM, model of Supra 40 VP. In this model combined with GEMINI- FESEM column with beam booster comprises three direct detection systems In-lens SE detector for high contrast topography, In-column EsB detector for low KV ultra-high resolution material contrast and Integrated annular AsB detector for compositional imaging. FE-SEM uses a field emission source producing a cleaner image with a spatial resolution < 2 nm.

The electrons generated by the Field emission source under the vacuum are accelerated in a field gradient and passes through electromagnetic lenses. This beam focuses and bombards the specimen resulting secondary electrons, back scattered electrons, auger electrons and others which are collected by the detector. The image of the sample surface is constructed by comparing the intensity of these secondary electrons to the primary electron beam and this is displayed on the monitor.

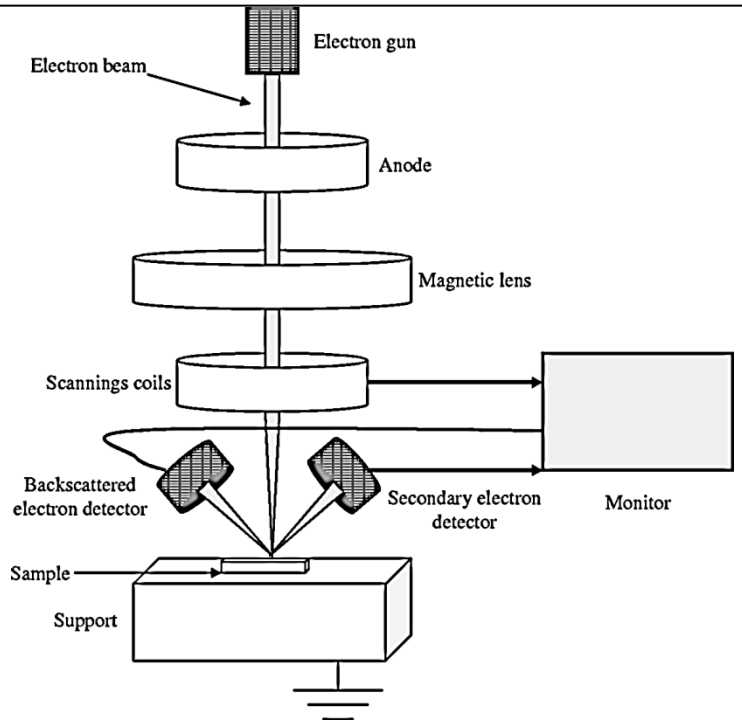

Figure 2.10. Schematic diagram of field emission scanning electron microscopy

The Schematic diagram of field emission scanning electron microscopy is shown in the figure.2.10. FE-SEM operates always under high vacuum (less than $1x10^{-7}$ Pa), which prevents electron scattering and discharges inside the instrument. The field emission electron Gun consists an emitter usually a Tungsten (W) wire fashioned into a sharp point of radius ~ 100 nm so as the electric field can be concentrated to an extreme level. This emitter is held at several kilovolts (1~30 KV) negative potential relative to a nearby electrode, so that there is sufficient

potential gradient at the emitter surface to cause field electron emission. A high energy (10-30 keV) electron beam, emitted from a tungsten tip is condensed to a spot diameter of 1-5 nm using electromagnetic lenses. The pair of scanning coils deflects the electron beam over the sample surface. This incident primary electron beam bombards the sample and cause low energy secondary electrons generation,which originates within a few nanometers from the surface.

The secondary electrons emitted from the sample are detected by a scintillator-photomultiplier device and signal is modified into a two-dimensional intensity distribution that can be viewed and saved as a digital image in a monitor. There are the high-energy electrons called as back scattered electrons, which are elastically scattered and essentially possess the same energy as the incident electrons.These are used to detect contrast between zones with different chemical compositions as they are emitted from a depth in the sample.

For specimen with poor electrical conductivity, a negative charge builds up gradually from bombardment by the high-energy electron beam. An abnormal contrast and splitting of the image result from the uneven distribution of the negative charge on the sample. A simple solution is to coat a very thin (generally 10 - 20 nm thick) gold layer on the sample's surface. It can enhance the emission of secondary and backscattered

electron, reduction of thermal damages as well as the elimination of charge accumulating effect.

Energy Dispersive Absorption of x-rays (EDAX) or Energy Dispersive x-ray analysis (EDX) is a method used to determine the energy spectrum of x-ray radiation emitted by a sample. It is a technique used for identifying the elemental composition of the specimen in an area of interest thereof. The EDAX attachment works as an integrated feature of a Field emission scanning electron microscope (FE-SEM), and cannot operate, on its own, without the FE-SEM. In addition, elemental analysis can be possible in two different ways. Based on energy called EDS and wavelength (WDS) up to the element Boron one can determine using this probe.

References

[1] B. D. Cullity, Elements of X-ray Diffraction (Ind. Ed.) (Addison-Wesley, 1977).

[2] Theo Hahn, International Tables for Crystallography , Volume A: Space-Group Symmetry, Published for The International Union of Crystallography by Springer (2005).

[3] K. Sköld and D. L. Price, Methods of Experimental Physics,Volume-23, Part A, Neutron Scattering, Academic Press, INC (1986).

[4] K. Sköld and D. L. Price, Methods of Experimental Physics,Volume-23, Part B, Neutron Scattering , , Academic Press, INC (1987).

[5] E. H. Kisi and C. J. Howard, Applications of Neutron Powder Diffraction, Oxford University Press (2008).

[6] JacekJ .Skrzypek and Franco Rustichelli, Innovative Technological Materials, Structural Properties by Neutron Scattering, Synchrotron Radiation and Modeling , Springer-Verlag, Berlin Heildelberg (2010).

[7] V. Siruguri, P. D. Babu, M. Gupta, A. V. Pimpale and P. S. Goyal, Pramana, J. Phys.71,1197-1201 (2008);

[8] S. S. Pande, S. P. Borkar, S. Prafulla, V. D. Shrivastava, A. Behere, P. K. Mukhopadyay, M.D. Ghodgaonkar and S. K. Kataria, Pramana ,J. Phys.63, 459 (2004).

[9] S. S. Pande, S. P. Borkar, A. Behere, S. Prafulla, V. D. Shrivastava, V. B. Chandratre, P. K.Mukhopadyay, M. D. Ghodgaonkar, P. S. R. Krishna, S. K. Paranjpe, M. Ramanadham, V. Siruguri and P. S. Goyal, BARC Newsletter 266, 2 (2006).

[10] V. G. Bhide, Mössbauer Effect and its Applications (Tata McGraw Hill, New Delhi, 1973).

[11] G. M. Bancroft, Mössbauer Spectroscopy: An Introduction to Inorganic Chemists and Geochemists (McGraw Hill, U.K. 1973).

[12] R. L. Mössbauer and M. J. Clauser, Hyperfine Interactions (Eds.) A. J. Freeman and R. B. Frankel, Academic Press Inc., New York, 1967), p 498.

[13] N. N. Greenwood and T. C. Gibb, Mössbauer Spectroscopy (Chapman and Hall, London, 1971).

[14] G. K. Wertheim, Mössbauer Effect: Principles and Applications (Academic Press, New York, 1964).

[15] V. I. Goldanskii and R. H. Herber, Chemical Applications of Mössbauer Spectroscopy (Academic Press, New York, 1968).

[16] PPMS-6000 (Quantum Design) User's Manual Part Number 1081-400 C1.

[17] J. Ross Macdonald (Ed.), Impedance Spectroscopy (Emphasizing Solid Materials and Systems) (John Wiley, New York, 1987).

[18] J. E. Bauerle, J.Phys. Chem. Solids **30** (1969) 2657.

[19] J.E. Randles, Discussion of Faraday Soc. **1** (1947) 11.

[20] Environmental Scanning Electron Microscopy, second ed. Philips Electron

Optics, Eindhoven, The Netherlands (1996).

CHAPTER 3

Structural characterization of $SrFe_{1-x}Ti_xO_{3-\delta}$ (x=0 to 0.3)

This chapter deals with the results of our studies on $SrFe_{1-x}Ti_xO_{3-\delta}$ (x=0 to 0.3) by x-ray diffraction, Neutron diffraction, Mössbauer spectroscopy and TGA techniques. The structural parameters like bond-length, bond angles and cation distribution in each coordination is established. With the help of low temperature Mössbauer and neutron diffraction, it is established that Fe occupies three different coordinations both crystallographically and magnetically.

3.1 Synthesis of $SrFe_{1-x}Ti_xO_{3-\delta}$ systems

$SrFe_{1-x}Ti_xO_{3-\delta}$ (x = 0 – 0.3) samples were prepared through solid state reaction route. Required molar ratio of $SrCO_3$, Fe_2O_3 and TiO_2 (procured from Sigma-Aldrich with the 99.9% purity) are taken and the mixed powder was milled up to 20 hours using planetary high-energy ball mill (Restch, PM-100) with zirconia vials and balls. The milling speed was 400 rpm with a ball to powder weight ratio of 8:1. The ground powders were calcined at 1000 °C for 24 hours. The calcined powder is again well ground (up to 1 hour) and pellets were made using hydraulic press with applied pressure of 15 ton per square inch (207 MPa). These pellets were sintered for 24 hours at 1200 °C in air, then samples are cooled under N_2 gas atmosphere up to 250 °C and at this temperature O_2 gas with 1 atm pressure flow is introduced for 48 hours. Oxygen flow is stopped and N_2 with 1 atm pressure flow is introduced and pellets are suddenly quenched from 250 °C to room temperature. One undoped $SrFeO_{3-\delta}$ and three different percentage of Ti^{4+} doped samples of 10%, 20% and 30% were chosen for further characterization which are labled as T0 (undoped), T1 (10% Ti), T2 (20% Ti) and T3 (30% Ti) [1-9].

3.2 Microstructure and composition analysis

The microstructure of the samples is studied using Field Emission Scanning Electron Microscope (FE-SEM) from Carl Zeiss and with combined EDAX attachment composition analysis is carried out. The chemical homogeneity of the samples is ensured by averaging the EDAX measurements taken from more than five different positions from the centre to the edges. The relative elemental concentration from EDAX spectra are normalized to the nominal composition of the starting materials. In T0 (undoped) system Sr to Fe ratio is close to one. In Ti doped systems Sr to Fe/Ti ratio comes very much close to one. The average particle size varies from 40 nm to 80 nm. Figure 3.1 shows the microstructure of all the samples T0 to T3 and Figure 3.2 shows the EDAX spectra taken on T1. Very good chemical homogeneity is seen in all the samples.

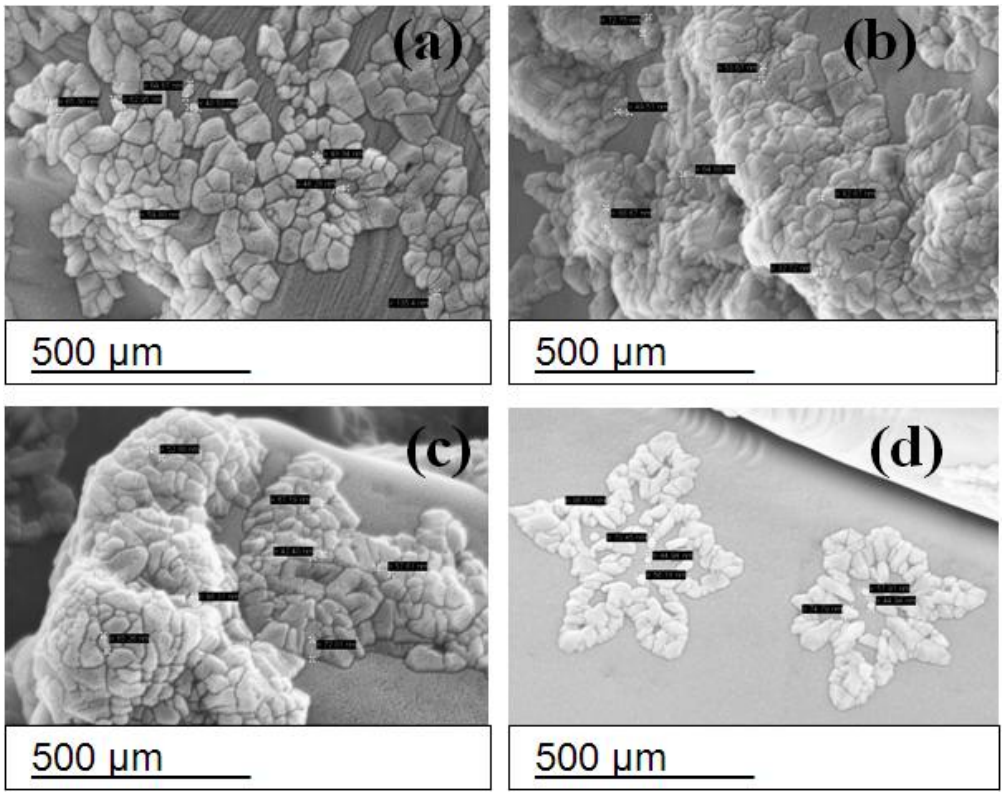

Figure 3.1 Microstructure of (a) T0 , (b) T1, (c) T2 and (d) T3

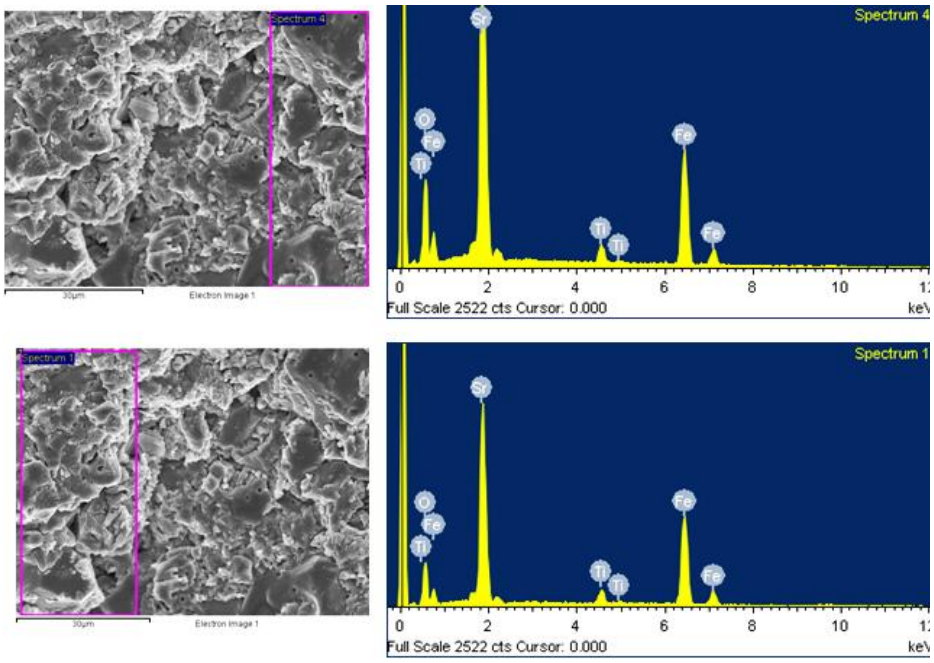

Figure 3.2 EDAX spectra taken on sample T1 in two different places.

3.3 Estimation of oxygen content

The oxygen content of all the samples are evaluated through TGA. $SrFeO_x$ is decomposed into $Sr_2Fe_2O_5$ at 1200°C [10] as follows.

$$2SrFeO_x = 2.5 + Sr_2Fe_2O_5 + (x-2.5)\,O_2$$

The value of x is calculated using the following equation,

$$x = 2.5 + \left[\frac{M_{Sr} + M_{Fe}}{M_O}\right] * \left(\frac{m_i - m_f}{m_f}\right) \qquad (3.1)$$

Where m_i is initial mass taken, m_f is final mass at 1200 °C, M_{Sr} is molecular weight of Sr, M_{Fe} is molecular weight of Fe and M_O is molecular weight of oxygen.

Figure 3.3 shows the TGA curve of $SrFeO_{3-\delta}$ from room temperature to 1200 °C and the measurement is done in an inert N_2 atmosphere with a heating rate of 10 °C per minute.

The oxygen stoichiometry of the undoped sample as determined from the TGA is found to be 2.87±0.01. The overall variation of oxygen across all the samples evaluated from TGA is found to be 2.86±0.02. This oxygen stoichiometry matches with the reported tetragonal $SrFeO_{3-\delta}$ [1, 2, 9-12].

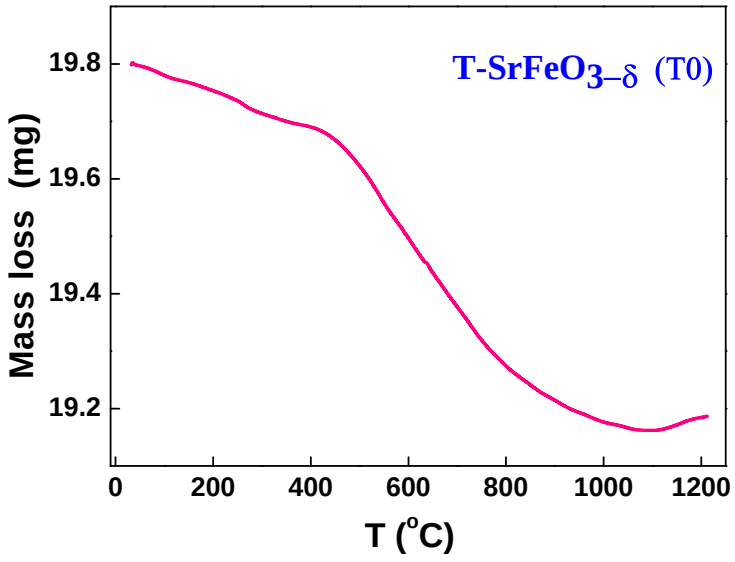

Figure 3.3 TGA measurement $SrFeO_{3-\delta}$ (T0) sample.

3.4 Crystal structure investigation from XRD pattern

Powders of sintered pellets were used to carry out x-ray diffraction (XRD) with an INEL diffractometer using Co Kα radiation. To get preliminary information of structure and phase confirmation x- ray diffraction (Figure 3.4) was carried out using Co Kα radiation with wavelength of 1.789 Å for all the samples. All the diffraction peaks are indexed ruling out the presence of any impurity or secondary phase. The diffraction pattern of all the samples closely matches with tetragonal structure. The reflection corresponding to (224) with Bragg angle of 62.50° has a relative intensity of less than 1%, (Ref: ICDD-PDF No-390954, λ= 1.788Å for $SrFeO_{2.86}$), is not observed in the undoped case.

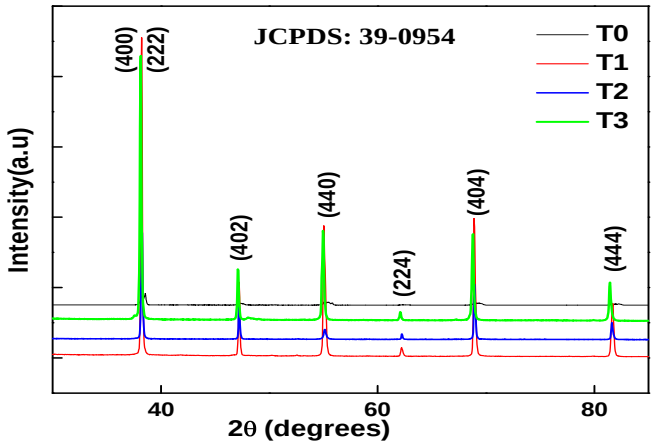

Figure 3.4 X-ray powder diffraction patterns of $SrFe_{1-x}Ti_xO_{3-\delta}$ systems using Co Kα source.

3.5 Rietveld refinement of Neutron Powder Diffraction (NPD) pattern and cation distribution in $SrFe_{1-x}Ti_xO_{3-\delta}$

Based on our XRD results and magnetization measurements (discussed in chapter 4) single phase samples are identified for neutron diffraction measurements. Neutron diffraction measurements are carried out using monochromatic wavelength of 1.48 Å in Bragg-Brentano geometry on $SrFe_{1-x}Ti_xO_{3-\delta}$ samples for x=0 - 0.3. Figures 3.5(a)-3.5(d) show the neutron diffraction spectra at RT for all the samples. To get the structural information (e.g cation distribution, site occupancy, atoms position coordinates, cell parameters, bond angle, bond length and Debye-Waller parameters) of these oxides Rietveld refinement is carried out. Diffraction profile matches well with the Thompson-Cox-Hastings pseudo-Voigt convoluted with axial divergence asymmetry function. Using FullProf suite the neutron diffraction data's are analyzed. Least square refinement weighting model is used in the Rietveld method to fit the experimental data. The refinement process continues till best fit of the entire calculated pattern to the entire observed pattern is matched. The quality of the agreement between observed and calculated values of individual intensities of various peaks are characterized by R-factors [13-15]. The numerical values of these R-factors indicate the goodness of

fit. Typically to accept the best fit value S_G should be less than 1.5. The following equations (3.2)-(3.5) defining the R-factors.

$$R_P = \frac{\sum \left| I_i(obs) - I_i(cal) \right|}{\sum I_i(obs)} \qquad (3.2)$$

$$R_e = \left[\frac{N - P}{\sum w_i I_i(obs)} \right]^{1/2} \qquad (3.3)$$

$$R_{wP} = \left\{ \frac{\sum w_i (I_i(obs) - (I_i(cal))^2}{\sum w_i I_i(obs)^2} \right\}^{1/2} \qquad (3.4)$$

$$S_G = \left\{ \frac{R_{wP}}{R_e} \right\} \qquad (3.5)$$

where R_P → R-pattern , R_{wP} →R-weighted pattern, R_e → R-expected, S_G →Goodness of fit and I_i is the intensity at "i" the Bragg reflection at the end of the refinement cycle. "obs" refers observed and "cal" refers calculated. N is the number of observations, P is the number of adjusted parameters and w_i is the observation weight.

3.6 Results and discussion of NPD

Diffraction profile matches well with the Thompson-Cox-Hastings pseudo-Voigt convoluted with axial divergence asymmetry function.

Using FullProf suite the neutron diffraction data's are analyzed. The initial atomic coordinates reported for the undoped (x = 0) tetragonal structure [16] are considered as an input for the refinement. Depending on the Oxygen stoichiometry considering the vacancy ordering the reported space groups (S.G) for Cubic is pm-3m, I4/mmm is for tetragonal and for Orthorhombic it is cmmm. For the doped system, initial refinement with the cubic, tetragonal and orthorhombic structures was carried out taking the reported initial parameters and space groups for tetragonal $SrFeO_{3-\delta}$ [16, 17].

All the three possible crystal structures are taken in to account and refined in similar way. Among these only I4/mmm fits well with experimental data. The simulated profiles using the other two space groups namely pm-3m (cubic) and cmmm (Orthorhombic) do not match with the experimental data. The main difference observed in the simulated profile using these two space groups and the experimental data are as follows. In the observed pattern 2θ ranges from 6 to 120° with equal steps of 0.037°. The generated pattern of cubic pm-3m has first Bragg reflection (110) at 22.26°, the second reflection (110) at 31.69° and third one (111) at 39.08°. But the observed spectrum for the T0 system has the first Bragg reflection at 2θ of 10.98° only which is indexed with (110) in I4/mmm space group and the observed pattern

has many more reflections at lower 2θ angles. The first reflection of orthorhombic CMMM is (110) at 13.49°. The observed Bragg reflections at 24.70° and 24.79° can be indexed only with I4/MMM space group of (310) and (112). Similarly at higher 2θ range, there are many reflections which can be indexed only with I4/MMM space group. In this pattern some of these observed Bragg reflection intensities at higher angles are very low and can be seen only at higher magnification scales. Apart from these observations, the overall goodness of fit also indicates that the measured profile can be refined only with the tetragonal structure with I4/MMM space group. Based on similar analysis it was found that the tetragonal structure with the space group I4/mmm is the only structure that matches closely with the experimental data even for systems with Ti doping up to 30%. The tetragonal structure determined for the present series of samples is in accordance with our x-ray and also TGA measurements confirming the oxygen stoichiometry. Atomic Displacement Parameters (ADP), position coordinates and Occupancy of all the systems are tabulated from Table 3.1-3.4. The calculated bond lengths and bond angles for all the samples are given in Table 3.5. The summarized bond length value of all the Fe coordination is tabulated in table 3.6. The fits generated using the Rietveld refined parameters and the difference between the experimental and the generated fits are shown in Figure 3.5(a)-3.5(d). Figure 3.6 shows the typical crystal

structure of tetragonal $SrFeO_{3-\delta}$ generated from refined coordinates. The Excellent fit between the observed data and simulated profile is obtained through Rietveld refinement with I4/mmm space group and S=1.235. According to the I4/mmm space group Fe occupies crystallographically three different sites, Sr occupies two different sites and oxygen occupies five different sites, given by the Wyckoff positions as shown in table 3.1 – 3.4. Out of the three Fe sites two of them are six oxygen coordinated octahedra sites namely Fe2 and Fe3 and the other one is five oxygen coordinated square pyramidal Fe1 site. The occupancy ratio of Fe1, Fe2 and Fe3 is 1:2:1 as suggested by the Wyckoff position. The valence states for different Fe sites are assigned in the original model of Hodges.et.al [16] based on the bond strength sum calculations combined with the Mössbauer analysis. Square pyramidal Fe1 and octahedral Fe3 sites were found to have 4+ valence and the Fe2 octahedra site has a mixed valence state of 3+ and 4+. The occupancy of Ti at different Fe sites can be arrived without any ambiguity from the neutron powder diffraction data due to the large variation in the scattering lengths of Fe (9.54 fm) and Ti (-3.438 fm). These values play an important role in the refinement providing a unique fit to the observed pattern. The occupation of Ti and its effect on the bond lengths and bond angles at different Fe sites is discussed below:

3.6.1 Square pyramidal Fe1 coordination

Fe1 exists in square pyramidal coordination, which has one Fe1-O1 bond and four Fe1-O2 bonds. Four O2 form the square base and O1 occupies the apex of the pyramid. The different Fe-O bond distances of the undoped system and Ti doped system are listed in Table 3.5. Compared to T0 system Fe1-O1 and Fe1-O2 bonds are elongated in the Ti doped T1, T2 and T3 systems. In all four samples Fe1-O1 bond length is longer than Fe1-O2 bond length and O1 is the apex oxygen of the square pyramid that is slightly above the base centre. Ti doped systems are expected to have elongated bonds because the atomic radius of Ti^{4+} (0.605 Å) is greater than that of Fe^{4+} (0.585 Å) 5% of Ti replaces Fe1 in T1 and T2 whereas in T3, 7% of Ti replaces Fe1. For a given system the bond lengths of Ti1-O1 and Ti1-O2 are same as Fe1-O1 and Fe1-O2 indicating that Ti1 replaces Fe1 site without changing the bond length and bond angle. However, with increase in Ti concentration there is an increase in the bond length and bond angle.

3.6.2 Octahedra Fe2 coordination

The octahedral Fe2 coordination comprises two Fe2-O2, two Fe2-O3 and two Fe2-O4 bonds. The complete Fe-O bond distances and bond angles of Fe2 octahedral site of all the samples investigated in this work are listed in the table 3.5. With increase in doping, contraction in Fe2-O2

bond length and elongation in Fe2-O3 bond length is observed compared to undoped system. In T1, none of the Ti atoms is occupying the Fe2 sites. In T2 10% of Ti occupies the Fe2 sites and in T3 around 14.5% of Ti atoms occupies the Fe2 sites.

3.6.3 Octahedra Fe3 coordination

Four Fe3-O4 and two Fe3-O5 bonds makes the Fe3 Octahedra coordination. In this coordination, two O4 and two O5 are forming a square base of octahedra with almost 90° to each corner oxygen atom. Other two O4 atoms occupy the apex of the octahedral making an angle O4 - Fe3 - O4 of 180°. In this coordination both Fe3-O4 and Fe3-O5 bonds are elongated compared to T0. In T1 case 5% of Fe3 atoms are replaced by Ti, in T2 system 5% of Fe3 atoms are replaced by Ti atoms and in T3 case 8.5% of Ti is occupied in Fe3 sites. Ti substitution makes no difference in the bond length and bond angles compared with Fe atoms in all the systems. In all the three Fe sites for a given doping, Ti replaces Fe without changing the bond lengths and bond angles.

The Lattice parameters of this system are given in table 3.7. It can be clearly observed that there is an increase in cell volume with increase in Ti doping and this is consistent as the size of Ti^{4+} is greater than that of Fe^{4+}.

The effective magnetic moment is estimated from the room temperature neutron measurements based on the site occupancy (not directly from the neutron diffraction pattern) of Fe in three different Fe sites obtained from the refinement. The spin only magnetic moment calculated for these valence states (for site 1 and 3 spin only moment of Fe^{4+} of 4.90 μ_B) and for site 2 an average moment of Fe^{3+} (spin only value of Fe^{3+} is 5.92 μ_B) and Fe^{4+} giving rise to 5.4 μ_B is multiplied with the corresponding occupancies to arrive at the total effective magnetic moment of the samples and listed in Table 3.3. The effective moment of undoped sample is 5.15 μ_B and with increase in Ti doping the effective moment decreases as expected due to the replacement of Fe^{4+} with non-magnetic Ti^{4+}.

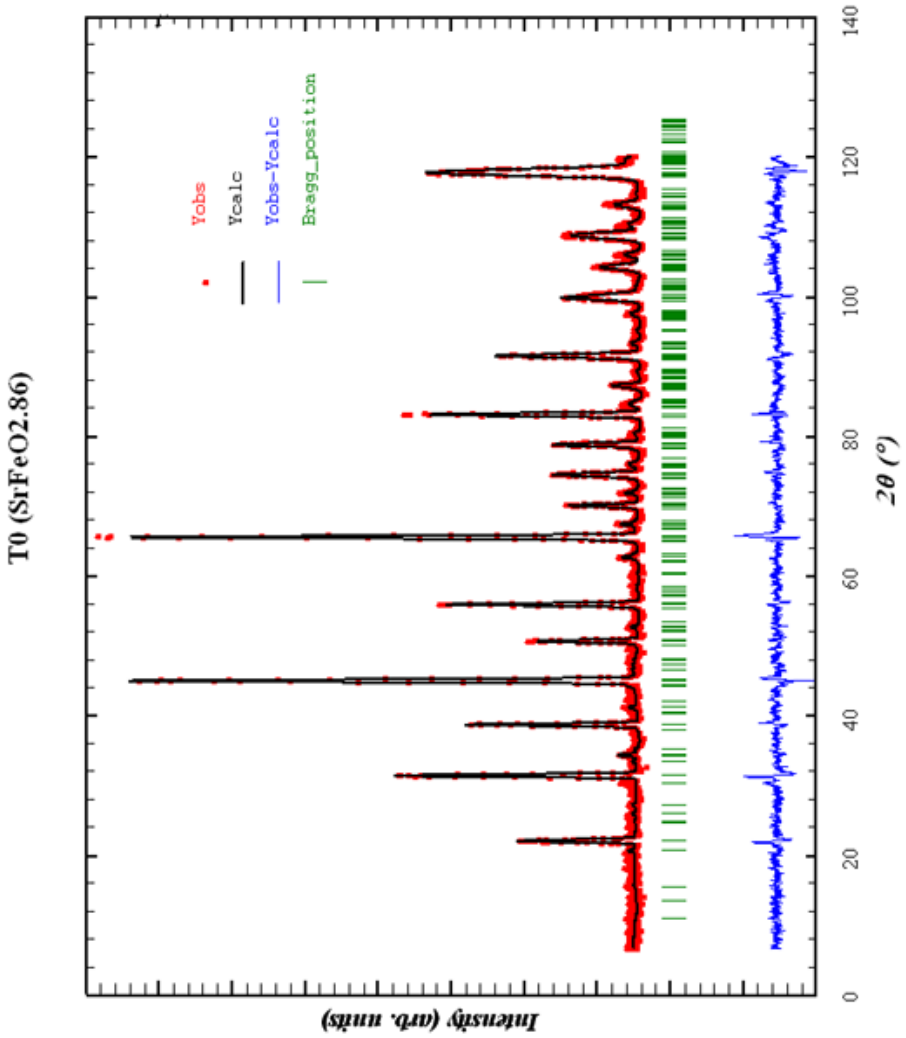

Figure 3.5a Rietveld refinement of neutron diffraction pattern recorded at room temperature of T0

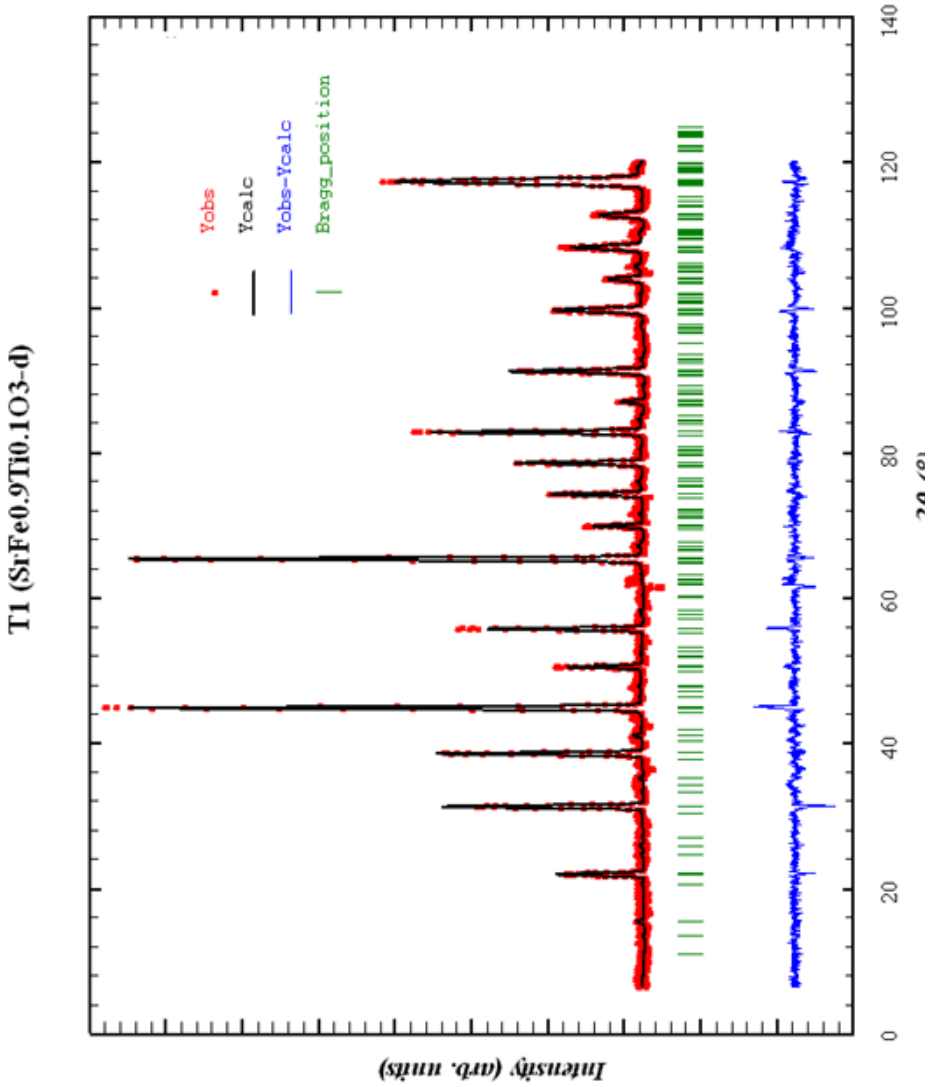

Figure 3.5b Rietveld refinement of neutron diffraction pattern recorded at room temperature of T1

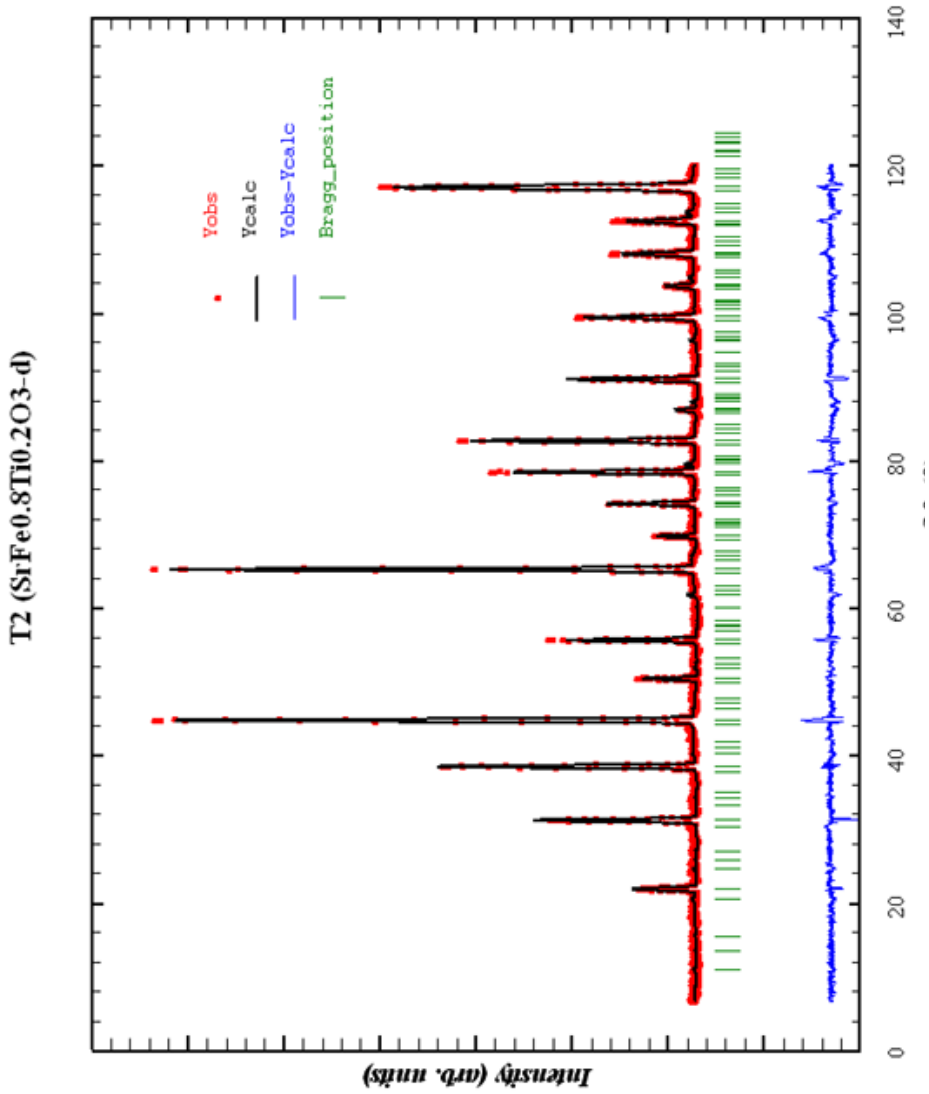

Figure 3.5c Rietveld refinement of neutron diffraction pattern recorded at room temperature of T2

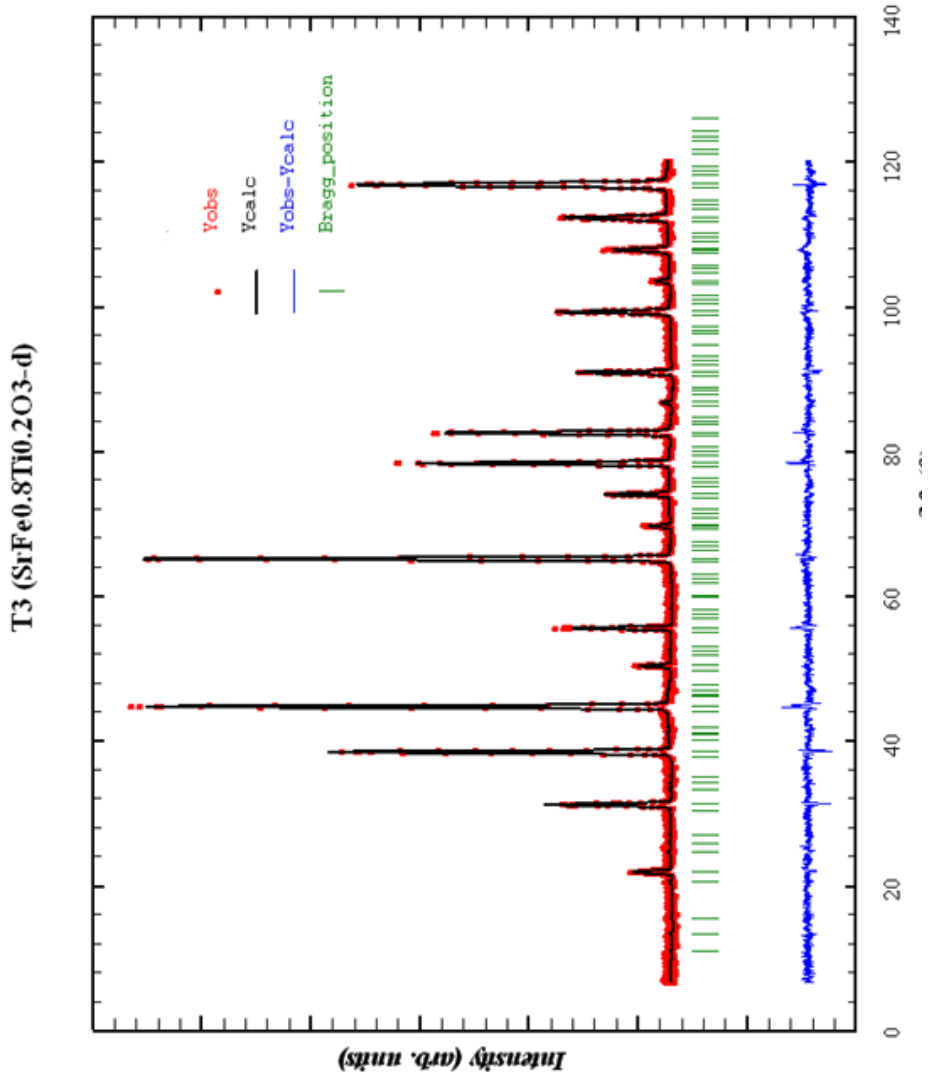

Figure 3.5d Rietveld refinement of neutron diffraction pattern recorded at room temperature of T3

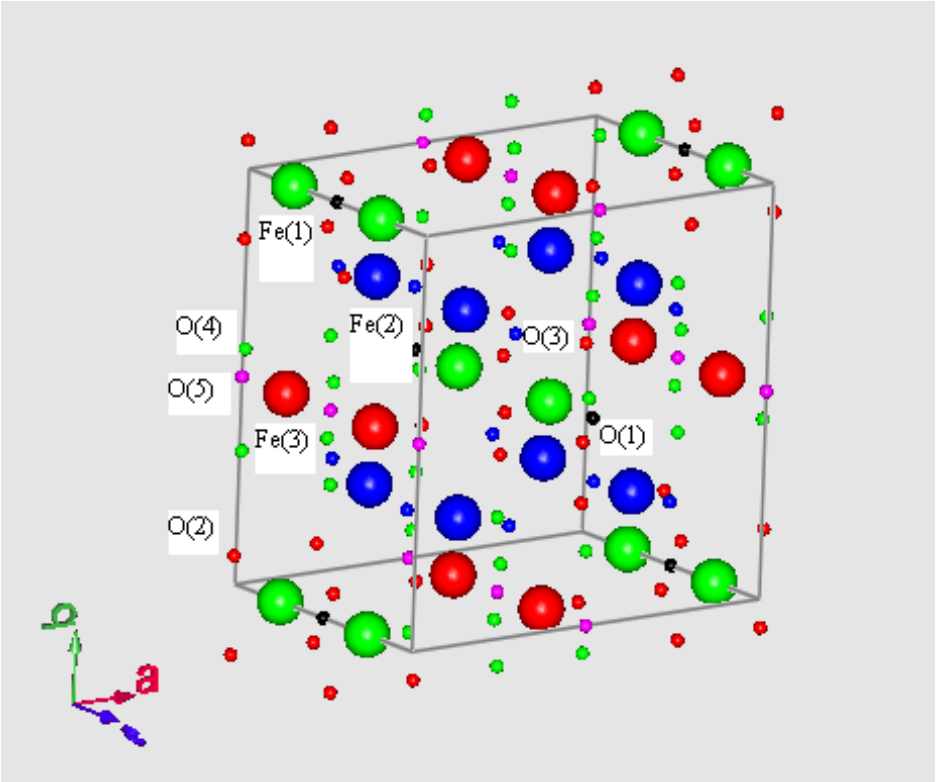

Figure 3.6 Typical crystal structure of tetragonal $SrFeO_{3-\delta}$ generated from refined coordinates. The legends for the above figure are: large circles- Fe1-Green, Fe2-blue, Fe3-red and small circles- O1-black, O2-red, O3-blue, O4-green, O5-pink.

Table 3.1 Structural parameters calculated from neutron diffraction patterns for T0. R values are R_P=19.2 ; R_{WP}=18.3 ; R_e= 14.8 ; S_G=1.235.

Atom	Site	x	y	z	U_{iso} (Å^2) x10^2	Occupancy
Sr(1)	8i	0.252(3)	0	0	0.690(2)	0.500
Sr(2)	8j	0.247(2)	1/2	0	0.568(1)	0.500
Fe(1)	4e	0	0	0.254(4)	0.353(4)	0.250
Fe(2)	8f	1/4	1/4	1/4	0.547(2)	0.500
Fe(3)	4d	0	1/2	1/4	0.490(3)	0.250
O(1)	2b	0	0	1/2	0.187(1)	0.124(2)
O(2)	16m	0.119(1)	0.119(1)	0.219(3)	0.056(2)	0.875(3)
O(3)	8h	0.268(2)	0.268(2)	0	0.970(2)	0.550(2)
O(4)	16k	0.1230	0.6230	1/4	1.208	1.125(2)
O(5)	4c	0	1/2	0	1.120	0.116(1)

Table 3.2 Structural parameters calculated from neutron diffraction patterns for T1. R values are R_p=20.4; R_{wp}=20.4; Re=5.91; S_G=3.451.

Atom	Site	x	y	z	U_{iso} (Å^2) x10^2	Occupancy
Sr(1)	8i	0.242(4)	0	0	0.322(2)	0.500
Sr(2)	8j	0.241(1)	1/2	0	0.322(2)	0.500
Fe(1) Ti(1)	4e	0	0	0.247(3)	0.316(1)	0.209(2) 0.040(4)
Fe(2) Ti(2)	8f	1/4	1/4	1/4	0.132(2)	0.500(2) 0.000
Fe(3) Ti(3)	4d	0	1/2	1/4	0.689(3)	0.188(3) 0.061(1)
O(1)	2b	0	0	1/2	1.639(2)	0.125(2)
O(2)	16m	0.123(2)	0.123(2)	0.256(3)	1.233(2)	1.000(2)
O(3)	8h	0.242(4)	0.242(4)	0	1.715(1)	0.485(1)
O(4)	16k	0.1239	0.6239	1/4	0.930(2)	1.000(2)
O(5)	4c	0	1/2	0	0.845(3)	0.250(4)

Table 3.3 Structural parameters calculated from neutron diffraction patterns for T2. R-Values are R_p=15.3; R_{wp} =14.1; R_e=6.84; S_G=2.061.

Atom	Site	x	y	z	U_{iso} (Å^2) x10^2	Occupancy
Sr(1)	8i	0.246(2)	0	0	0.556(4)	0.500
Sr(2)	8j	0.255(4)	½	0	0.556(2)	0.500
Fe(1) Ti(1)	4e	0	0	0.244(1)	1.749(3)	0.205(4) 0.044(3)
Fe(2) Ti(2)	8f	1/4	¼	1/4	0.055(2)	0.398(2) 0.101(4)
Fe(3) Ti(3)	4d	0	1/2	1/4	0.057(4)	0.202(4) 0.047(3)
O(1)	2b	0	0	1/2	1.739(5)	0.125(2)
O(2)	16m	0.124(4)	0.124(4)	0.245(4)	0.723(3)	1.000(5)
O(3)	8h	0.242(4)	0.242(4)	0	1.623(3)	0.485(3)
O(4)	16k	0.122(3)	0.622(3)	1/4	1.254(4)	1.000(3)
O(5)	4c	0	1/2	0	1.072(3)	0.250(2)

Table 3.4 Structural parameters calculated from neutron diffraction patterns for T3. R-Values are R_p=18.0; R_{wp}=16.0; R_e= 7.42; S_G=2.156.

Atom	Site	x	y	z	U_{iso} (Å^2) x10^2	Occupancy
Sr(1)	8i	0.248(2)	0	0	0.587(4)	0.500
Sr(2)	8j	0.250(3)	1/2	0	0.587(4)	0.500
Fe(1) Ti(1)	4e	0	0	0.249(5)	0.355(3)	0.178(6) 0.071(5)
Fe(2) Ti(2)	8f	1/4	1/4	¼	0.355(4)	0.355(2) 0.145(2)
Fe(3) Ti(3)	4d	0	1/2	1/4	0.355(3)	0.202(5) 0.047(4)
O(1)	2b	0	0	1/2	1.739(2)	0.125(3)
O(2)	16m	0.123(3)	0.123(3)	0.247(4)	0.723(5)	1.000(2)
O(3)	8h	0.250(1)	0.250(1)	0	1.623(2)	0.485(5)
O(4)	16k	0.124(2)	0.625(2)	1/4	1.254(4)	1.000(3)
O(5)	4c	0	1/2	0	1.072(3)	0.250(5)

Table 3.5 Calculated bond angles and bond lengths obtained from neutron diffraction measurements.

System	Square pyramidal Fe(1)site	Octahedral Fe(2) site	Octahedral Fe(3) site
T0	O1-Fe1-O2 : 99.4 (3) x1 O2-Fe1-O2 : 88.4 (2) x2 O2-Fe1-O2 : 161.0(2) x2 Fe1-O1 : 1.891(2) x1 Fe1-O2 : 1.881(2) x4 O1-O2 : 2.879 (3) O2-O2 : 2.624(2)	O3-Fe2-O3 : 180 (5) x2 O3-Fe2-O4 : 89.9 (5) x4 Fe2-O2 : 2.030 (3) x2 Fe2 -O3 : 1.927 (4) x2 Fe2-O4 : 1.964 (2) x2 O3-O4 : 2.751(3) O2-O4 : 4.061(3)	O4- Fe3-O4 : 180 (4) x3 O4-Fe3-O4 : 89.9 (5)x2 O4-Fe3-O4 : 90 (5)x2 O4-Fe3-O5 :89.9 (3)x10 Fe3-O4 : 1.903 (4) x4 Fe3-O5 : 1.926 (5) x2 O4-O4 : 3.807 (3) O4-O5 : 2.708 (4)
T1	O1-Fe1-O2 : 87.9(2) O2-Fe1-O2 : 89.9 (2) Fe1-O1 : 1.959 (3) x1 Fe1-O2: 1.917 (3) x4 Fe1-O1 : 1.959 (4) Fe1-O2 : 1.917 (4) O1-O2 : 2.693(2) O1-Ti1-O2 : 87.9(2) O2-Ti1-O2 : 89.9(3) O2-Ti1-O2 : 175.9 (2) Ti1-O1 : 1.959 (2) x1 Ti1-O2 : 1.917 (3)x4	O2-Fe2-O2: 180 (2) O2-Fe2-O3: 88.1(2) O2-Fe2-O3: 91.8 (2) O2-Fe2-O4: 90.0 (4) O3-Fe2-O4: 89.9 (4) O2-Fe2 : 1.955 (2) O2-O2 : 3.911 (4) Fe2-O2 : 1.955 (3) x2 Fe2-O3 : 1.942 (3) x2 Fe2-O4 : 1.952 (4) x2	O4-Fe3-O4: 180 (3) O4-Fe3-O4: 90 (3) O4-O4 : 3.838 (5) Fe3-O4 : 1.919 (5) x4 Fe3 -O5 : 1.939 (3) x2 O4-Ti3-O4: 180.0 (3) O4-Ti3-O4: 90.0 (3) Ti3-O4 : 1.919 (4) x4 Ti3-O5 : 1.939 (4)x2 O4-O4 : 3.838 (5)
T2	O1-Fe1-O2: 89.8(2) O2-Fe1-O2: 179.6(3) Fe1-O1 : 1.981 (1) x1 Fe1-O2: 1.939 (2)x4 O1-Ti1-O2 : 89.8(3) O2-Ti1-O2 : 179.6(4) O2-Ti1-O2 : 175.9 (2) Ti1-O1 : 1.981(2) x1 Ti1-O2 : 1.939 (3) x4 O1-O2 : 2.768(4) O2-O2 : 3.878(4)	O2-Fe2-O2: 180 (3) O2-Fe2-O3: 85.6 (3) O2-Fe2-O4: 90.0 (4) Fe2-O2 : 1.941 (4) x2 Fe2-O3 : 1.942 (4)x2 Fe2-O4 : 1.971 (5)x2 O2-O2 : 3.882(3) O2-Ti2-O2 : 180.00 (2) O2-Ti2-O3 : 85.68 (3) O2-Ti2-O4: 90.00 (3) Ti2-O2: 1.941 x2 (2)	O4-Fe3-O4: 180 (2) O4-Fe3-O4: 90 (2) Fe3-O4 : 1.908 (4) x4 Fe3 -O5 :1.939 (4)x2 O4-Ti3-O4: 180 (3) O4-Ti3-O4: 90 (3) Ti3-O4 : 1.908 (5)x4 Ti3-O5 : 1.939 (4)x2 O4-O4 : 3.817 (2) O4-O5 : 2.721(3)

		Ti2-O3:1.942 x2 (2) Ti2-O4:1.971 x2 (4)	
T3	O1-Fe1-O2: 90.5 (4) O2-Fe1-O2: 89.9 (5) O2-Fe1-O2 : 178.8 (4) Fe1-O1 : 1.942 (3) x1 Fe1-O2: 1.925 (3) x4 O1-Ti1-O2: 90.5 (4) O2-Ti1-O2: 89.9 (5) O2-Ti1-O2: 178.8 (4) Ti1-O1 : 1.942 (2) x1 Ti1-O2 : 1.925 (2) x4 O1-O2 : 2.749(5) O2-O2 : 3.851(5)	O2-Fe2-O2: 180 (5) O2-Fe2-O3: 90.5 (5) O2-Fe2-O4: 89.9 (3) Fe2-O2 : 1.959 (4) x2 Fe2-O3 : 1.942 (4) x2 Fe2-O4 : 1.942 (5) x2 O2-O2 : 3.918 (3) O2-Ti2-O2 : 180 (3) O2-Ti2-O3 : 89.4 (5) O2-Ti2-O4: 90 (4) Ti2-O2: 1.959 (4) x2 Ti2-O3: 1.942 (5) x2 Ti2-O4: 1.942 (5)x2	O4-Fe3-O4: 180 (3) O4-Fe3-O4: 89.9 (4) Fe3-O4 : 1.942 (5) x4 Fe3 -O5 :1.942 (5) x2 O4-Ti3-O4: 180 (4) O4-Ti3-O4: 89.9 (4) Ti3-O4 : 1.942 (3) x4 Ti3-O5 : 1.942 (5)x2 O4-O4 : 3.884 (4) O4-O5: 2.746 (5)

Table 3.6 Bond length between Fe and O atoms of different crystallographic sites (named as Fe1, Fe2 and Fe3) calculated from neutron diffraction data with Bond-Valence Sum rule (number in the brackets indicates number of bonds associated). (Summarized value of Bond lengths from table 3.5)

Systems	Fe1-O1(Å) (1)	Fe1-O2 (Å) (4)	Fe2-O2(Å) (2)	Fe2-O3(Å) (2)	Fe2-O4 (Å) (2)	Fe3-O4 (Å) (4)	Fe3-O5 (Å) (2)
T0	1.891	1.881	2.030	1.927	1.964	1.903	1.926
T1	1.959	1.917	1.955	1.942	1.952	1.919	1.939
T2	1.981	1.939	1.941	1.942	1.971	1.908	1.939
T3	1.942	1.925	1.959	1.942	1.942	1.942	1.942

Table 3.7 Lattice parameters calculated from neutron diffraction patterns

System	Lattice constant a=b(A°)	c(A°)
T0	10.940 (2)	7.706 (3)
T1	10.950 (1)	7.756 (2)
T2	10.974 (2)	7.757 (2)
T3	10.988 (3)	7.768 (1)

3.7 Mössbauer studies on $SrFe_{1-x}Ti_xO_{3-\delta}$

Room temperature and low temperature transmission mode Mössbauer effect spectra (ME) are recorded to probe the valence and spin states (low or high) of each Fe site locally. ^{57}Fe source Mössbauer spectrometer with transmission geometry is used to record Mössbauer spectrum. The resultant spectra are fitted with Lorentzian shape using least squares program valence state of Fe is assigned based on WWJ model [18-21] (Walker, Wertheim and Jaccarino) taking into account our calculated values of Isomer Shift(IS), Hyperfine Field(H_{BF}), Quadrupole Splitting(QS) and comparing with the corresponding reported values. In order to compare the present results with those reported in literature a brief account of different studies is given here. The room temperature ME spectra of tetragonal $SrFeO_{2.86}$ by Takeda et al [1,2] has one singlet with Fe in 4+ high spin state and one doublet with Fe in 3.5+ state which is interpreted as resulting due to the fast electron transfer between Fe^{4+} and Fe^{3+}. Their low temperature data at 5 K on the same sample has three components. Among the three components one is very broad absorption spectra which is unassigned state and other two states are assigned as (4+δ) and (4-δ). Lebon et al [22,23] used single crystal of $SrFeO_{3-\delta}$ with different δ values. The single crystal samples also has mixed phases with a minimum of two compositions. $SrFeO_{2.87}$ has one

singlet with Fe in 4+ and one doublet with Fe in 3.5+ which is a mixed phase of 81% tetragonal and 19% of cubic. $SrFeO_{2.81}$ has one singlet with Fe in 4+ and two doublets of Fe in 3.5+ and 3+ which consists mixed phases of 76% tetragonal and 24% of orthorhombic.

In the present study, the room temperature Mössbauer spectra of all the four systems (Figure 3.7 and 3.8) have the common feature of one singlet and two doublets, which is a signature of existence of Fe in three different coordinations. Sub-spectra 1 (singlet) in T0 has QS=0 with IS=-0.0824 mm/s is an indication of Fe in cubic environment with six oxygen coordination. This Fe site is assigned with 4+ state with one of the octahedra coordination.

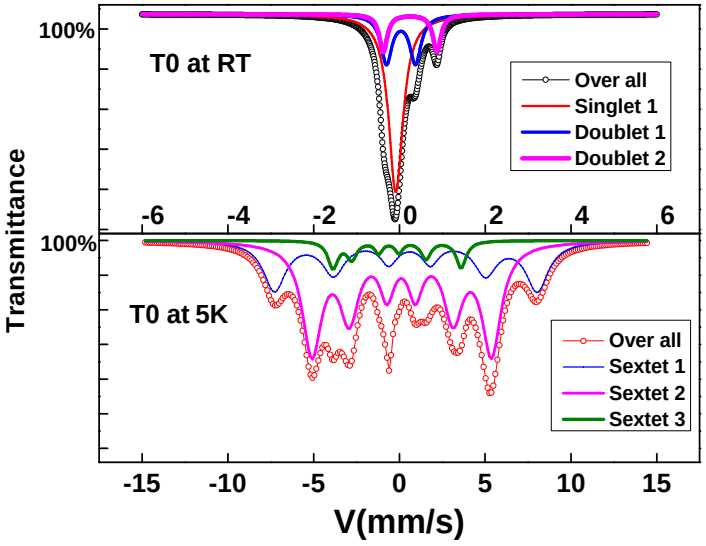

Figure 3.7 Mossbauer spectrum of T-$SrFeO_{3-\delta}$ (T0) recorded at RT and 5K with ^{57}Co source in transmission mode

Sub-spectra 2 (doublet1) in T0 has low IS and QS with the values of IS and QS are 0.0374 mm/s and 0.6766 mm/s respectively is a signature of Fe in 4+ in square pyramidal coordination. Sub-spectra 3 (doublet2) in T0 has higher value of IS and QS (IS=0.2504 mm/s and QS=1.25 mm/s) is in between the 3+ and 4+ or it can be assigned the average value of 3.5+.

In T0 system data collected at 5K (Figure 8 bottom one) has three sextet of different Isomer shifts and Hyperfine field (Bhf) values. The sextet 1 (C1) has the (IS= 0.489mm/s) hyperfine field of 47.4 T, with large quadrupole splitting. In this Fe site, 3d electrons are screening the 4s electrons more and has a large isomer shift. This indicates that Fe is in high spin state with 3+. Sextet 2 (C2) has IS=0.122 mm/s and the hyperfine field value of 32.4 T with small quadrupole interaction (QS). Small QS indicates that almost all the charge distribution is symmetrical indicating octahedral symmetry. Sextet 3 (C3) has hyperfine field value of 23.15 T only, which is lower than the hyperfine field value of the other two components. Sextet 3 has IS (-0.37 mm/s) value which means that the electronic configuration $4s^2 3d^4$ of Fe^{4+} is modifying as $4s^{2-x} 3d^{4+x}$. In that situation s electron sees more screening effects at the nucleus and the s electron density is decreasing which is reflected as a high IS value [24-26].

The ME results of Ti doped samples [27, 28] are also analyzed in terms of presence of one singlet and two doublets (figure 3.8). Component1 (singlet) in T1 has low value of both IS and QS (IS=-0.0709 mm/s and QS=-0.1763 mm/s) indicates the presence of Fe in 4+ (cubic symmetry of Fe) with octahedra coordination. Component 2 (doublet 1 in T1) has low IS and moderate QS due to square pyramidal coordination of Fe in 4+ state. Component 3 (doublet 2 in T2) has higher value of IS and QS is due to Fe in 3.5+ state. In T2, component 1 (singlet) has low value of IS and QS (IS=-0.0638 and QS=0.1658), similar to the above, which can be interpreted due to the presence of Fe in 4+ state with octahedra environment. Component 2 (C2, doublet 1 in T2) has low value of IS and moderate value of QS refers to Fe in 4+ state with square pyramidal coordination. The value of IS and QS of component 3 (doublet2 in T2) indicates that Fe has an average valence of 3.5+. T3 system also has the similar situation like the above discussed with three Fe sites having three different IS and QS values.

Alder.et.al [28] reported ME studies on Ti doped $SrFeO_{3-\delta}$ samples. Most of their samples are high pressure annealed and structurally cubic phases.

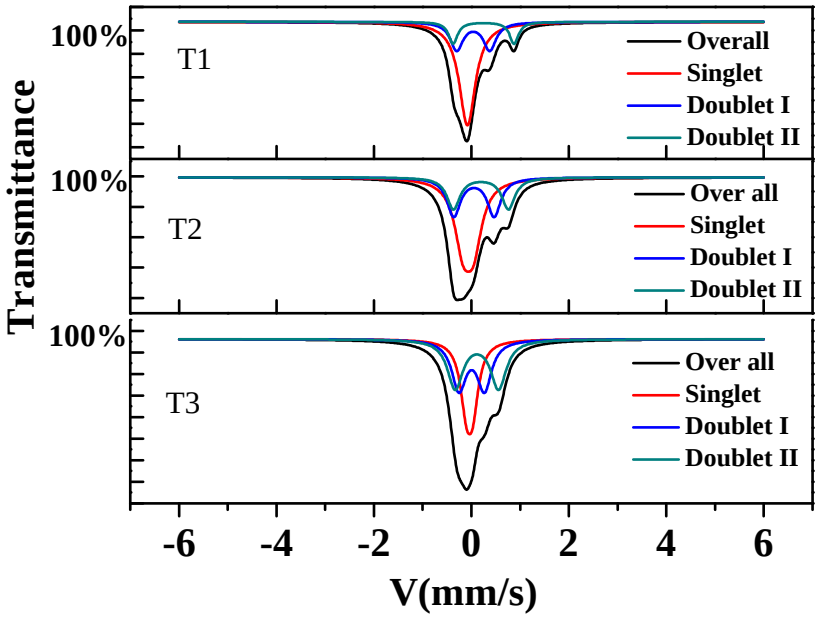

Figure 3.8 Mossbauer spectrum of $SrFe_{1-x}Ti_xO_{3-\delta}$ (x=0.1 to 0.3) recorded at room temperature.

In the above studies Fe is in 4+ with 10% Ti doped and two singlets are observed in 30% Ti doped samples having valence of 4+ and 3+. The same group prepared air annealed sample which has a tetragonal structure. This tetragonal sample is found to have one singlet of Fe in 4+ state and two doublets of Fe in 3+ state. The present study on these tetragonal samples show two Fe sites with 4+ state and one with 3.5 state and this result matches well with our neutron results.

Table 3.8 Mössbauer Parameters such as isomer shift (I.S), quadrupole splitting (Q.S.), hyperfine magnetic field (Bhf), linewidth (W.V.) and sub-spectra relative intensities obtained from least squares fitting.

System	Sub-spectra	I.S (mm/s)	Q.S(mm/s)	W.V(mm/s)	Bhf (T)	% Area	Val. state
T0 (RT)	S- C1 D-C2 D- C3	- 0.08238 0.03744 0.25045	0 0.67666 1.25040	0.40496 0.77580 0.54806	---- ---- ----	60.56 25.39 14.03	Fe^{4+} Fe^{4+} $Fe^{3.5+}$
T0 (5K)	Se-C1 Se- C2 Se- C3	0.489 ±0.039 0.122±0.013 -0.374 ±0.054	-0.217 ±0.062 0.033 ±0.025 0.479 ±0.063	1.21 ±0.105 1.04 ±0.037 0.54 ±0.13	47.42 ±0.24 32.42 ±0.12 23.15 ±0.30	31.1 60.0 8.9	Fe^{3+} (HS) Fe^{4+} (HS) Fe^{4+}
T1 (RT)	S-C1	-0.07094	-0.17633	0.35746		49.89(45)	Fe4+(HS)
	D-C2	0.01996	0.70039	0.87809		32.34(29)	Fe4+(HS)
	D-C3	0.16281	0.90295	1.07828		17.76(16)	Fe3.5+
T2 (RT)	S-C1	-0.06386	0.16581	0.39043		49.77(40)	Fe4+
	D-C2	0.05237	0.75995	0.80545		24.44(19)	Fe4+
	D-C3	0.19586	1.01553	0.96223		25.78(21)	Fe3.5+
T3 (RT)	S-C1	-0.03779	-0.13178	0.29209		31.60(22)	Fe4+
	D-C2	0.00540	0.52147	1.21741		32.89(23)	Fe4+
	D-C3	0.11254	0.88849	1.31789		35.50(25)	Fe3.5+

S – Singlet; D – Doublet; Se – Sextet; C1, C2, C3 - Components

Table 3.9 Effective magnetic moment values obtained from different experimental techniques and T_b indicates the bifurcation in FC-ZFC.

Systems	Magnetization (μ_B)	Mossbauer(μ_B)	Neutron(μ_B)	T_b(K)	θ(K)
T0	5.30(2)	5.04(3)	5.36(2)	74	-3.3
T1	4.54(1)	4.57(4)	4.81(3)	45	21.2
T2	4.33(2)	4.12(5)	4.70(2)	39	21.9
T3	4.10(3)	3.67(3)	3.77(1)	33	23.9

The estimated oxygen stoichiometry in these samples based on the area proportions of different valence states matches well with TGA analysis. The effective magnetic moment of all the samples is calculated from the area fractions of Fe^{4+} and Fe^{3+} high spin states (normalized with the percentage of Fe present in the doped system, given in brackets in Table 3.8) and the values are listed in Table.3.9. The values of effective magnetic moments are in close agreement with those obtained from magnetization (C-W analysis of magnetization data well above T_N) and room temperature neutron measurements. This proves that both the crystal structure and the magnetic structure of these systems are solved consistently assuming three Fe sites which are different both crystallographically as well as magnetically. Consistent with the previous reports, we see that there is a systematic decrease in isomer shift (IS) with increase in Ti doping which is attributed [28] to the increase in Ti^{4+} and Fe^{3+}.

3.8 Conclusion

Tetragonal $SrFe_{1-x}Ti_xO_{3-\delta}$ (x=0 to x=0.3) are synthesized using solid state reaction. The crystal structure and the structural parameters are determined using an elaborate x-ray and neutron data analysis. The Ti doped samples for x up to 0.3 belong to the I4/mmm space group. The cell volume increases with increase in Ti doping, consistent with the increase in size of Ti^{4+} in comparison to the Fe^{4+}. Detailed magnetization measurements reveal the decrease in the bifurcation temperature T_b and also effective magnetic moment with increase in Ti doping. The low field magnetization of the Ti doped samples indicates spin glass behaviour. ME studies together with neutron analysis on these tetragonal systems establishes that Fe exist structurally and also magnetically in three different sites. The effective magnetic moment values obtained from neutron, magnetization and ME studies has a close agreement verifying the assignment of Fe valence state and establishing the cation distribution in different sites.

References

[1] Y.Takeda, K.Kanno ,T.Takada, O.Yamamoto, M.Takano, N.Nakayama and Y.Bandol, J.Solid State Chemistry 63(1986) 237.

[2] M.Takano, T.Okita, N.Nakayama, Y.Bando, Y.Takeda, O.Yamamoto and J.B.Goodenough, J.Solid State Chemistry 73(1988) 140.

[3] Junichiro Mizusaki , Masanobu Okayasu, Shigeru Yamauchi, KazuoFueki, Journal of Solid State Chemistry, 99,166 (1992).

[4]A.Wattiaux , L.Fournes, A.Demourgues, N.Bernaben, J.C.Grenier, andM.Pouchard, , Solid State Communications, 77,489 (1991).

[5] Naoaki Hayashi, Takahito Terashima and Mikio Taano, J.Mater.Chem, 11, 2235(2001).

[6] Stefanie Schott, Zhihong Jia, Andreas K.Schaper, Venkataraman Thangadurai, Werner Weppner and Peter Schmid-Beurmann, Physica Status Solidi (a), 202 ,2330 (2005).

[7] P.K.Gallagher ,J.B.Mac Chesney and D.N.E.Buchanan, The Journal of Chemical Physics 41 (1964) 2429.

[8] L.H.Brixner, Mater.Res.Bull 3 (1968) 299.

[9] M.Schmidt , Mater.Res.Bull 35(2000) 169.

[10] Phase formation and structural transformation of Strontium ferrite SrFeOx, Marek Wojciech Schmidt, thesis to The Australian National University.

[11] M.Schmidt, Journal of Physics and Chemistry of Solids 61 (2000) 1363.

[12] M.Shmidt, Mater.Res.Bull 37 (2002) 2093.

[13] H. M. Rietveld, J. Appl . Crystallo gr. 2, 65 (1969).

[14] R.A. Young, The Rietveld Method ,Oxford IUCr/OUP (1995)

[15] G. Bagon Neutron Diffraction ,Oxford, 3rd edition (1989)

[16] J.P.Hodges , S.Short, J.D.Jorgensen, X.Xiong,B.Dabrowski, S.M.Mini and C.W.Kimball Journal of Solid State Chemistry 151(2000) 190.

[17] M. Schmidt, M. Hofmann, and S. J. Campbell, J. Phys.: Condens.

Matter 15, 8691 (2003)

[18] Mossbauer Spectroscopy by N.N.Greenwood and T.C.Gibb "Chapman and Hall Ltd.London" (1971)

[19] R. L. Mössbauer and M. J. Clauser, Hyperfine Interactions (Eds.) A. J. Freeman and R. B. Frankel, Academic Press Inc., New York, 1967), p 498.

[20] G. K. Wertheim, Mössbauer Effect: Principles and Applications (Academic Press, New York, 1964).

[21] V. I. Goldanskii and R. H. Herber, Chemical Applications of Mössbauer Spectroscopy (Academic Press, New York, 1968).

[22] A.Lebon, P.Alder, C.Bernhard, A.V.Boris, A.V.Pimenov, A.Maljuk, C.T.Lin, C.Ulrich and B.Keimer Phy.Rev.Lett. 92(2004) 037202.

[23] P. Adler,A. Lebon,V. Damljanovi C. Ulrich, C. Bernhard, A. V. Boris, A. Maljuk, C. T. Lin,and B. Keimer Phys.Rev.B 73, 094451 (2006).

[24] Y.M. Zhao,R.Mahendiran, N. Ngugen, B. Raveau and R.H. Yao, Phys.Rev.B 64, 024414 (2001).

[25] P.D.Battle , T.C.Gibb and S.Nixon Journal of Solid State Chemistry 79 (1989) 75.

[26]T. C. Gibb, J. Chem. Soc., Dalton Trans . 1455 (1985)

[27] Peter Alder and Sten Eriksson Z.Anorg. Allg. Chem. 626 (2000) 118.

[28] J.Rodriguez, J.A.Pereda, M.Vallet, J.G.Calbet and J.Tejada Mater.Res.Bull 21(1986) 255

.

CHAPTER 4

Magnetization studies of $SrFe_{1-x}Ti_xO_{3-\delta}$ Systems

This chapter describes the results of the studies on $SrFe_{1-x}Ti_xO_{3-\delta}$ (x=0 to 0.3) by AC Susceptibilty, Magnetization, and low temperature Neutron diffraction techniques. Based on all the three sets of data, it is established that the undoped system exhibits the long-range helical antiferromagnetic order while the Ti doped systems behave as a cluster spin-glass.

4. 1. Introduction

$SrFeO_3$ has attracted considerable attention in the recent past due to the exciting electric and magnetic properties. $SrFeO_{3-\delta}$ ($\delta = 0$) with Fe in its 4+ (d^4) high spin (HS) state shows metal-like conductivity. However, the strong Fe^{4+}-O^{2-}-Fe^{4+} superexchange interactions produce an antiferromagnetic state with a Neèl temperature around 130 K. Oxygen non-stoichiometry forces some of the Fe^{4+} ions in to Fe^{3+} valence state and in addition, presence of oxygen vacancies could induce considerable strain in the lattice, making the structural transformation possible. Higher values of δ produce a change in the crystal structure from a simple cubic to a lower symmetry (cubic → tetragonal → orthorhombic). The symmetry first changes to tetragonal (at $\delta = 0.125$) which is a helical antiferromagnet with T_N close to 76 K and to an orthorhombic structureat higher values of $\delta \approx 0.25$) which sustains antiferromagnetic order with T_N = 232 K. At higher concentrations ($\delta > 0$), the FeO_6 octahedra give way to a series of octahedra that are connected to square pyramids increasing the volume of the unit cell. Arrangement of Fe^{4+}/Fe^{3+} ions in the octahedral and square pyramidal complexes results in interesting properties that change even with a minute concentration of oxygen deficiency. Number of reports exist which describe this fascinating changes of phases and their effect on the transport and magnetic properties [1-7]. The charge ratio, Fe^{4+} to Fe^{3+} imparts a

profound influence on the magnetic structure and the related properties in $SrFeO_{3-\delta}$. Partial replacement of Fe with Ti not only stabilizes the crystal structure but also can alter the helical antiferromagnetic structure observed in the tetragonal system. It will be interesting to investigate the effect of site disorder caused by the random Ti doping and also the effect of fractional valence of Fe^{4+}/Fe^{3+} on the magnetic properties. Previous study by Alder et.al [8-9] reported large values of 5.7 μ_B and 5.9 μ_B for 10% and 30 % Ti doped cubic $SrFeO_{3-\delta}$. The high magnetic moment values are attributed to the formation of magnetic clusters with ferromagnetic interactions.

In this work, the results of systematic ac and dc magnetic measurements along with low- temperature neutron diffraction data clearly establish the magnetic ground state in T-$SrFe_{(1-x)}Ti_xO_{3-\delta}$ (x= 0,0.1,0.2 and 0.3).

4. 2 Thermomagnetic data

Figure 4.1(a) shows the zero-field-cooled (ZFC) and field-cooled (FC) dc magnetization (M) as a function of temperature (T) in the range 5-300 K for the undoped tetragonal $SrFeO_{2.86}$ measured at three different fields, namely 500 Oe, 1 kOe and 10 kOe. The most remarkable observation for the undoped sample at 500 Oe is the bifurcation in FC and ZFC M-T curves at T = 230 K which is the T_N of the orthorhombic phase. The FC

and ZFC curves are distinct till about 230 K and merge above this temperature; around 120 K (~ T_N of cubic phase) a change in curvature is observed. With lowering of temperature both ZFC and FC data of the undoped sample exhibit a transition at T ~ 79 K (which is the T_N of the tetragonal phase) followed by a sudden decrease in magnetization down to 69 K, which is typical of an antiferromagnet. Further lowering of temperature results in a more gradual decrease in M_{ZFC}. M_{FC} increases slightly from 69K to 5 K, but M_{ZFC} is almost constant up to 41 K and decreases with further lowering of temperature to 5 K. Even though the neutron diffraction data could be fitted only with tetragonal structure, the magnetization at low fields however reveals the presence of even trace cubic and orthorhombic phases.

Application of 1 kOe field shows similar features that are observed at 500 Oe field. M_{ZFC} reaches a maximum value at 79 K with a sharp drop in magnetization till T = 63 K. Beyond this magnetization decreases up to the lowest temperature of 5 K. However, M_{FC} continues to increase beyond 79 K and reaches a maximum at 73 K, which amounts to a shift of 6 K in comparison to the M_{ZFC}.

A field of 10 kOe suppresses the bifurcation in the ZFC-FC M(T) curves down to 81 K. However, the feature corresponding to the T_N of the cubic phase at 120 K is intact. At 81 K, similar to the M (T) at 500 Oe

and 1 kOe, there is a sharp decrease in M(T) up to 67 K with the transition temperature width of 15 K. The magnetization is almost constant from 67 K to 29 K in both ZFC and FC. Below 29 K there is a decrease in M_{ZFC} whereas M_{FC} increases. Magnetic field of 10 kOe is able to suppress the orthorhombic features in the magnetization data.

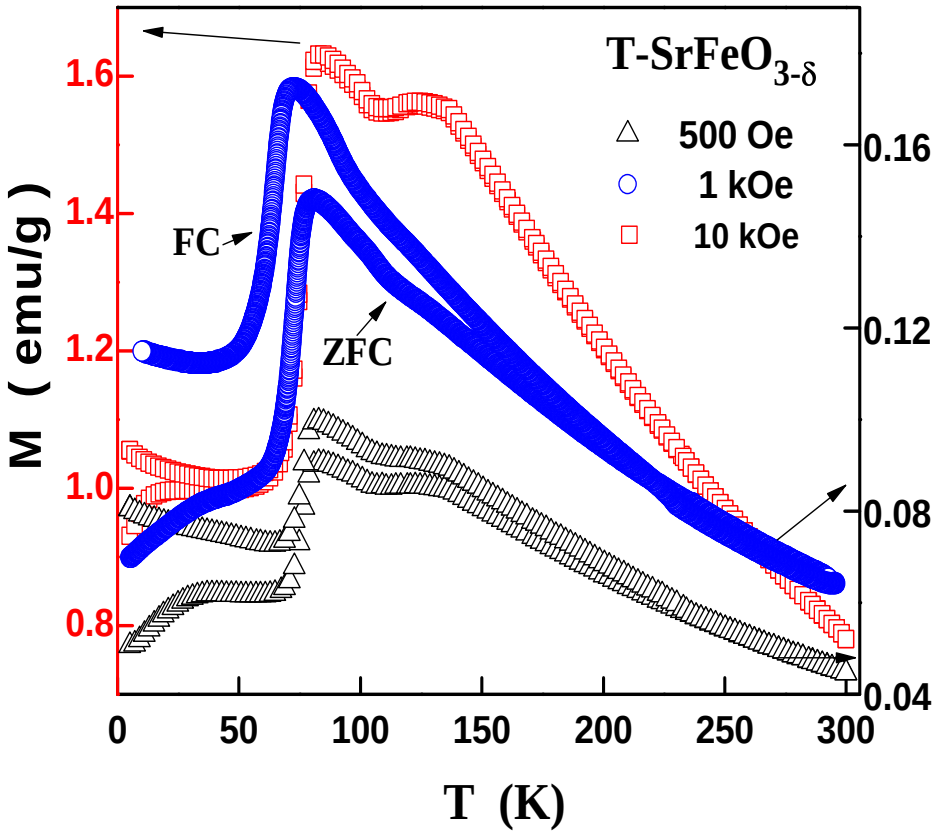

Figure 4.1 (a) M-T of T- $SrFeO_{3-\delta}$ for H = 500 Oe, 1 kOe and 10 kOe.

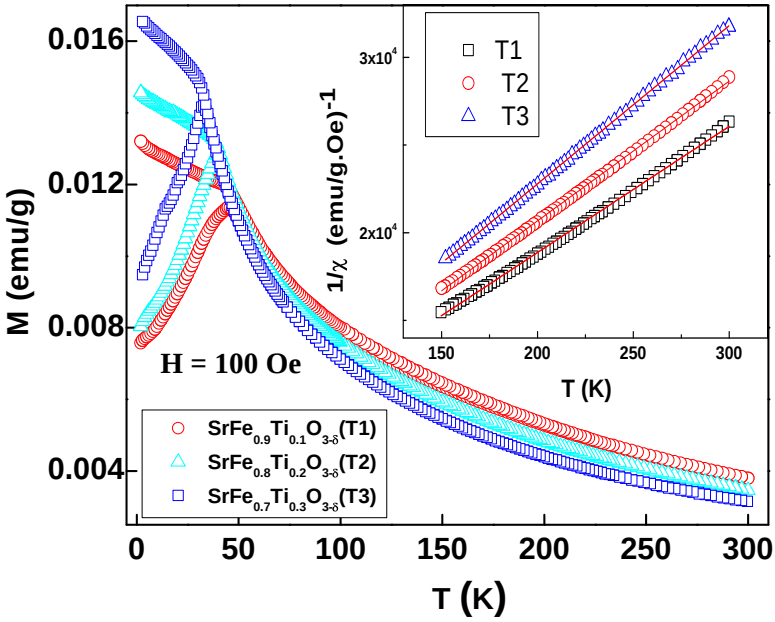

Figure 4.1(b) M-T of T-$SrFe_{1-x}Ti_xO_{3-\delta}$ (x = 0.1, 0.2 and 0.3), inset: χ^{-1} vs. T plots for T1- T3

Figure 4.1(b) shows the magnetization versus temperature of Ti doped $SrFeO_{3-\delta}$ systems namely T1, T2 and T3 at 100 Oe. In T1 (10 % Ti doped) from room temperature to 45 K, ZFC-FC M(T) curves overlap completely and the magnetization increases monotonously with a constant curvature. M reaches a maximum at $T^* \approx 45$ K in ZFC. Below 45 K, a decreases in M_{ZFC} and increase in M_{FC} is observed up to T= 2 K. The most important observation in comparison to the undoped sample is the absence of multiple phases at temperatures above T_N of the tetragonal phase. This confirms that Ti stabilizes the tetragonal phase of $SrFeO_{3-\delta}$.

In T2 system (20% Ti doped) the highest magnetization value is observed at $T^* \approx$ 38 K. From room temperature to 38 K both ZFC-FC magnetization curves coincide with each other, below which M_{ZFC} decreases. An upturn is noticed in M_{FC} below 38 K up to the lowest measured temperature of 2 K. M(T) of the sample T3 shows features similar to those in T1 and T2 except that M_{ZFC} reaches a maximum at $T^* \approx$ 32 K.

In all the Ti doped samples, the oxygen stoichiometry is the same. The high temperature anomalies that are seen in the undoped sample (arising due to the presence of small traces of cubic and orthorhombic phases) are not seen in the doped samples. This clearly establishes that Ti doping stabilizes the tetragonal phase in the present case. The $\chi(T) = M(T)/H$ data at temperatures above 230 K in the paramagnetic regime for the undoped sample and between 200 K and 300 K for the Ti doped samples, can be described by the Curie-Weiss law $\chi = C/(T- \theta)$. From the CW fit the effective moment, μ_{eff}, was calculated using the formula $\mu_{eff} = \sqrt{7.99C}$. The values calculated for the undoped sample are $\mu_{eff} = 5.3\ \mu_B$ and the paramagnetic Curie temperature θ = -3 K. For the Ti doped samples T1, T2 and T3, the effective moment decreases to 4.54 μ_B, 4.33 μ_B and 4.10 μ_B, respectively, and the corresponding θ values are 21.2 , 21.9 and 23.9 K.

The decrease in T^* (the temperature at which $M_{ZFC}(T)$ peaks) and the effective magnetic moment with the increase in Ti doping can be explained by the magnetic dilution caused by the partial substitution of magnetic Fe ion by the non-magnetic Ti ion.

The magnetic anomalies observed in the undoped sample are due to the presence of varying proportions of Fe^{4+}/Fe^{3+}. With Ti doping, the low-spin-state of Fe^{3+} seems to be increasing at the expense of high-spin state of Fe^{4+} thereby decreasing the total effective moment. In the above Ti doped systems, T3 shows the highest magnetization value of 0.0165 emu/g at 2 K compared to T2 (0.0145 emu/g) and T1 (0.0132 emu/g) in the FC mode. The increase in magnetization with increasing non-magnetic Ti concentration can be understood in terms of the decrease in the helical spin structure giving rise to a more collinear spins. This can also be seen in the M-H measurements described below.

4.3 M-H hysteresis loops

Magnetization has been measured up to 90 kOe at different temperatures 5, 50, 75, 100 and 150 K. Figure 4.2(a) shows the M-H hysteresis loops for the tetragonal $SrFeO_{3-\delta}$ (T0). Even up to 90 kOe, M increases linearly and a field of 90 kOe is not sufficient to saturate the magnetization. As expected in antiferromagnets, the M is higher close to

T_N than at low temperatures, i.e., M at 75 K is higher than that at 5 K and 50 K. For $T > T_N$, i.e., at 100 K, the magnetization decreases. M decreases further at 150 K. The coercivity (H_C) at 5 K is 1035 Oe and at 50 K it decreases to a low value of 84 Oe, the inset shows the enlarged view of the M-H loops that highlight large H_C in this sample.

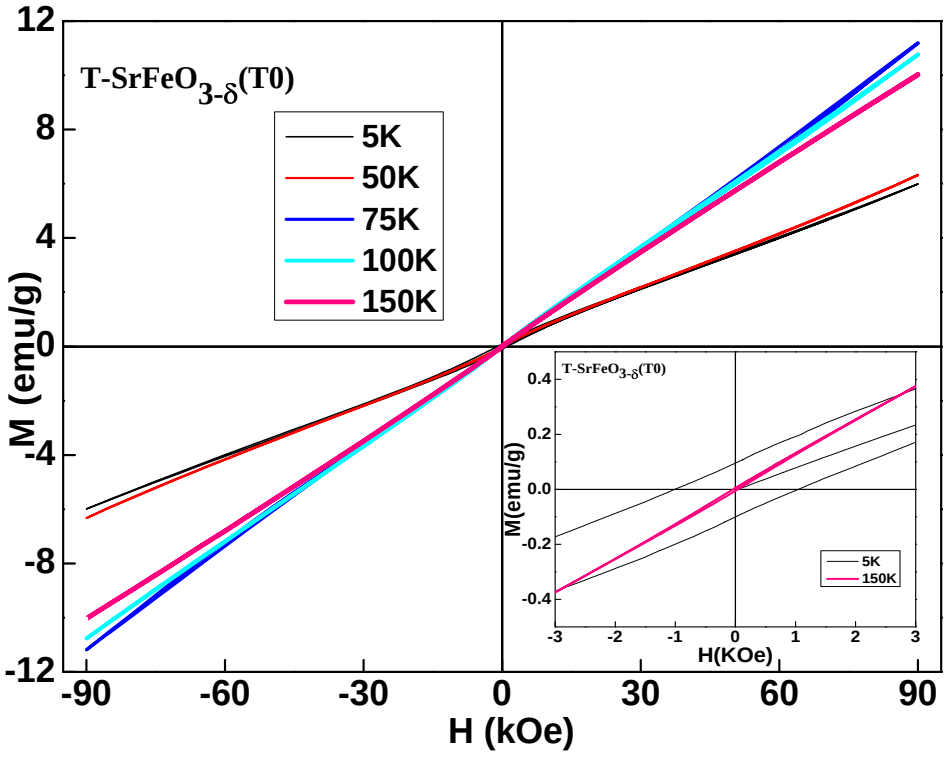

Figure 4.2(a) M-H of T0 at different Temperatures and the inset show magnified data of 5 and 150 K.

At other temperatures of 75 K, 100 K and 150 K, H_C remains constant with a value of around 40 Oe. The remanence is 0.09586 emu/g at 5 K and value decreases by one order of magnitude as the temperature reaches 150 K.

Figure 4.2(b) shows the M-H loop of T1 at 5 K and 55 K (below and above $T^* \approx$ 45 K) measured up to 9T field. The coercivity (remanence) decreases from 1352 Oe (0.1097 emu/g) at 5 K to 10 Oe (0.00048 emu/g) at 55 K.

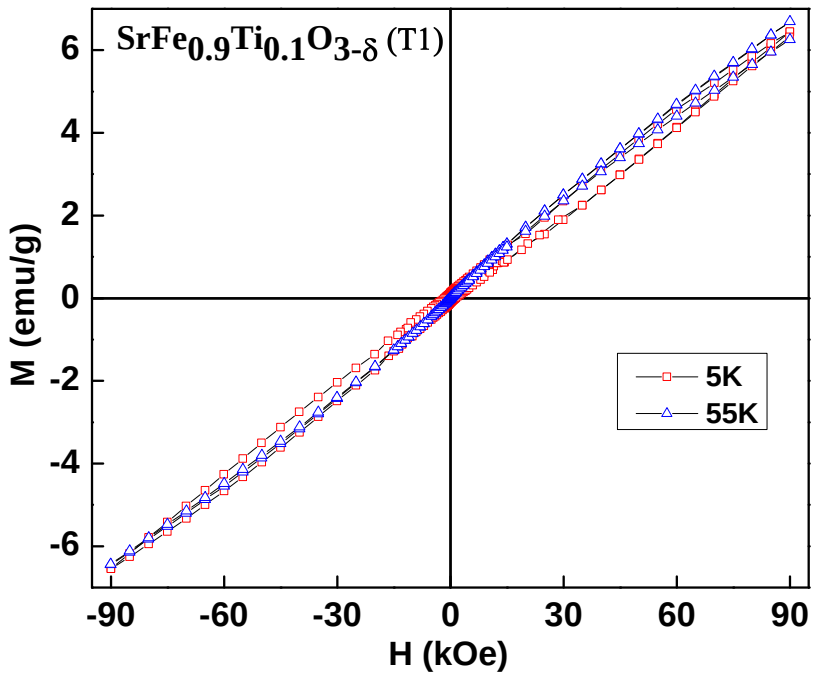

Figure. 4.2(b) M-H hysteresis loops for $SrFe_{0.9}Ti_{0.1}O_{3-\delta}$ at T = 5 and 55 K.

Figure 4.2(c) shows the M-H loops of T2 at 5 and 55 K. The coercivity at 5 K is 1390 Oe and it reduces to a low value of 6 Oe at 55 K. Figure 4.2(d) shows the M-H loop of T3 at 5K. The magnetization (8.3807 emu/g), coercivity (2011 Oe) and remanence (0.2233 emu/g) of T3 at 5 K is the highest among all the samples studied. When compared to T0, T1 and T2, the bending of the magnetization curve in T3 at H $\approx$ 40 kOe so as to saturate at fields > 9 T is evident from figure 4.2. The increase in magnetization and coercive fields as well as the tendency towards saturation observed in M-H loops with increase in Ti doping clearly indicates that the ferromagnetic interactions grow in strength at the expense of the antiferromagnetic interaction between Fe^{4+}/Fe^{3+} ion spins mediated through O^{2-}.

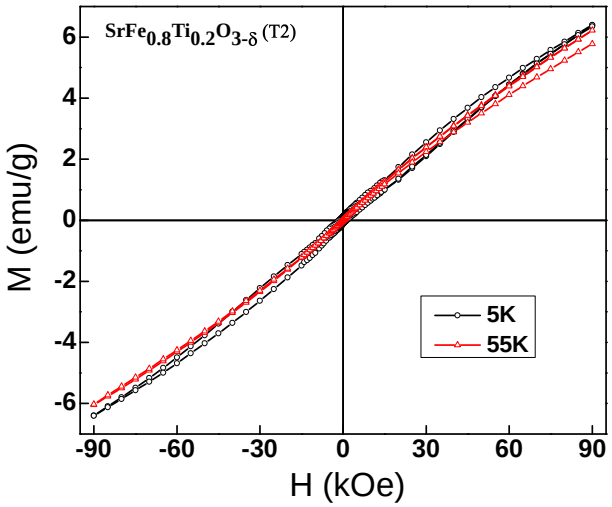

Figure 4.2 (c) M-H hysteresis loops for $SrFe_{0.8}Ti_{0.2}O_{3-\delta}$ at T = 5 and 55 K.

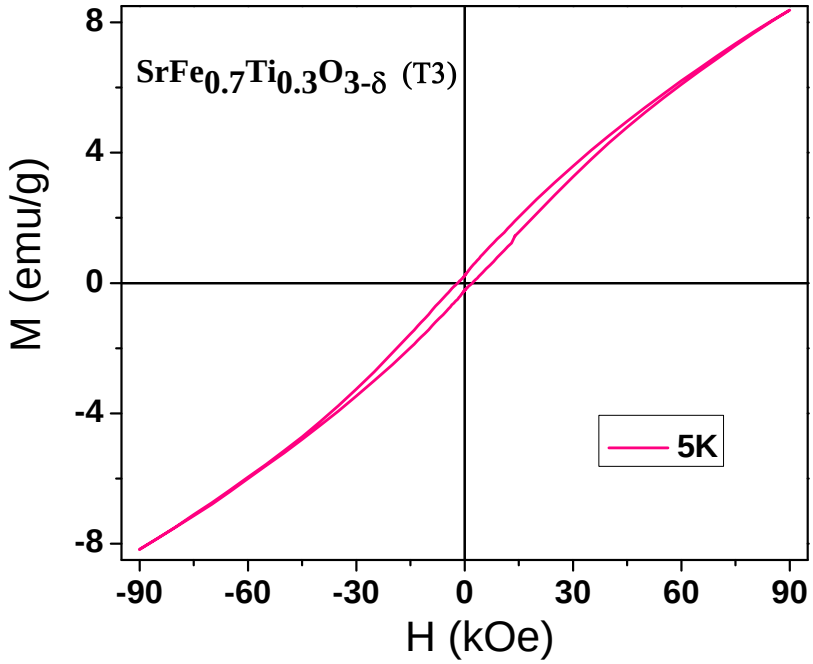

Figure 4.2 (d) M-H hysteresis loop for $SrFe_{0.7}Ti_{0.3}O_{3-\delta}$ at T = 5 K.

4.4 Exchange Bias

In $SrFeO_{3-\delta}$, Fe exists in mixed valence states of Fe^{3+} and Fe^{4+}. The antiferromagnetic superexchange interactions between Fe^{4+}-O^{2-}-Fe^{4+} spins and the ferromagnetic double exchange interactions between Fe^{4+}-O - Fe^{3+} spins can give rise to a phenomenon called exchange bias (EB). The exchange bias, initially observed in Co/CoO [10] and in many other core shell nanoparticles [11-16], is characterized by a shift in M-H loop when measured by cooling the sample through T_N from a temperature above T_N in the presence of a bias field. To investigate if exchange bias is present in the current system and also to determine the effect of Ti doping on the exchange bias, a series of M-H hysteresis loops were carried out by cooling the sample from room temperature to the measurement temperature below T_N in the presence of 90 kOe bias field.

Figure 4.3(a) shows M-H hysteresis loop of T0 system with a field of 90 kOe applied at room temperature and cooled to the lowest temperature of 5 K where M-H hysteresis loop was recorded. Once the tracing of M-H loop is finished, the field is brought down to zero with the oscillatory mode to avoid the presence of any stray fields. Again the system is warmed up to room temperature then 90 kOe field is applied and cooled to 55 K where M-H loop is recorded. Figures 4.3(b)–4.3(d) show the M-H loops of T1-T3 measured by cooling the samples up to 5

K in 90 kOe field. The exchange field is calculated from the observed shift in M-H loop for all the samples and is tabulated in Table 4.1. With increase in Ti^{4+}, the ratio of Fe^{4+} to Fe^{3+} varies which changes the proportions of competing ferromagnetic and antiferromagnetic interactions. Thus, Ti doping is expected to affect the EB present in the system. From the table (4.1) it is evident that initially with increase in Ti^{4+} doping there is a sharp increase in EB. From our room temperature neutron measurements (discussed in chapter 3) we find that for the doping of 10% Ti, Ti prefers to occupy only the Fe1 and Fe3 sites which are Fe^{4+} valence states. This site preference is expected to drastically change the Fe^{4+}/Fe^{3+} ratio giving rise to a large change in EB.

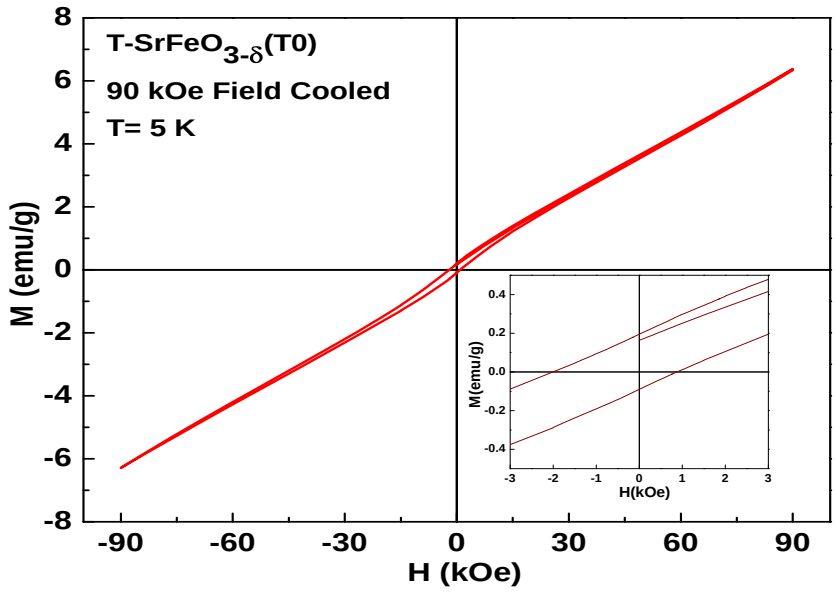

Figure 4.3(a) M-H loop of T0 at 5 K after cooling from RT in a field of 90 kOe and the inset shows magnified data of T0.

With further increase in Ti doping, Ti not only replaces Fe^{4+} but also $Fe^{3+\delta}$ affecting the Fe^{4+}/Fe^{3+} ratio and resulting in a decrease of EB for 30 at.% Ti doping.

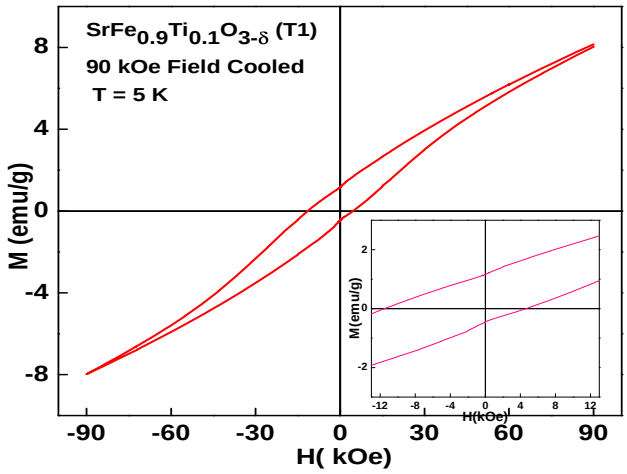

Figure 4.3(b) M-H loop of T1 at 5 K after cooling from RT in a field of 90 kOe and the inset shows the enlarged view.

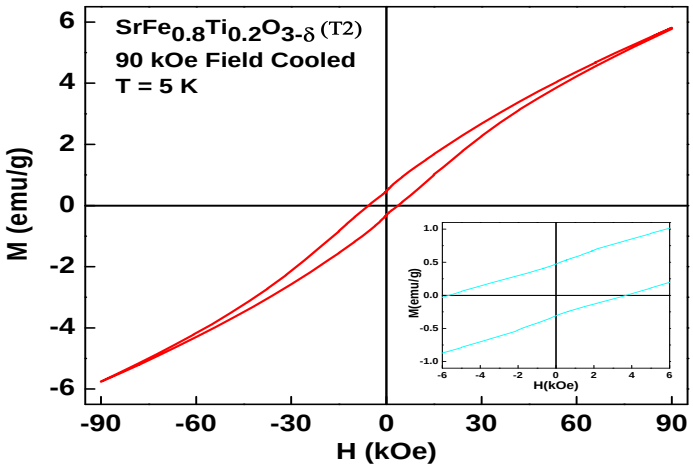

Figure 4.3(c) M-H loop of T2 at 5 K after cooling from RT in a field of 90 kOe.

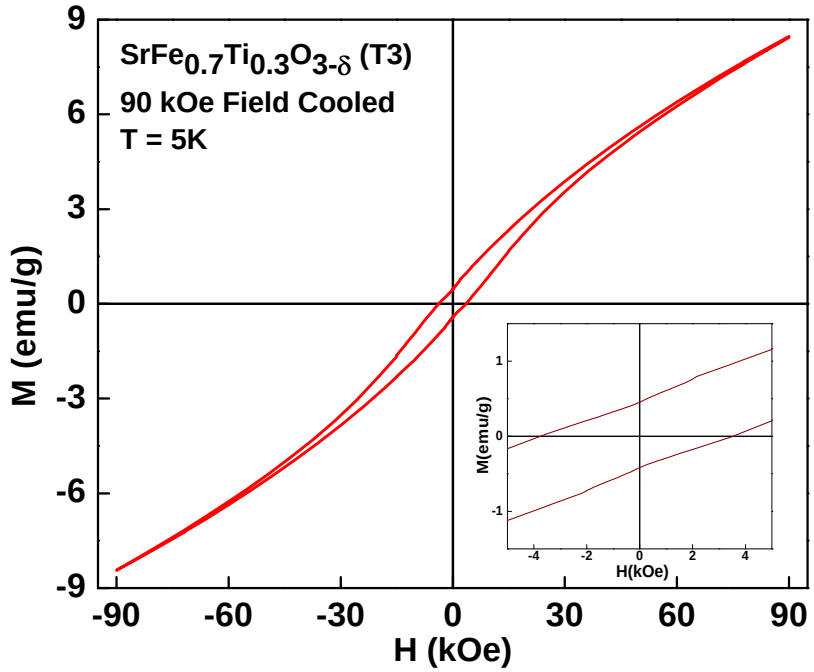

Figure 4.3(d) M-H loop of T-$SrFe_{0.7}Ti_{0.3}O_{3-\delta}$ at 5 K after cooling from RT in a field of 90 kOe

Table 4.1: Exchange bias field and coercivity at T = 5 K

Sample	EB (Oe)	H_C (Oe)
T0	560	1440
T1	3400	8000
T2	4600	950
T3	50	3600

4.5 Arrott plots

In general, the presence of random site disorder and competing ferromagnetic and antiferromagnetic interactions gives rise to a frustrated spin system called a spin glass. With increase in Ti doping M-H loops showed a tendency to eventually saturate at fields > 90 kOe. This observation that the helical spin structure prevalent in T0 paves way to a ferromagnetic arrangement of spins progressively so that in the sample T3, the ferromagnetic spin component dominates over the antiferromagnetic spin component. Considering that the long-range ferromagnetic order is characterized by a finite spontaneous magnetization for temperature below the Curie temperature, whether or not the M-H hysteresis loop of sample T3 is symptomatic of the FM ground state can be ascertained from the Arrott plots, as elucidated below.

Spontaneous magnetization (M_S) is the order parameter for the FM-PM transition. Theoretically, M_S is the value of magnetization within the domains in the absence of the external magnetic field. Experimentally, however, the magnetization in the limit of $H_{app} \rightarrow 0$ yields the spontaneous magnetization. Spontaneous magnetization can be determined by measuring the magnetization as a function of field

(below phase transition temperature) and extrapolating the high-field magnetization to H = 0.

Specifically for second-order phase transition,

$H_{int} = (1/\chi_0) M + \beta M^3$

where the internal field H_{int} is the external field corrected for the demagnetizing field, χ_0 is the initial susceptibility and M is the magnetic moment per unit volume. At the Curie temperature, $1/\chi_0 = 0$. For finite fields and temperatures, the above magnetic equation of state takes the form

$(H_{int}/M) = (1/\chi_0) + \beta M^2$

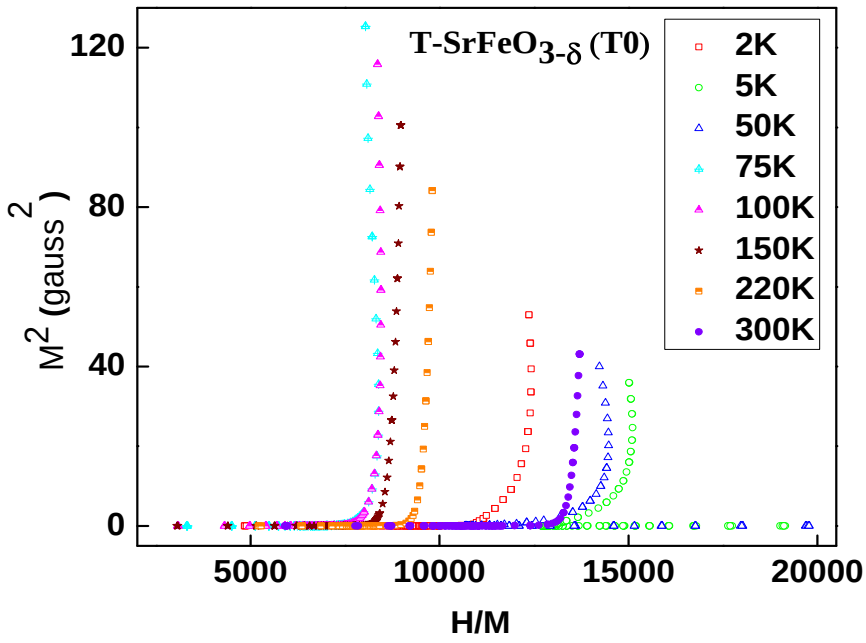

Figure 4.4(a) Arrott plot for T0 at different temperatures showing that $M_S = 0$ at all temperatures.

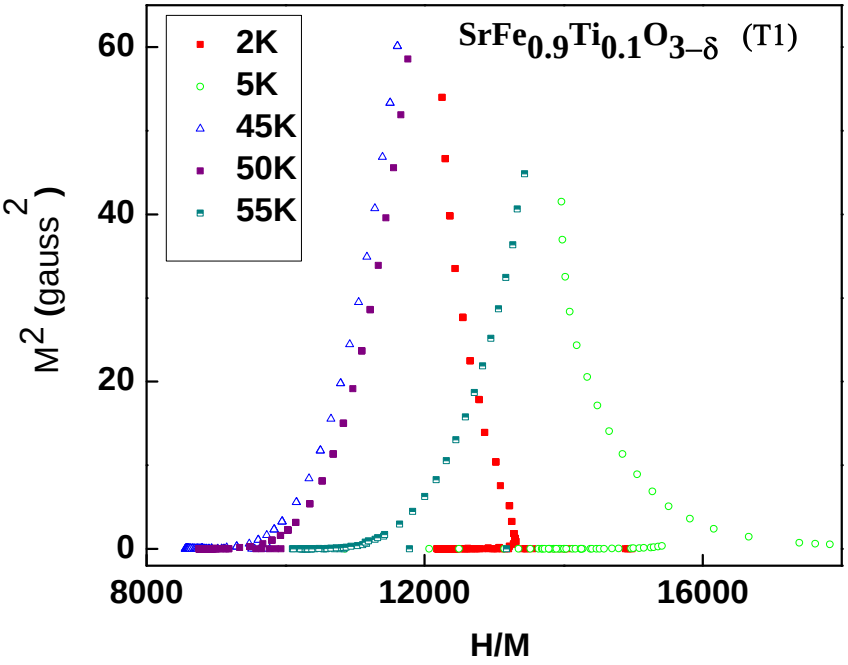

Figure 4.4(b) Arrott plot for T1 different temperatures showing that $M_S = 0$ at all temperatures.

Thus, the spontaneous magnetization and inverse initial susceptibility are obtained as intercepts on the ordinate and abscissa for temperatures $T < T_C$ and $T > T_C$ when the linear high-field portions of the Arrott plot (M^2 vs. H/M) isotherms are extrapolated to H = 0 and M = 0, respectively. The Arrott plot isotherm that goes through the origin corresponds to the Curie temperature, T_C. Arrott plots are constructed

after correcting for the demagnetization factor for all the samples at temperatures down to 2 K are shown in figures 4.4(a) - 4.4 (d). Since none of the Arrott plot isotherms yields a finite intercept on the M^2 axis when extrapolated to H = 0, no spontaneous magnetization exists at any temperature for all the samples studied. This result completely rules out the possibility of a FM ground state in any of the samples [17, 18].

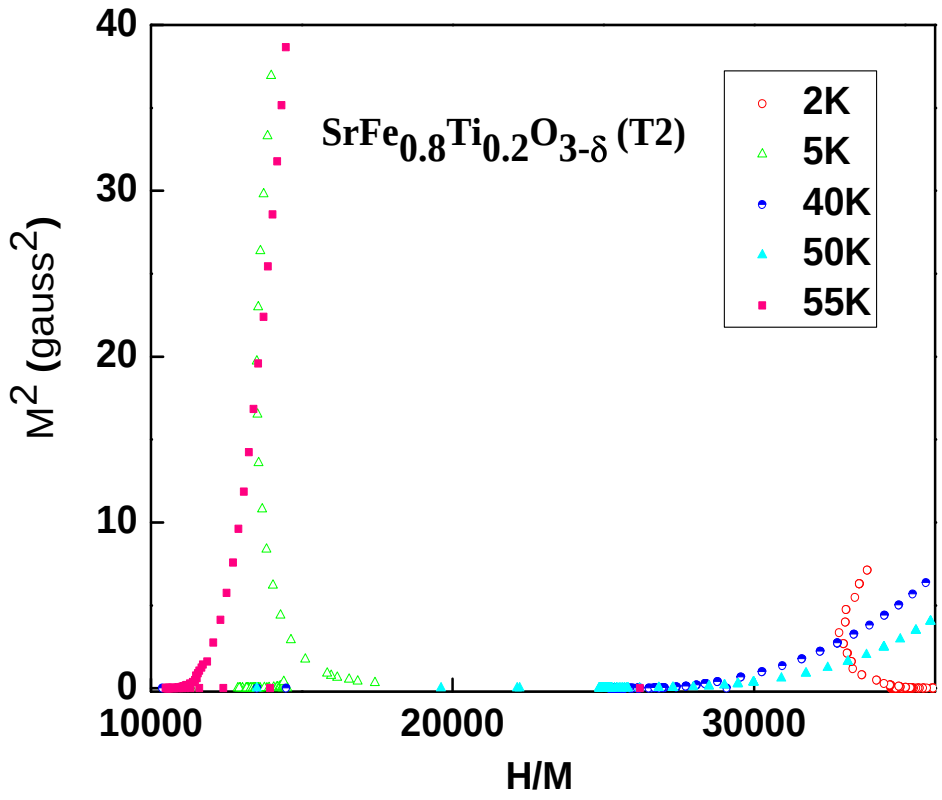

Figure 4.4(c) Arrott plot for T2 at 5 K different temperatures showing that $M_S = 0$ at all temperatures.

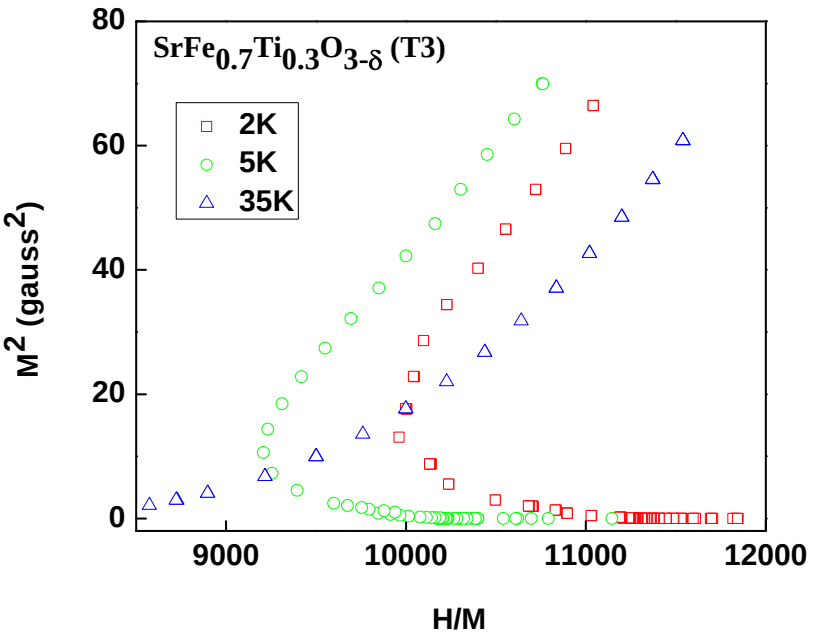

Figure 4.4(d) Arrott plot for T3 at different temperatures showing that $M_S = 0$ at all temperatures.

4.6 AC magnetic susceptibility

AC susceptibility (being a zero field measurement) is a powerful technique to study magnetic phase transitions, which can be smeared out by the presence of even moderate magnetic fields. The frequency dependence of ac susceptibility is useful to distinguish various types of magnetic order present in a system. To ascertain the magnetic order in

these systems, systematic ac susceptibility measurements were carried out.

Figure 4.5(a)-(d), shows AC magnetic susceptibility (χ') as a function of temperature for undoped (T0) and doped (T1, T2 and T3) samples at different frequencies in the frequency range from 11 Hz to 9999 Hz measured at an ac amplitude of 8 Oe without superposed dc field. With lowering of temperature, the undoped T0 exhibits a transition at around 82 K followed by a steep decrease in the χ' down to 61 K. When the temperature is lowered further, more gradual decrease in χ' is observed. Susceptibility curves at different frequencies do not exhibit any frequency shift and lie on top of each other up to 61 K. In addition to the transition at $T \approx 82$ K, another transition is manifested as a cusp at $T \approx 124$ K. These two transitions can be identified as the T_N for tetragonal (Fe^{3+} state) and a residual cubic (Fe^{4+} state) phase, respectively. The sensitivity of the ac susceptibility technique is revealed by the observation of the cubic phase, which is not evident in the dc magnetization measured at fields as low as 100 Oe.

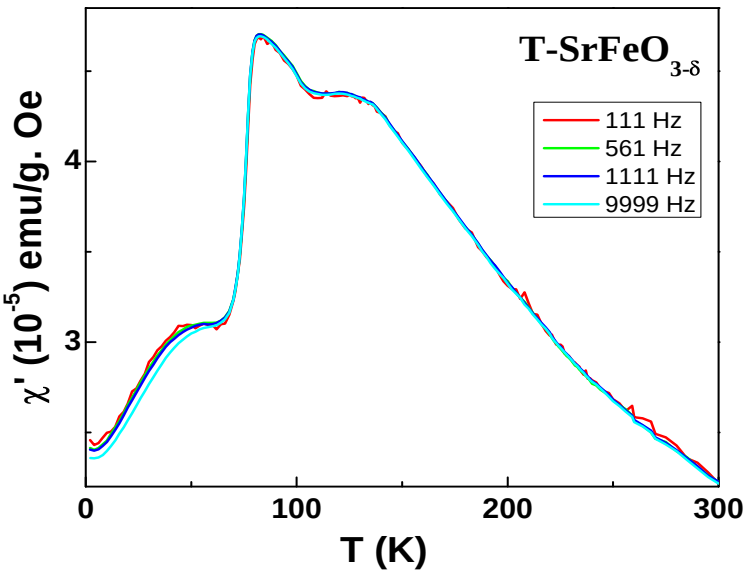

Figure 4.5(a) AC susceptibility of T-$SrFeO_{3-\delta}$ measured at different frequencies.

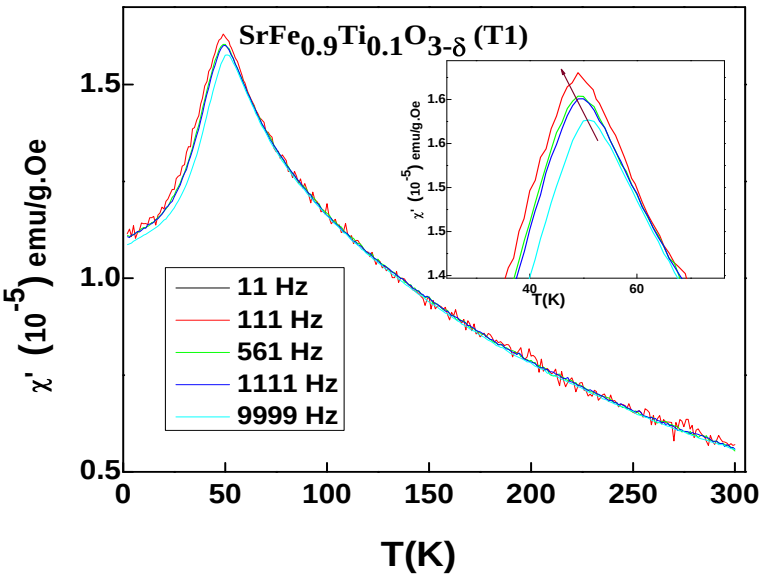

Figure 4.5(b) AC susceptibility of T-$SrFe_{0.9}Ti_{0.1}O_{3-\delta}$ measured at different frequencies.

χ' vs. T for T1 is shown in figure 4.5(b). Only a single maximum is noticed at T_{max} = 48 K for 11 Hz. T_{max} shifts to higher temperatures with the increase in frequency and reaches a value of 50 K for 9999 Hz. There is no indication of the cubic phase in the Ti doped samples indicating the stabilization of the tetragonal phase. The dispersion in susceptibility increases with lowering of temperature below T_{max}. Figures 4.5 (c) and 4.5(d) depict the susceptibility for the T2 and T3 samples.

For sample T2, T_{max} remains close to that in T1 whereas it shifts to a lower temperature of 34 K for T3. The peak in χ' matches well with the observed peak temperature in dc magnetization measurement at H = 100 Oe.

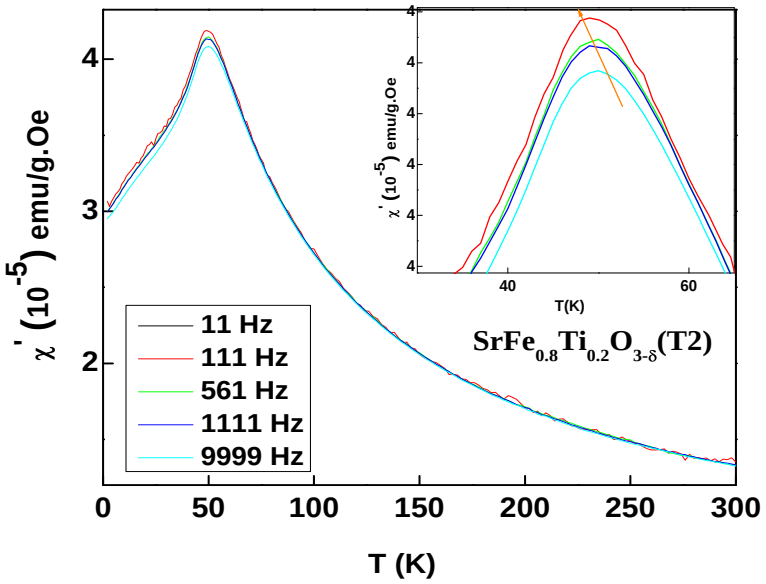

Figure 4.5(c) AC susceptibility of T-$SrFe_{0.8}Ti_{0.2}O_{3-\delta}$ measured at different frequencies.

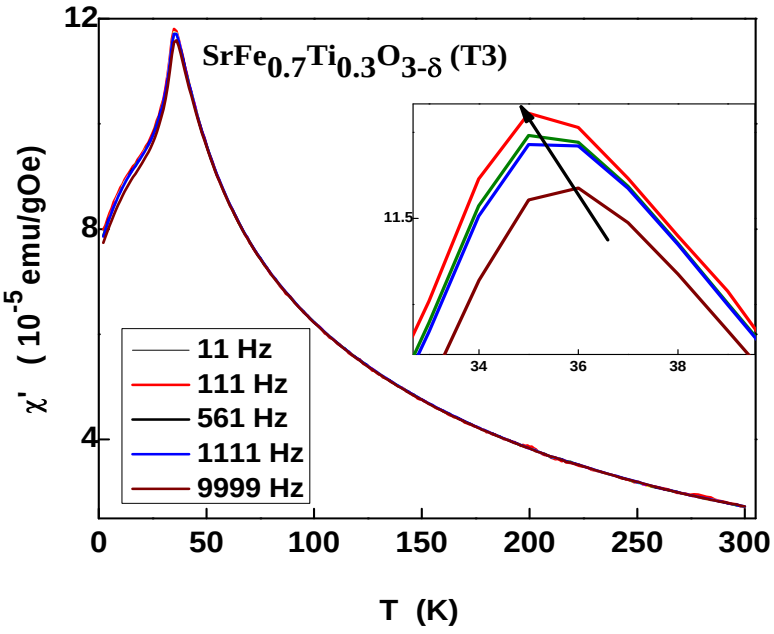

Figure 4.5(d) AC susceptibility of T-$SrFe_{0.7}Ti_{0.3}O_{3-\delta}$ measured at different frequencies.

Figure 4.6 shows a combined plot of χ' vs. T for all the four samples under investigation. It can be seen clearly that with 10% Ti doping, the magnitude of χ' decreases in comparison to the sample T0 but with increase in Ti doping, there is a large increase in χ'. This is in accordance with the dc magnetization data indicating that the helical magnetic structure observed in undoped sample is weakening with the increase in Ti doping, leading to a less non-collinear magnetic state [19]. The inset shows the dispersion in susceptibility measured at two different frequencies for T1 sample. This type of frequency dependence of ac susceptibility is observed in many spin- frustrated systems such as spin glasses [20-22].

The magnetization reversal between two metastable states, arising from the spin frustration caused by the mixed valency in this system, is separated by an anisotropy barrier (E_a). In terms of the attempt frequency, this can be expressed as the Néel-Arrhenius (N-A) law i.e., $\ln f = \ln f_0 - (E_a/k_B T)$. When the frequency dependence of T_P (the temperature at which the ac susceptibility peaks) is analyzed using the N-A law (as shown in Fig. 7(a)), the results gave unphysically large values E_a/k_B= 4681 K and $f_0 = 8.6 \times 10^{43}$ Hz.

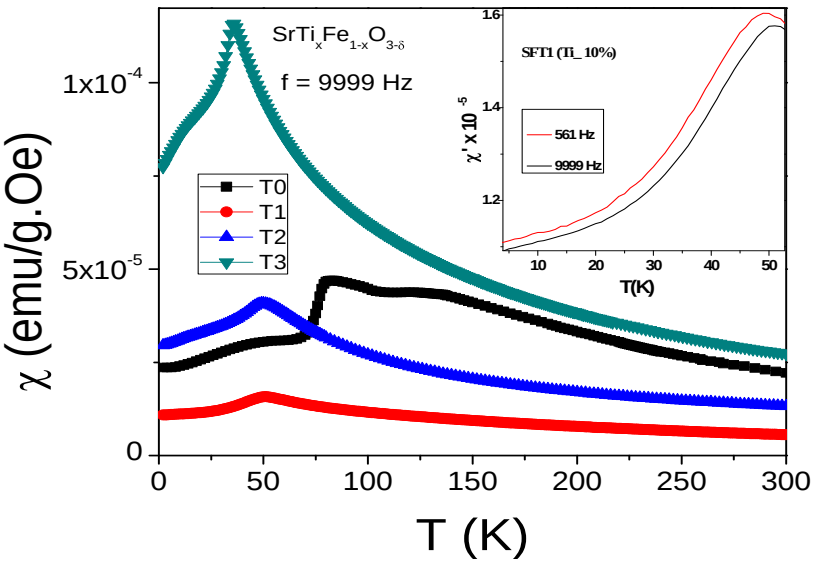

Figure 4.6 Comparison of AC susceptibility of the samples T0, T1, T2 and T3.

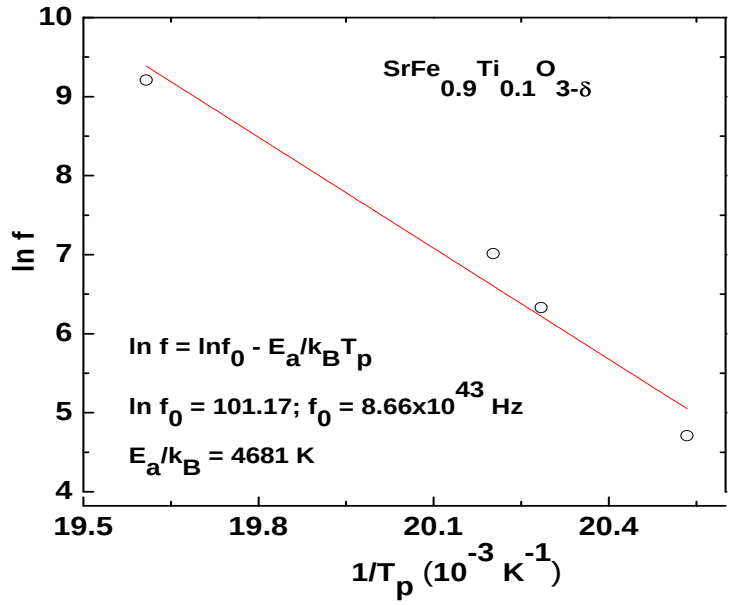

Figure 4.7(a) N-A analysis of the frequency dependence of T_p for T1.

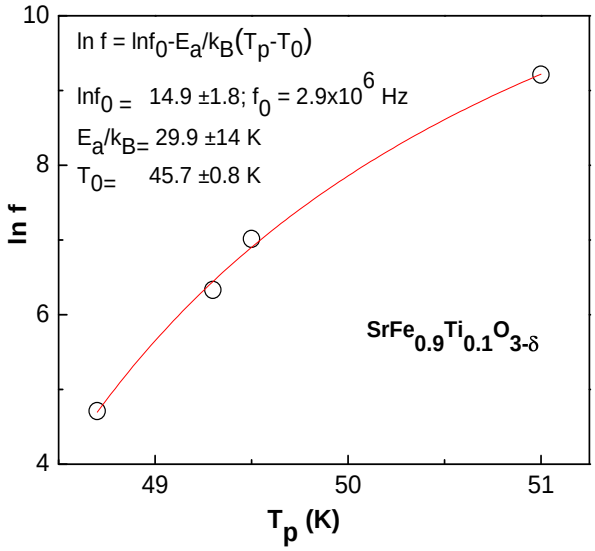

Figure (7b) V-F analysis of the frequency dependence of T_p for T1.

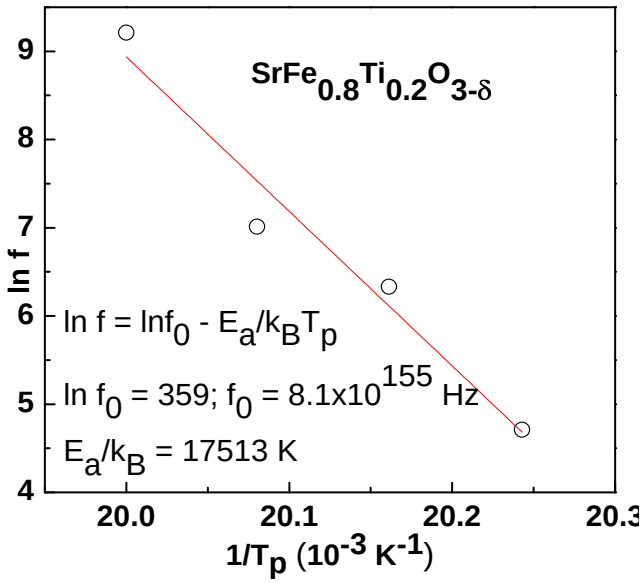

Figure 4.7 (c) N-A analysis of the frequency dependence of T_P for T2

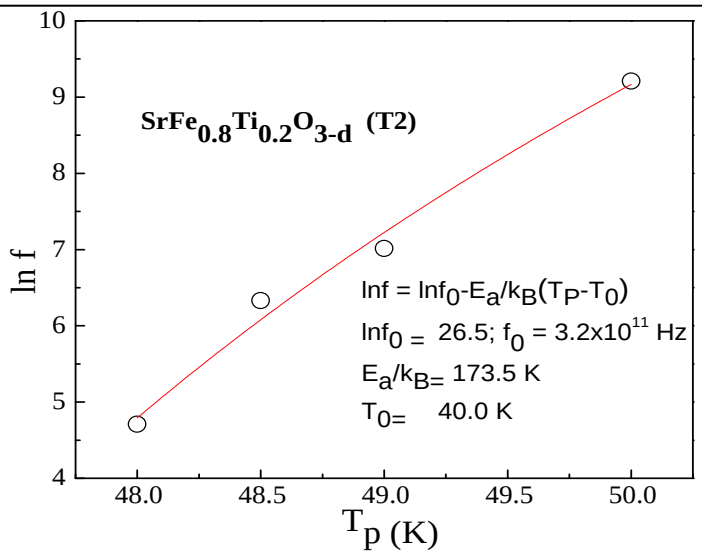

Figure 4.7 (d) V-F analysis of the frequency dependence of T_p for T2.

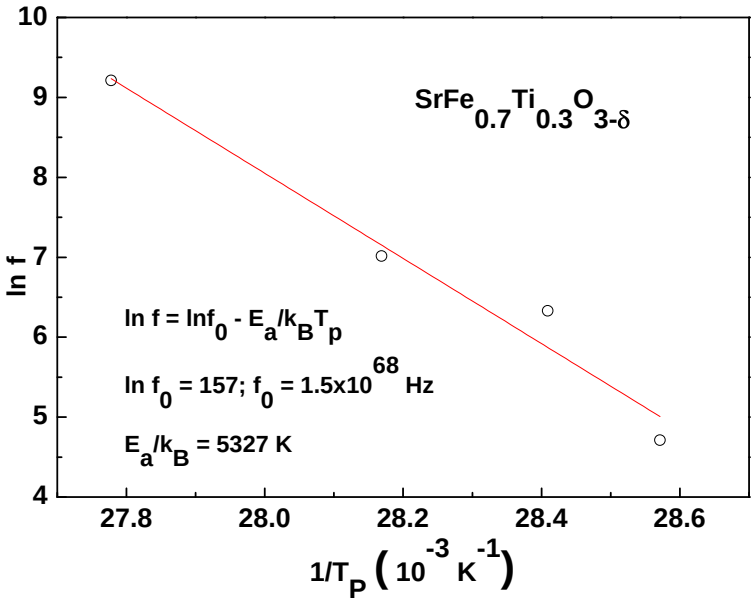

Figure 4.7 (e) N-A analysis of the frequency dependence of T_p for T3.

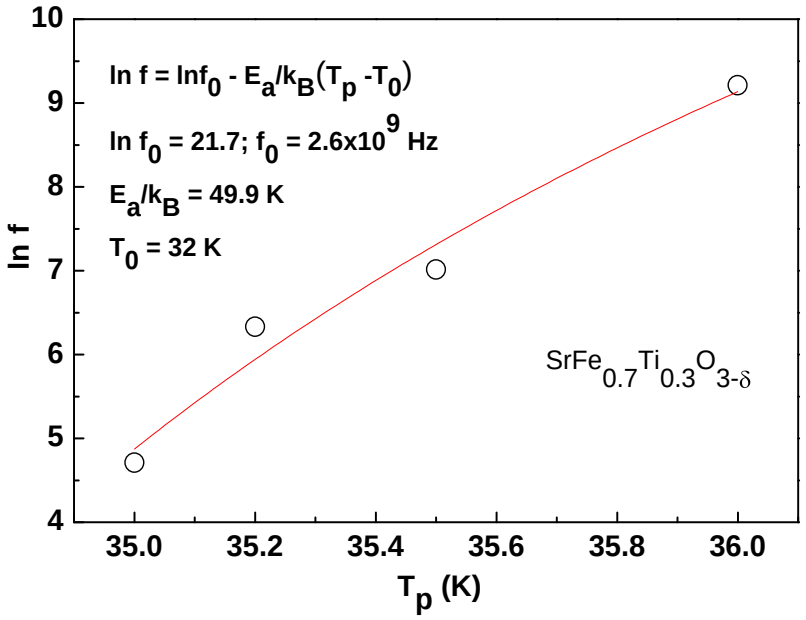

Figure 4.7 (f) Vogel-Fulcher analysis of the frequency dependence of T_P for T3.

This shows that the interactions between the spin clusters play a significant role and the activation energy and the relaxation times are controlled by the strength of such interactions. To further analyze the role of cluster spin glass interactions, the frequency dependence of T_P is analyzed in terms of Vogel-Fulcher (V-F) law: $\ln f = \ln f_0 - E_a/k_B(T_P - T_0)$.

It can be seen clearly (Fig. 4.7(b)) that V-F describes the data much better than N-A. The analysis yields $f_0 = 2.9 \times 10^6$ Hz and $E_a/k_B = 29.9$

K, which are very reasonable, as is T_0= 45.7 K, where T_0 is a measure of the interparticle interaction. From these analyses, we conclude that with the decrease in temperature, the interacting spin clusters freeze in random orientations giving rise to the frequency-dependent ac susceptibility. Similar analysis in terms of N-A and V-F laws are performed for the 20% and 30% Ti doped samples with the results shown in fig 4.7(c)-4.7(f). For all the samples, V-F law describes the frequency dependence of ac susceptibility much better indicating that the Ti doped samples behave as cluster spin glasses [23].

4.7 Neutron diffraction

Neutron diffraction (ND) is the only experimental tool that can establish the existence of long-range antiferromagnetic order (if present) without any ambiguity. No spontaneous magnetization at any temperature, as inferred from the Arrott plots, can be due to the presence of either a long-range antiferromagnetic order or a spin glass order. Neutron diffraction pattern should exhibit additional diffraction peaks (purely magnetic in nature) at low transfer momentum, $\boldsymbol{q}$, (or equivalently, at small Bragg angles) below T_N, due to the doubling of the unit cell if long-range AF order is present. On the other hand, long-range FM order leads to an enhancement in the intensity of the nuclear Bragg peaks, as the ferromagnetic unit cell is the same as the crystallographic unit cell.

In this case, no peaks other than the nuclear Bragg peaks should be observed, which implies that no additional magnetic peaks should appear at low ***q***.

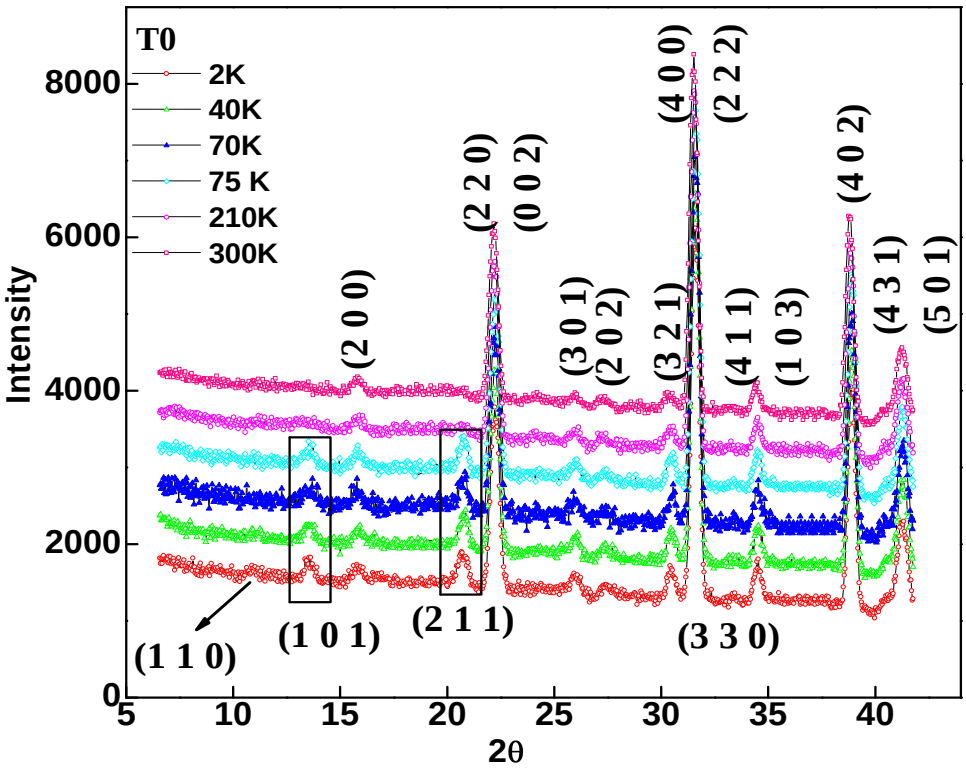

Figure 4.8 (a) Neutron diffraction patterns of T0 measured at different temperatures, emergence of new (101) and (211) peaks (rectangular boxes) are observed below T_N.

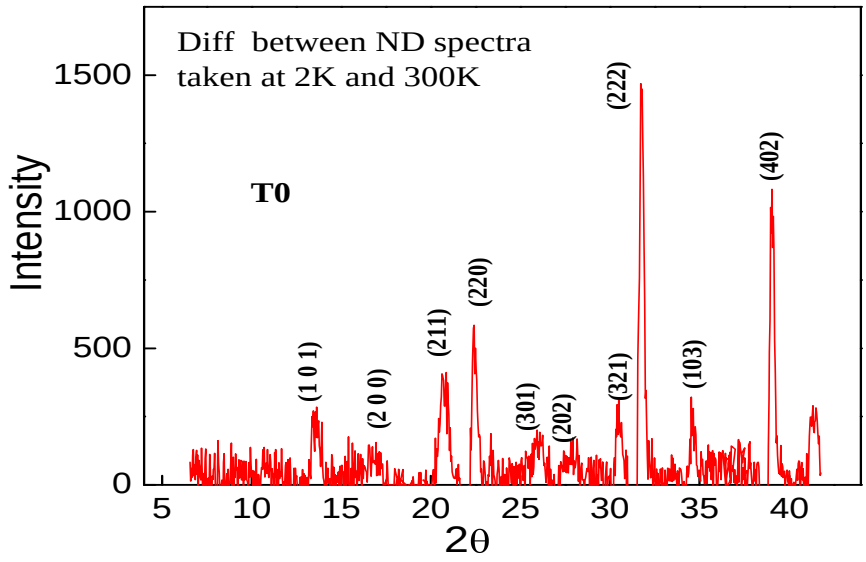

Figure 4.8 (b) Difference in the intensity of ND spectra taken at 2 K and 300 K for the T0 sample indicates the presence of extra peaks resulting from the AFM structure.

Neutron diffraction measurements were carried out on T0 at 2 K, 40 K, 70 K, 75 K, 210 K and 300 K (Fig. 8(a). Intensity of (110) reflection is increased at 2 K in comparison to that at 40 K. An additional peak (in comparison to the room temperature data), identified as the (101) reflection, is observed from 75 K till the lowest temperature of 2 K. This reflection arises from the antiferromagnetic ordering in this system. The intensity of this peak is almost constant from 75 K to 2 K. The (200) reflection intensity is found to increase while cooling from room temperature (RT). The (211) reflection has both nuclear and magnetic

contribution because a small peak arising due to nuclear scattering is present even at RT but with decrease in temperature an increase in intensity is observed due to the magnetic contribution. The difference in intensity between the data taken at 2 K and 300 K is shown in Fig 4.8(b).

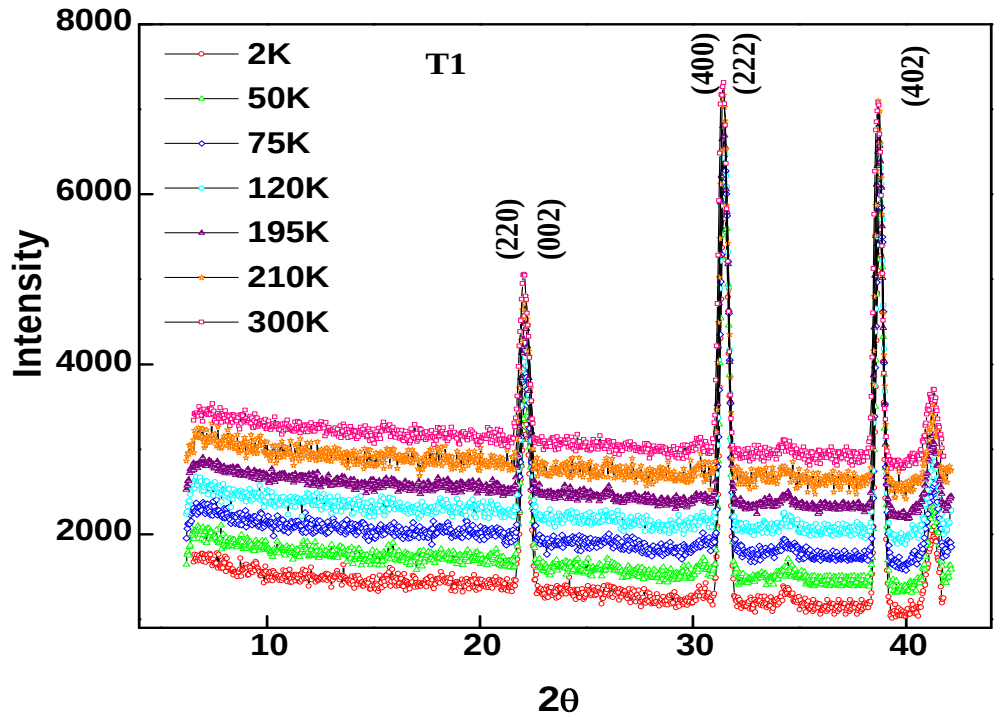

Figure 4.9 (a) Neutron diffraction patterns of T1 measured at different temperatures.

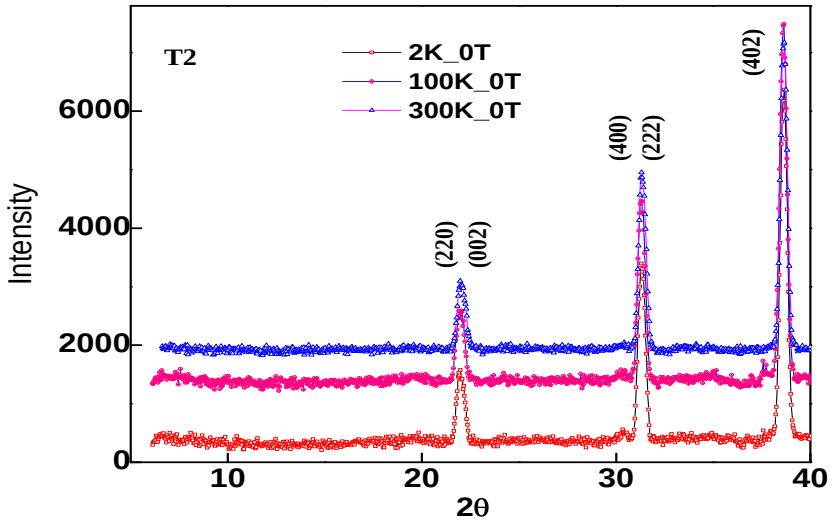

Figure 4.10 (a) Neutron diffraction pattern of T2 measured at different temperatures. No new peaks are observed even at T = 2 K.

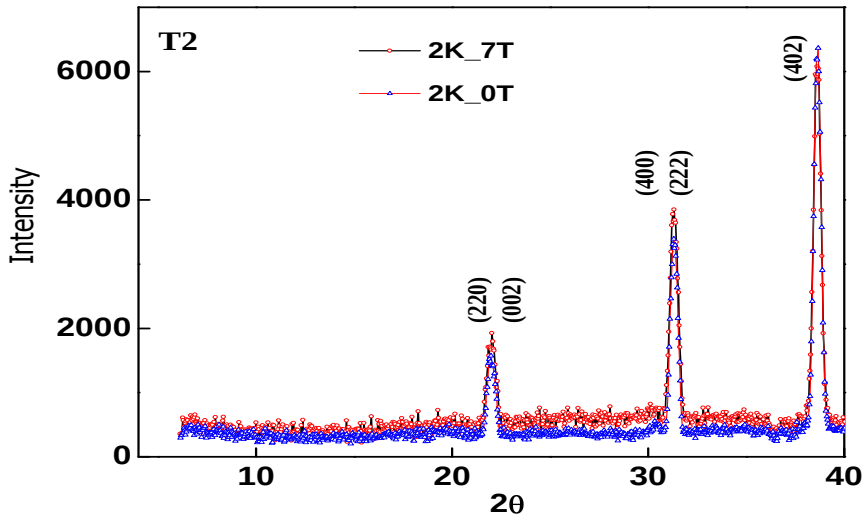

Figure 4.10 (b)Comparison of neutron diffraction pattern measured at 2 K in zero and 70 kOe field.

The low temperature ND data for T0 system provides an evidence for a ferromagnetic component (increase in the intensities of the diffraction peaks such as (200) and (211)) and an antiferromagnetic component (presence of new peaks such as (101) below T_N).

In order to observe the magnetic ordering, low temperature neutron diffraction measurements are carried out on all the Ti doped samples (T1, T2 and T3). Fig (4.9), 4.10(a) and 4.11(a) show the comparison of neutron data at 2 K and 300 K. At 2 K, there is neither any additional peak nor an increase in the intensity of the diffraction peaks in comparison to the 300 K data. Fig 4.10(b), Fig 4.11(b) show the comparison of the neutron diffraction data measured at zero field and in a field of 70 kOe. If long-range FM order is present, there will be an increase in intensity of the diffraction peaks. On the other hand, if a long range AFM order is present, the intensity of the diffraction peaks will be suppressed. There is neither an increase nor a decrease in the intensity because of the application of 70 kOe field, indicating that the Ti doped T-$SrFeO_{3-\delta}$ behaves as a cluster spin glass.

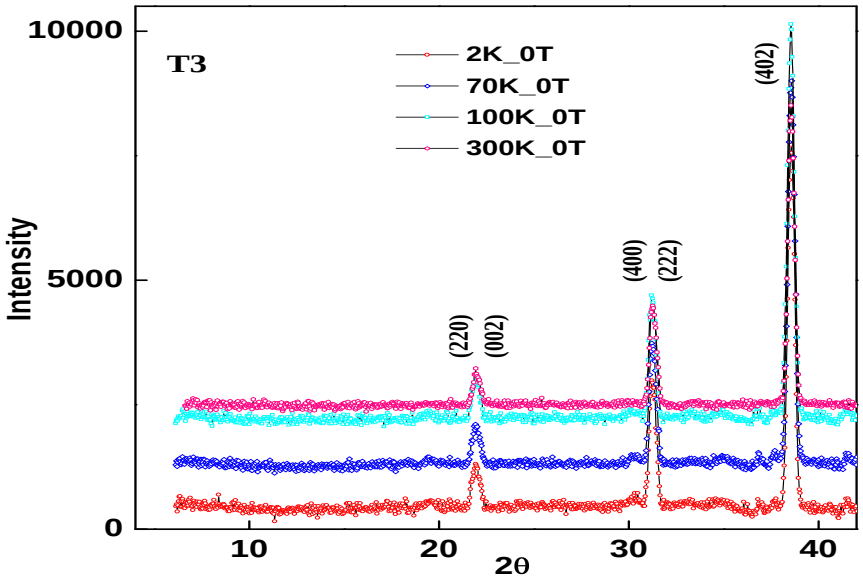

Fig 4.11(a) Neutron diffraction patterns of T3 measured at different temperatures. No new peaks are observed even at T = 2 K.

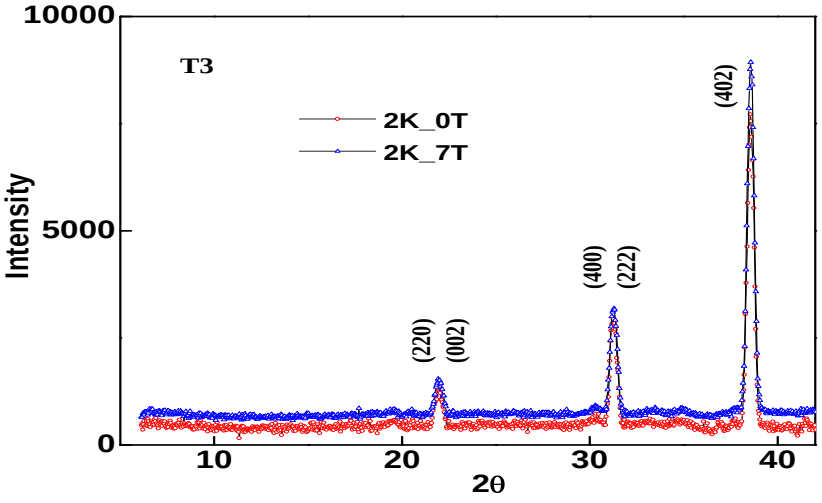

Figure 4.11(b) Comparison of neutron diffraction patterns measured at 2 K in zero field and in H= 70 kOe.

4.8 Discussion

We can now put all these results in perspective and try to develop an understanding of magnetism in these materials. The dc magnetization measured for all the samples shows strong magnetic history effects, which are observed as a bifurcation in the zero-field-cooled (ZFC) and Field-cooled (FC) magnetization curves. Irreversibility in magnetization refers to the difference in ZFC and FC magnetizations (ΔM). Generally irreversibility is an indication of the magnetic metastable states. Irreversibility is observed in a wide variety of magnetic materials, for example in spin glasses, cluster glasses, superparamagnets, etc. But the origin of irreversibility is not the same in all the above cases. Generally, the presence of random local anisotropy field causes the irreversibility. Bifurcation occurs in the ZFC-FC magnetizations when the applied field is less than the local field. When the sample is cooled in zero-field through the transition, certain number of spins is locked in a particular direction dictated by the local field direction. While measuring magnetization in the ZFC mode, the applied field is sufficiently lower than the local anisotropy field, and then the number of spins contributing to the magnetization is less than the actual number of spins which gives rise to lower magnetization compared to the FC case for the same applied field. In FC case, when the

samples are cooled through the transition there is a competition between the local field and applied field. If the applied field is stronger than the local field all the spins align in the applied field direction, which gives rise to maximum magnetization in comparison to the same field value in the ZFC case.

In sample T0, the irreversibility is observed at all measurement fields but the maximum in magnetization is observed at 79 K. This matches well with the maximum in χ' of ac susceptibility of the same system. In dc magnetization, depending upon the applied field, the magnitude of ΔM varies with the measuring temperature range. Above 79 K, even though ΔM is observed for small field values, it is not due to AF ordering of the tetragonal phase. This magnetic irreversibility could be a result of the presence of a minor orthorhombic phase and/or presence of short-range interaction between domains at higher temperature (above T_N) giving rise to irreversibility with 500 Oe and 1 kOe field.

Below T_N, the irreversibility in ZFC and FC curves in the undoped sample indicates the magnetic frustration induced by the competing affects of inter-layer ferromagnetism (FM) and intra-layer antiferromagnetic (AFM) order due to the helical spin arrangement. The degree of irreversibility is high for low applied fields. With increasing magnetic field, the degree of irreversibility decreases. This is consistent

with the transformation of the helical magnetic order to a collinear order at extremely high fields. In $SrFeO_3$, the angle between the spins of the neighboring {111} planes has been found to be $\theta = 46^o$. Strong magnetic fields can decrease θ, reducing the irreversibility [25, 26].

In all the doped systems T1-T3, the T_{irr} gets shifted to lower temperatures compared to the undoped T0 system (T3 [32K] < T2 [38K] < T1 [45K]). Above T_{irr}, FC and ZFC magnetization curves overlap in all these systems. This indicates that the minority phases are completely absent. Ti stabilizes the tetragonal structure in this case. Below T_{irr}, M_{ZFC} is decreasing and M_{FC} is increasing, which is generally observed in spin glasses or cluster spin glasses. Addition of more non-magnetic Ti^{4+} is expected to dilute the helical antiferromagnet in to a simple collinear or canted antiferromagnet. At a low field of 100 Oe, the magnetization of Ti doped samples increased with increasing Ti doping (Fig. 4.1(b)) and M-H loop of T3 (Fig. 4.2(d)) shows an increase in the curvature, indicating a tendency of saturation in magnetization for H > 90 kOe. H_C also increases with the increase in Ti doping. These results suggest that the helical antiferromagnetic structure of the parent tetragonal $SrFeO_{3-\delta}$ is progressively getting suppressed with Ti doping.

The existence of mixed valence, the ratio of $Fe^{4+}/Fe^{3+\delta}$, and the consequent competing AFM and FM interactions as well as the site

disorder due to the Ti doping and oxygen vacancies lead to a cluster spin glass state at temperatures below T^*.

4.9 Conclusion

Based on AC Susceptibilty, Magnetization, and low temperature Neutron diffraction measurements on $SrFe_{1-x}Ti_xO_{3-\delta}$ (x=0 to 0.3), it is established that the undoped system exhibits the long-range helical antiferromagnetic order while the Ti doped systems behave as a cluster spin-glass.

References

[1] B.C.Tofield, C.Greaves and B.E.F.Fender ,Mater.Res.Bull 10 (1975) 737

[2] M.Takano, J.Kawachi, N.Nakanishi, and Y.Takeda Journal of Solid State Chemistry 39(1981) 75.

[3] Y.Takeda, K.Kanno,T.Takada, O.Yamamoto, M.Takano, N.Nakayama and Y.Bandol, J.Solid State Chemistry 63(1986) 237.

[4] M.Takano, T.Okita, N.Nakayama, Y.Bando, Y.Takeda, O.Yamamoto and J.B.Goodenough, J.Solid State Chemistry 73(1988) 140.

[5] Junichiro Mizusaki , Masanobu Okayasu, Shigeru Yamauchi, Kazuo Fueki Journal of Solid State Chemistry 99 (1992) 166.

[6] T.C. Gibb, J.Chem.Soc.Dalton Trans.1445 (1985).

[7] J.P.Hodges, S.Short, J.D.Jorgensen, X.Xiong,B.Dabrowski, S.M.Mini and C.W.Kimball Journal of Solid State Chemistry 151(2000) 190.

[8] Peter Alder and Sten Eriksson Z.Anorg. Allg. Chem. 626 (2000) 118.

[9] J.Rodriguez, J.A.Pereda, M.Vallet, J.G.Calbet and J.TejadaMater.Res.Bull 21(1986) 255.

[10] W.H.Meiklejohn and C.P.Bean, Phys.Rev. 102, 1413 (1956).

[11] W.H. Meiklejohn, C.P. Bean, Phys. Rev. 105, 904(1957).

[12] W.H. Meiklejohn, J. Appl. Phys. 33, 1328(1962).

[13] J. Nogues, I.K. Schuller, J. Magn. Magn. Mater. 192,203(1999).

[14] A.E. Berkowitz, K. Takano, J. Magn. Magn. Mater. 200,552(1999).

[15] R.L. Stamps, J. Phys. D: Appl. Phys. 33, R247 (2000).

[16] Mikhail Feygenson, Yuen Yiu, Angela Kou, Ki-Sub Kim, and Meigan C. Aronson, Phys.Rev.B, 81,195445 (2010).

[17] Jun Shen, Jin-Liang Zhao, Feng-Xia Hu, Guang-HuiRao, Guang-Yao Liu, Jian-Feng Wu, Yang-Xian Li, Ji-Rong Sun and Bao-Gen Shen, Appl. Phys. A 99, 853 (2010).

[18] Q.Y. Dong, B.G. Shen, J. Chen, J. Shen, and J.R. Sun, Solid State Comm. 151,112 (2011).

[19] S.Srinath, M.Mahesh Kumar, K.Sahner, M.L.Post, M.Wickles, R.Moos and H.Srikanth Journal of Applied Physics 99 (2006) 08S904.

[20] S.N.Kaul and S.Methfessel, Solid State Comm. 47, 147(1983).

[21] D. Fiorani, S. Viticoli, J.L. Dormann, J.L. Tholence and A.P. Murani, Phys.Rev.B 30, 2776 (1984).

[22] J.L. Tholence, Solid State Comm. 88, 917(1993).

[23] J.L. Tholence, Solid State Comm. 35, 113(1980).

[24] Theo Hahn, International Tables for Crystallography, Volume A: Space-Group Symmetry, Published for The International Union of Crystallography by Springer (2005).

[25] T.Takeda,Y.Yamaguchi and H.Watanabe, J.Phys. Soc.Jpn. 33 (1972) 967.

[26] H. Oda, Y. Yamaguchi, H.Takei and H. Watanabe, Journal de Physique, 38, C1 (1977).

CHAPTER 5

Transport and magneto-transport properties of $SrFe_{1-x}Ti_xO_{3-\delta}$ systems (x = 0 to 0.3)

This chapter describes the results of the transport and magneto-transport studies on $SrFe_{1-x}Ti_xO_{3-\delta}$ (x = 0 to 0.3) carried out by the standard four probe technique using the dc transport option of PPMS. These systems have defects (vacancies) originating from the oxygen deficiency and site disorder caused by a partial substitution of Ti^{4+} at Fe sites. Large change in resistivity due to charge ordering is observed when lowering the temperature. In all the above systems, semiconducting like decrease in resistivity with increase in temperature is observed. The temperature dependence of resistivity is well described by the three dimensional Variable Range Hopping (3D-VRH) model. Magneto-resistance is measured by applying a field of 80 kOe and the results are discussed.

5.1 Introduction

In ABO_3 perovskite systems the transport properties generally are governed by B-site cation and additionally in oxides, by the stoichiometry of the compound. $SrFeO_{3-\delta}$ systems have four distinctly different crystallographic phases with respect to oxygen deficiencies. Stoichiometric $SrFeO_3$ is a metal up to the lowest measurable temperature. Any deviation from stoichiometry transforms the system from a metal to a semiconductor and with further decrease in oxygen stoichiometry, to an insulator.

5.2 Review of earlier work

Transport and magneto-transport in tetragonal $SrFeO_{3-\delta}$ has been studied by a number of groups. A few of the important results are discussed here. Lebon et al [1, 2] reported transport behavior of three different oxygen deficient single crystals. The resistivity of mainly tetragonal $SrFeO_{2.85}$ single crystal (in which 70% tetragonal and 30% orthorhombic phase is present) increases by one order of magnitude at 70 K and around 70 K, a large negative Magnetoresistance (MR) of 90% is observed. The negative MR is attributed to Fe^{4+}- Fe^{3+} charge and magnetic ordering. Williams et al [3, 4] reported the resistivity and MR in two different oxygen deficient samples, namely, $SrFeO_{2.8}$ and

$SrFeO_{2.71}$. In tetragonal $SrFeO_{2.8}$ system, below 70 K an increase in the resistivity and with the application of 120 kOe field a positive MR of 10% is observed from room temperature down to 80 K. Around 80 K, there is a jump from positive MR to negative MR of 80% and this high value of negative MR persists down to low temperatures. The difference in MR observed in this system in comparison to those of single crystals is attributed to the contribution from transport across the grain boundaries.

In view of the reported sensitivity of MR to the microstructure, a study of transport in the present ball-milled tetragonal samples with and without Ti doping, wherein the microstructure shows the presence of nanograins, could yield interesting results.

5. 3 Transport mechanisms in Oxides

The transport mechanism for the mixed-valence manganites and doped semiconductors is discussed mainly using three different models. They are (i) thermal activation or band gap model, ,

(ii) adiabatic nearest-neighbour hopping model of small polarons or small polaron hopping model (SPH), (iii) Variable-

range hopping (VRH) model, . To understand the conduction mechanism in an oxide system, it is imperative to check which of these models describes the observed dependence of resistivity on temperature.

5.3.1 Band gap model

The band gap model has been applied to many semiconductors and insulators in the literature. In this model, a band gap exists between the conduction band and the valence band and if the thermal energy is sufficient to cause thermal excitation of the electrons across the band gap, the electrons excited to the conduction band become available for conduction. If a graph between ρ and , constructed out of the measured ρ (T), is linear, the band gas model holds. However, this simple check yielded a non-linear graph in the present case. Thus, the band gap model is inadequate to explain the conduction process in the systems under investigation.

5.3.2 VRH Mechanism

VRH theory was originally developed to explain the transport in doped semiconductors where electrons are localized by potential fluctuations associated with the dopant. According to the VRH model, if the electron

is not deeply trapped it can hop from one site to another site with the assistance of a phonon [5-10]. At low temperatures if the electron does not have enough energy to hop to the nearest neighboring site, but it is possible to hop further to find a site with a smaller potential difference. Since the hopping range is variable, it is called variable range hopping. According to this model, the resistivity varies as — .

5.3.3 Adiabatic nearest-neighbour hopping model of small polarons

If the electrons are deeply trapped as small polarons, the thermal energy is not sufficient to overcome the deep potential well (deeply trapped electrons) to hop out of its site. In this situation, the hopping is possible through a multiphonon assisted process. The electron is activated to an intermediate state which is a localized state with a higher energy. Then from the thermal energy acquired due to the second phonon the electron hops out from the intermediate state to its nearest-neighbour site or further sites. Hopping to nearest-neighbour site is considered as multi-phonon assisted nearest-neighbour hopping. The hopping to the non-nearest-neighbour site is termed as variable-range hopping of small polarons, because the carrier in both the initial and final states is localized as small polarons [11-16].

If the conduction occurs via the SPH process, a plot of log (ρ/T) against 1/T should be linear. In the present system, this graph yielded a

nonlinear curve. This permits us to conclude that the SPH model cannot account for the conduction process.

5.4 Resistivity and Magnetoresistance of Tetragonal $SrFeO_{3-\delta}$

Resistivity of tetragonal $SrFeO_{3-\delta}$ (T0) sample is measured from 300 K to 5 K using standard four probe method. Figure 5.1 shows the resistivity as a function of temperature in the above temperature range. The shape of the curve is typical of a semiconductor/insulator in that the resistivity monotonously decreases with increasing temperature (T). Since the voltage across the sample T0 at 2 K was well within the compliance voltage of the constant current source, resistivity could be measured over the complete temperature range. Zero-field resistivity data show hysteresis between cooling and warming cycles at $T \approx T_N$. Hysteresis in resistivity between cooling and warming is reported in the literature [1, 2, 17-19] and is attributed to the coexistence of antiferromagnetic and paramagnetic domains. Around 70 K (~ T_N of the tetragonal phase) a large change in slope with a sudden increase in resistivity by at least an order of magnitude is observed, indicating the inter-relationship between the magnetic and transport properties. On further cooling, the increase in resistivity exhibits a power-law behavior. On heating, the sample shows a hysteresis around the T_N. The hysteresis starts at 72 K and closes at 45 K.

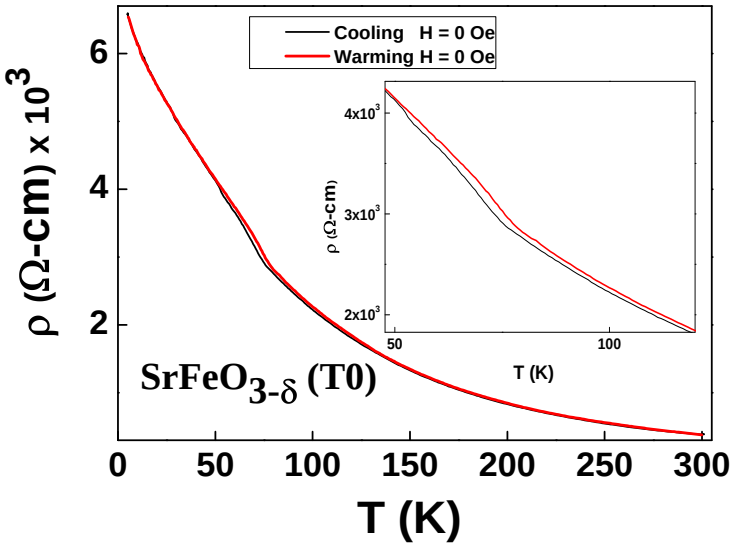

Figure 5. 1. Resistivity of Tetragonal $SrFeO_{3-\delta}$ system measured while cooling and warming in zero magnetic field.

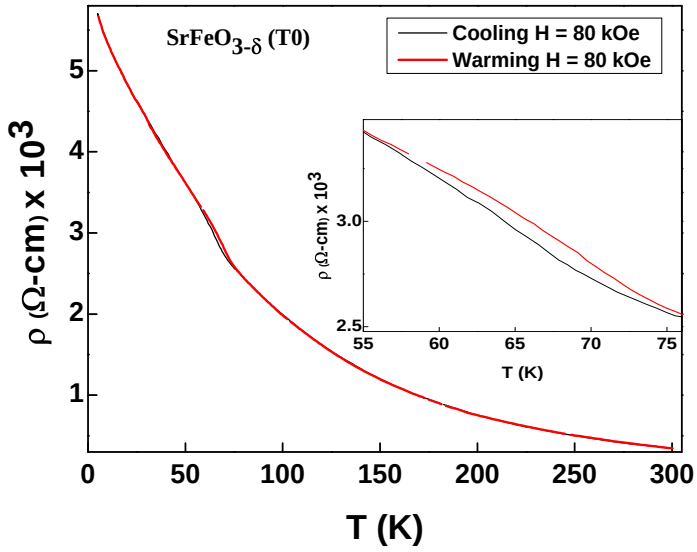

Figure 5.2. Resistivity of Tetragonal $SrFeO_{3-\delta}$ system measured while cooling and warming in the presence of 80 kOe field.

Figure 5.2 depicts the temperature variation of resistivity, measured in the presence of 80 kOe magnetic field during both cooling and warming cycles. The overall shape of the resistivity curve is very similar to that observed in the zero field case. The measured resistivity at the lowest temperature is smaller than the zero field and also temperature range over which the hysteresis observed between the cooling and warming cycles is small in comparison to the zero field case.

The magnetoresistance (MR) is the fractional change in resistivity (ρ) on the application of external magnetic field and is defined as MR = [ρ(H) - ρ (0)] / ρ (0). To measure MR in these materials, ρ(H) is measured both while cooling and warming in the presence of a field of 80 kOe.

A comparative assessment of the temperature variation of zero-field resistivity ρ(0) and the 80 kOe resistivity ρ(H) is carried out in Figure 5.3 for the warming cycles. It is clear from the figure that ρ(H) shows a decrease in comparison to the ρ(0) as a function of temperature, indicating negative MR. With increasing temperature, MR decreases indicating decreasing trend in magnetic interactions, possibly by a hopping electron. The tetragonal phase transition is clearly visible in both cases as a slope change, with a slightly reduced temperature for the 80 kOe curve. The calculated MR is shown in Figure 5.4. MR is negative

in the entire temperature range with a maximum of -15.2% at 76 K, which is close to the T_N of the sample. The maximum MR close to T_N is due to the enhanced spin fluctuations. Even though signatures of cubic and orthorhombic minor phases are observed in the low field magnetization data of T0, no such signatures are noticed either in the resistivity or MR of this sample, indicating that the trace

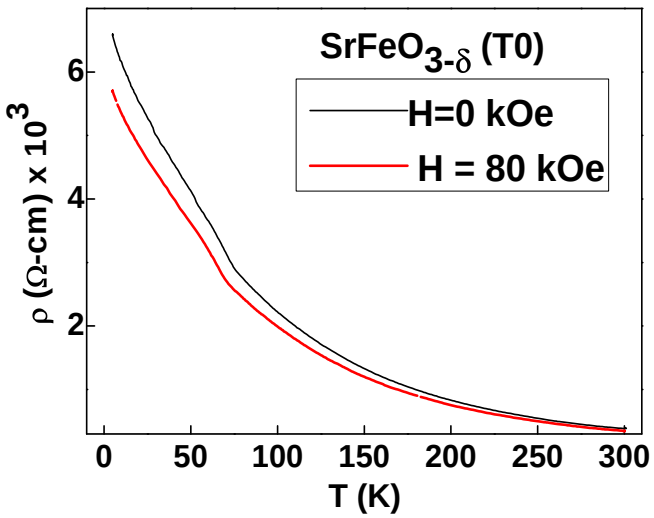

Figure 5.3. Resistivity of Tetragonal $SrFeO_{3-\delta}$ system measured in the warming cycle at H = 0 and H= 80 kOe.

phases, if present, are essentially of no consequence. The relatively smaller MR (compared to those reported in the literature) in the present case could be due to the presence of nanograins (seen in microstructure).

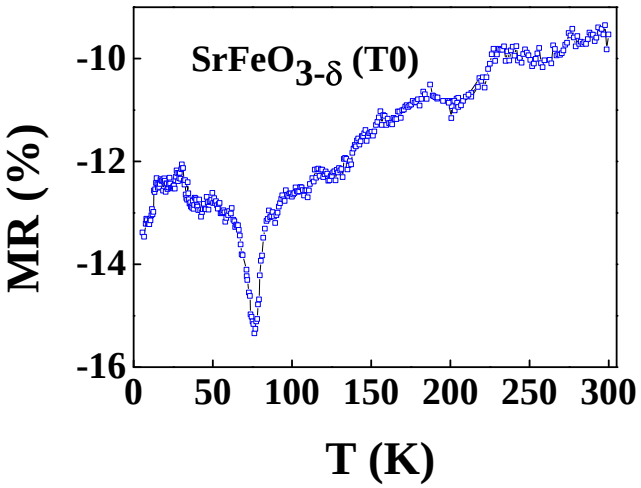

Figure 5.4. Temperature dependence of MR of Tetragonal $SrFeO_{3-\delta}$.

5.4 Resistivity and Magnetoresistance of Ti doped $SrFeO_{3-\delta}$

Resistivity and magnetoresistance of 10%, 20% and 30% of Ti doped $SrFeO_{3-\delta}$ (T1, T2 and T3)are measured by the four probe method on PPMS. Figure 5.5 shows ρ (H =0) of T1 measured in both cooling and warming cycles. There is a sharp increase in resistivity close to 74 K and unlike in T0, ρ(H=0) could be measured only down to 55 K, which lies above the magnetic ordering temperature of T1 (50 K). The ρ(H=0) at 55 K is 4.2 x 10^4 Ω-cm, which is much higher in comparison to T0. The hysteresis between the cooling and warming cycles is also much smaller

in comparison to T0. Figure 5.6(a) shows ρ (H =80 kOe) of T1 measured in both cooling and warming cycles. MR as a function of temperature is shown in Figure 5.6(b). It is interesting to note that from RT to 105 K the MR is positive with a maximum value of 11 % close to RT. The MR decreases continuously with decrease in temperature and at 105 K MR changes sign and becomes negative with further decrease in temperature the negative MR increases and close to 58 K reaches a maximum of 4.3%. The positive MR observed in similar systems is, in general attributed to the opening of the gap.

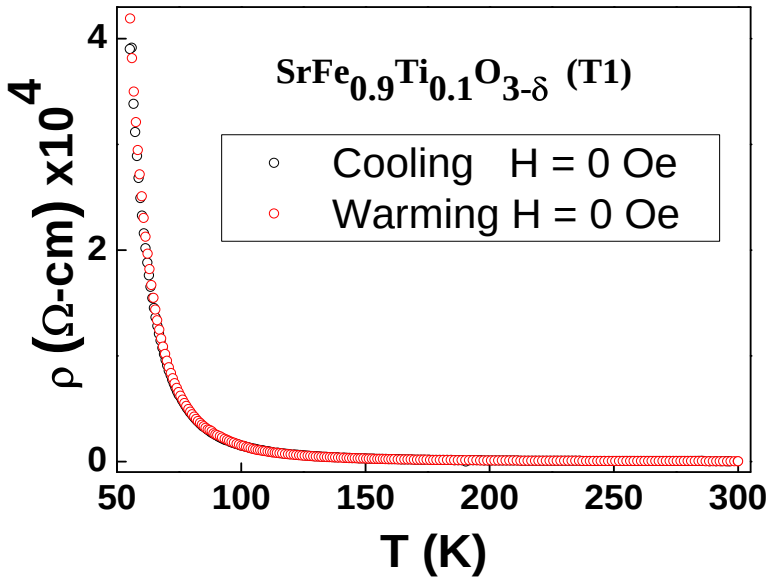

Figure 5.5. Resistivity of $SrFe_{0.9}Ti_{0.1}O_{3-\delta}$ system measured in zero field while cooling and warming.

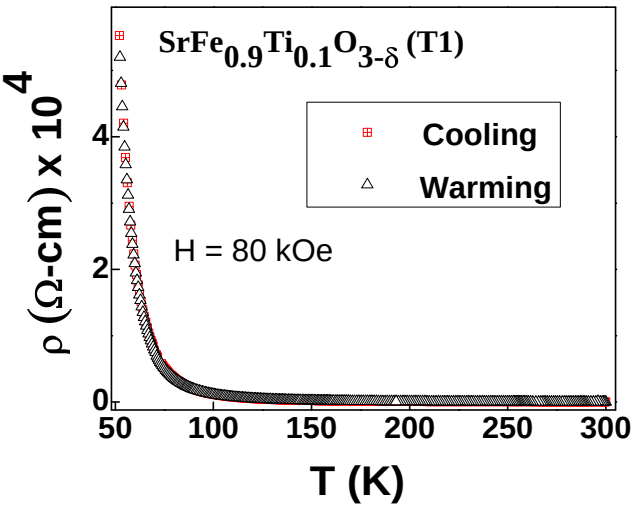

Figure 5.6(a) Resistivity of $SrFe_{0.9}Ti_{0.1}O_{3-\delta}$ system while cooling with zero and 80 kOe field.

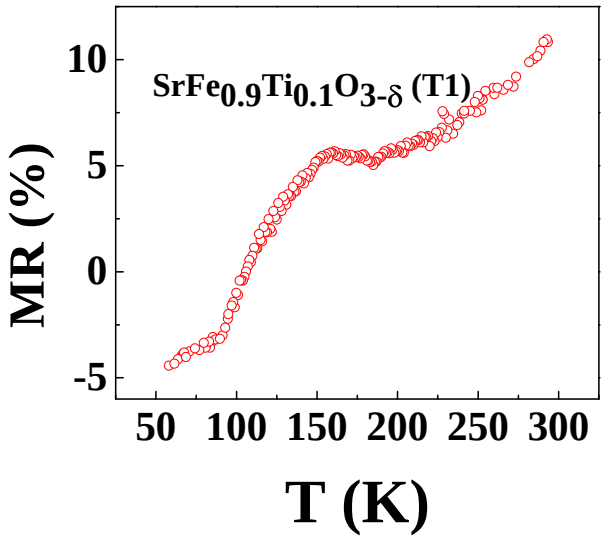

Figure 5.6 (b) Temperature dependence of MR of T1 at H = 80 kOe.

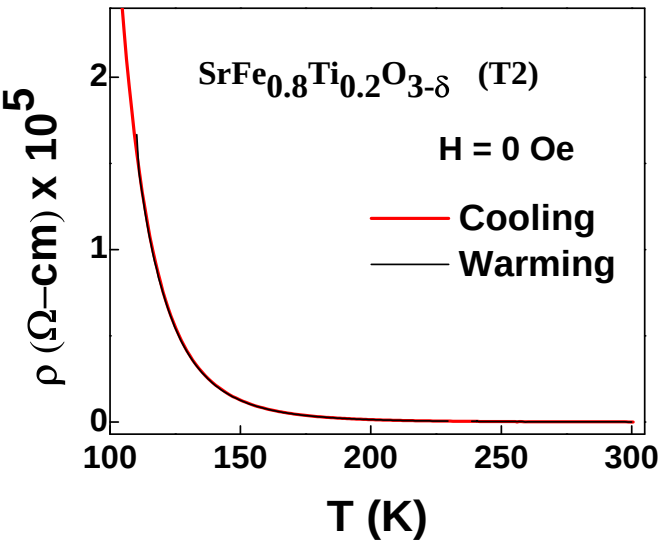

Figure 5.7. Resistivity of $SrFe_{0.8}Ti_{0.2}O_{3-\delta}$ system measured in zero field while cooling and warming.

ρ (H=0) of T2 measured while cooling and warming is shown in figure 5.7. The ρ(H=0) increases more sharply at a higher temperature of 140 K and the resistivity could be measured only up to 104 K, reaching a maximum value of 2.3 x 10^5 Ω-cm. No hysteresis is observed between the cooling and warming cycles. The figure 5.8 shows the cooling and warming ρ(H = 80 kOe) data of T2 system. Field has a very little effect on the resistivity of this sample, as the sample is in the paramagnetic

state throughout the measurement temperature range. The lowest temperature up to which ρ(H = 80 kOe) could be measured and the value of resistivity at this temperature match well with those of zero field measurement. The calculated MR for the T2 is shown in figure 5.9. A small positive MR of 0.9% is observed close to RT. MR decreases continuously with

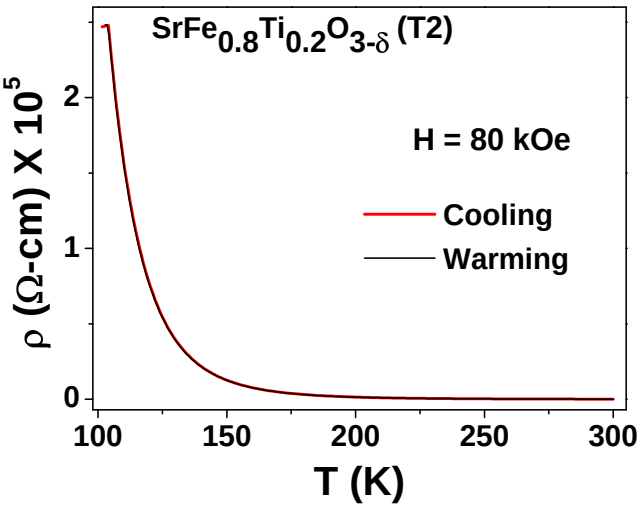

Figure 6.8 Resistivity of $SrFe_{0.8}Ti_{0.2}O_{3-\delta}$ at H = 80 kOe.

decrease in T. The sign of MR changes at 160 K and with further lowering of temperature, negative MR increases and reaches a maximum value of -1.1% at 105 K.

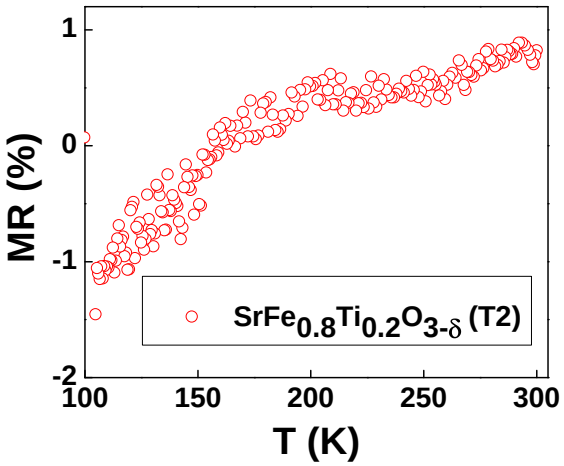

Figure 5.9 Temperature dependence of MR in $SrFe_{0.8}Ti_{0.2}O_{3-\delta}$ at 80 kOe field.

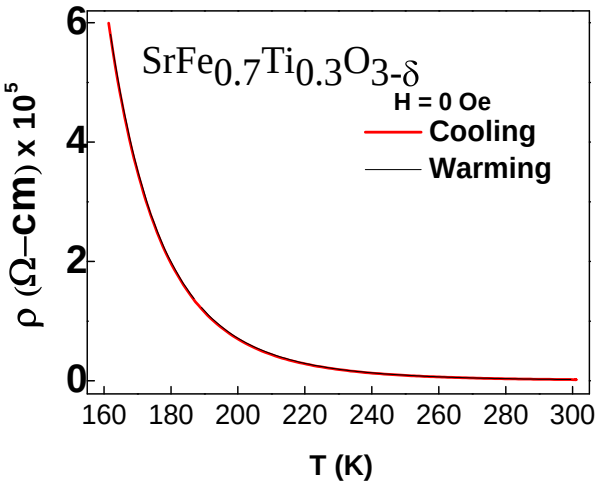

Figure 5.10 Resistivity of $SrFe_{0.7}Ti_{0.3}O_{3-\delta}$ in zero field.

Figure 5.10 shows ρ(H =0) of T3 measured in cooling and warming cycles. Similar to T2 sample, no hysteresis is observed between the cooling and warming cycles. A sharp increase in ρ is seen for T< 190 K. The resistivity value reaches the maximum compliance value at T =161 K and hence ρ (T) could not be measured below this temperature. ρ(H = 80 kOe, T) of T3 is shown in figure 5.11. Similar to the zero field data, no hysteresis is observed in this case also and the resistivity could not be measured below 164 K.

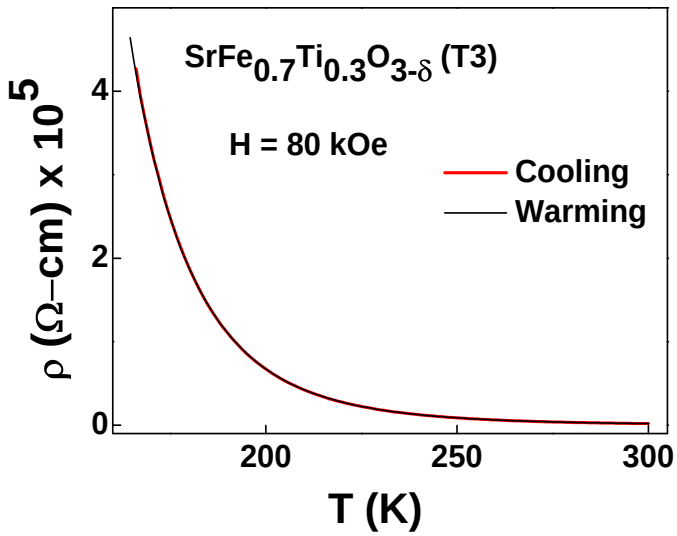

Figure 5.11 Resistivity of $SrFe_{0.7}Ti_{0.3}O_{3-\delta}$ at H = 80 kOe.

The calculated MR is shown in figure 5.12. MR is negative in the entire temperature range. At room temperature there is not much change in

MR and negative MR increases continuously with the decrease in temperature and finally at 164 K reaches 9%.

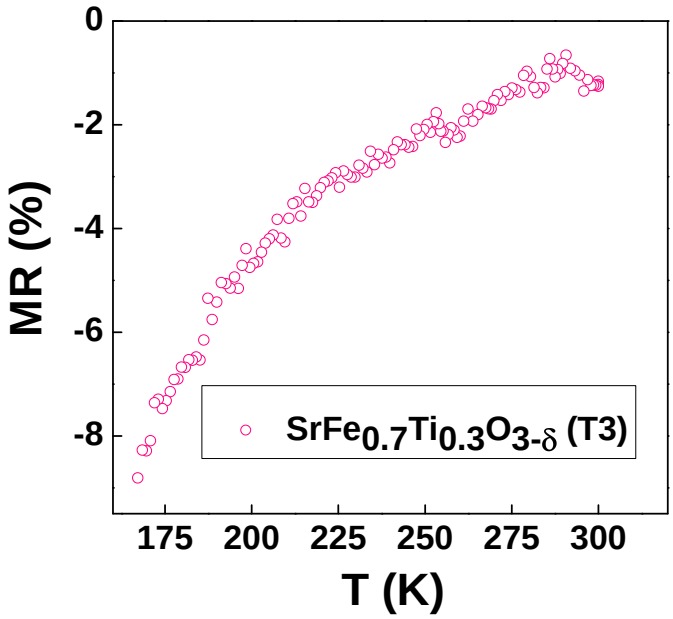

Figure 5.12 Change in MR with 8T field of $SrFe_{0.7}Ti_{0.3}O_{3-\delta}$.

In all the Ti doped samples, the resistivity could be measured only in the paramagnetic region and this explains the small magnitude of MR.

5.5 3D Variable Range Hopping and Data Analysis

The most notable aspect of the transport properties is the observation of 11% positive MR at room temperature and positive MR

from RT to 104 K for T1. MR has a small positive value at RT for T2 and remains positive up to 160 K. It is obvious that the increase in resistivity on the application of a magnetic field is related to either the opening up of the gap between the bands or due to the increased scattering of electrons. ρ(H= 0, T) and magnetization data point to localized electron spin moments in all the samples giving rise to a semiconducting behavior. Such antiferromagnetic-insulators are classified as Mott insulators where a metal-insulator (M-I) transition could occur due to electron-electron correlation. Anderson pointed out that the disorder in a solid could introduce random potential energy in the lattice which ultimately leads to a localization of the electron wave function.

At low temperatures, Anderson localization occurs in many disordered metals, semiconductors and perovskite type oxides. The most striking examples of this category are high T_C superconductors and colossal magnetoresistance oxides like La(SrMn)O_3. In these materials, conduction mechanism is governed by 'variable range hopping' (VRH), where the hopping energy (*W*) varies with a temperature [20-24].
The resistivity in the present system of $SrFe_{(1-x)}Ti_xO_{3-\delta}$ [25-27] is analyzed in terms of 'variable range hopping', a mechanism where the electron hops between localized antiferromagnetic states. Such hopping mechanism can be described using the following equation

–

(5.1)

where the dimensionality of the hopping is 3, T_0 is a characteristic temperature related to the density of states at the E_F. In materials undergoing VRH, the plot of ln ρ vs $T^{-1/4}$ appears as a straight line. The localization length ' ', calculated from the relation

(5.2)

' ' indicates the extent to which the 3d orbitals of the metal atom overlap with the oxygen 2p orbitals.

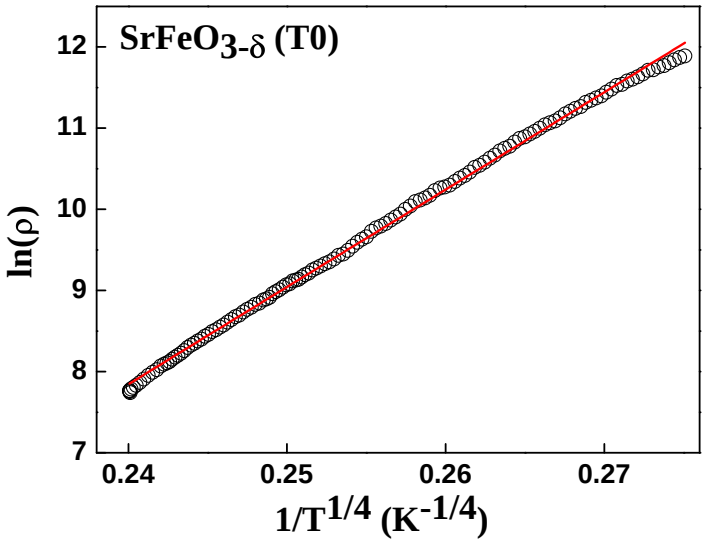

Figure 5.13(a) Resistivity of T0 along with the fit (straight line passing through the data points) based on the three-dimensional variable range model.

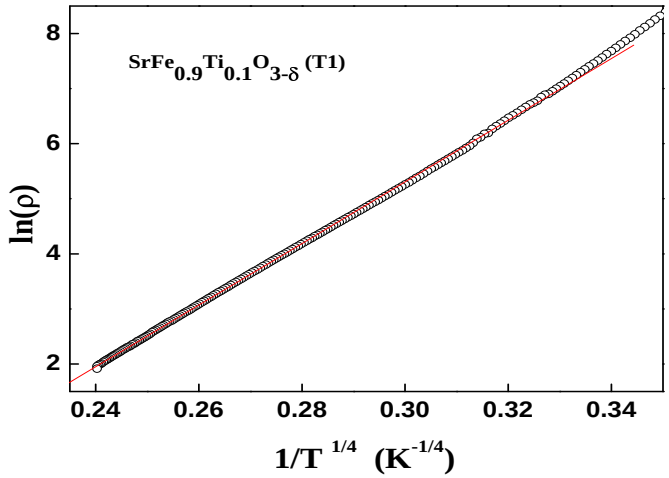

Figure 5.13(b) Resistivity of T1 along with the fit (straight line passing through the data points) based on the three-dimensional variable range model.

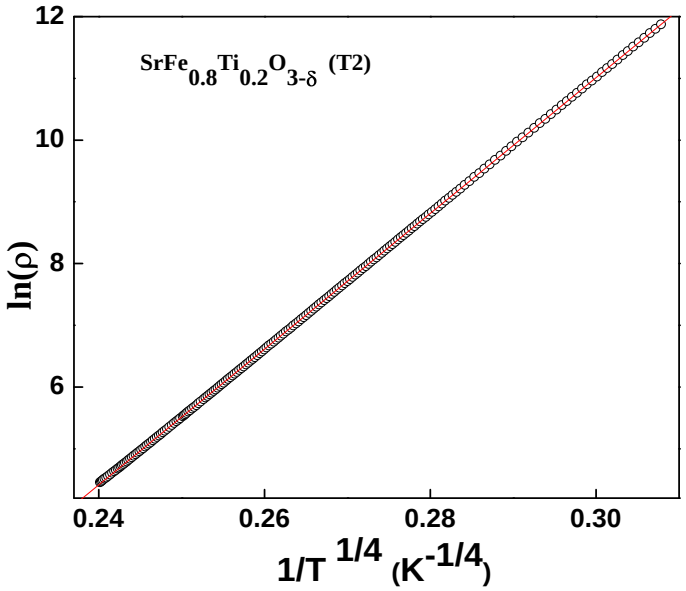

Figure 5.13(c) Resistivity of T2 showing fit to variable range hopping model

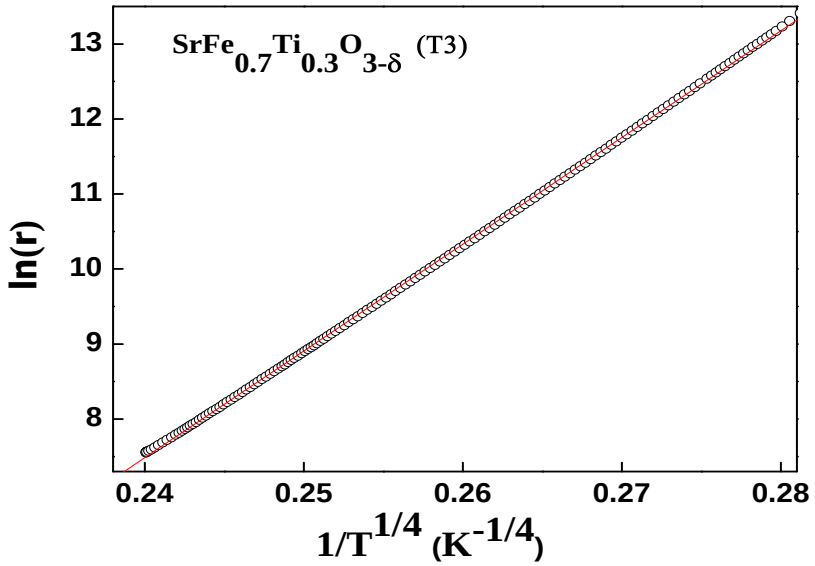

Figure 5.13(d) Resistivity of T3 along with the fit (straight line passing through the data points) based on the three-dimensional variable range model.

Figure 5.13(a), 5.13 (b) shows the fits to the resistivity data of T0 in the temperature range 130-270 K and to ρ(H = 0, T) for T1 from 185 K to 300 K. The values of T_0 and calculated from Eqs. (5.1) and (5.2) for different samples are tabulated in Table 5.1. For temperatures lower than 130 K, ρ(H = 0, T) for T0 did not fit to either d=3 or 2, indicating a mechanism of conduction that is more complex than variable range hopping. This is understandable considering the disproportionateness of varying valence states of Fe at low temperatures and their arrangement in the crystal lattice.

Table 5.1 Calculated values of T_0 , l, R, and W at 300 K for Sample T0, T1, T2 and T3 at 0 and 80 kOe .

Sample	Field(kOe)	Range(K)	T0(K)	l(Å) localization length	R (Å)	W (mev)
T0	0	142-300	5.65×10^{5}	2.09	5.7	35.8
	80	142-300	6.79×10^{5}	1.97	5.6	37.8
T1	0	78-299	9.81×10^{6}	0.81	4.5	72.8
	80	86-192	1.01×10^{7}	0.80	4.5	72.8
T2	0	111-299	1.46×10^{8}	0.33	3.6	142
	80	103-299	1.44×10^{8}	0.33	3.6	142
T3	0	160-300	4.10×10^{8}	0.23	3.2	202
	80	165-300	3.91×10^{8}	0.24	3.2	202

In a solid with a high degree of disorder, a large network of varying potential barriers hampers the mobility of the electron and in such cases, the electron percolates through the network in a set of varied jumps than a single jump, assisted by the phonons to reach the final

state. The energy needed (W) is gained from the phonons and the electron attains its final state through the indirect hops assisted by the two levels of phonon energy. The necessary energy for a hop can be calculated using the relation,

$$W = 3/[4\pi R^3 N(E_F)] \qquad \text{- (5.3)}$$

where R is the hopping distance in Å calculated from

$$R = (3\ /[(2\pi N(E_F)kT])^{1/4} \qquad \text{- (5.4)}$$

The calculated values of T_0, , R and W (R&W at RT) using Eqs. (5.1)- (5.4) for all the samples at H= 0 and H= 80 kOe are given in Table 5.1. A constant value for density of states at the Fermi level, $N(E_F)$, 3.6 x 10^{22} $eV^{-1}cm^{-3}$, estimated for the parent compound [28] is taken for all the doped samples as well. From the table, it can be noted that increasing magnetic field causes an increase in T_0, which, in turn, for the samples T0 and T1 causes a decrease in the localization length ' ' while the field has practically no effect on T_0 and in the samples T2 and T3.

It is known that the spatial extension and the orbital overlap could decide the overall increase or decrease of resistance depending on which one is greater. A comparison between the localization lengths ( ) of measured data at H = 0 and H = 80 kOe indicates that the value of ' ' at 80 kOe is smaller than that calculated for H = 0 (Table 5.1). A decrease

in localization length directly affects the overlap integral resulting in the shrinkage of orbital overlap causing an increase of the resistance with field. On the other hand, with Ti doping the differences in the values of T_0 and are marginal influencing the overall magnetoresistance, which is very small.

5.6 Conclusion

ρ(H=0, T), ρ(H= 80 kOe, T) is measured in both cooling and warming cycles for T0, T1, T2 and T3 samples. The resistivity of the samples increase with increase in doping which can be understood due to the increase in disorder and also with the decrease in the overlap between the metal and oxygen orbitals. MR is negative and the maximum MR is found to be close to the T_N of the undoped sample. The small MR in this case may be due to the increase in resistivity arising due to the nanograin boundaries. All the Ti doped samples show completely insulating behaviour much above the magnetic ordering temperature, hence the field has a very little role to play in changing the resistivity. VRH mechanism seems to explain the transport in the temperature range of 150 – 300 K.

References

[1] A. Lebon, P. Alder, C. Bernhard, A.V. Boris, A.V. Pimenov, A. Maljuk, C.T. Lin, C. Ulrich and B.Keimer Phy.Rev.Lett. 92(2004) 037202.

[2] P. Adler,A. Lebon,V. Damljanovi C. Ulrich, C. Bernhard, A. V. Boris, A. Maljuk, C. T. Lin,and B. Keimer Phys.Rev.B 73, 094451 (2006).

[3] E. K. Hemery, G. V. M. Williams, and H. J. Trodahl, Phys.Rev.B 75, 092403 (2007).

[4] G.V.M. Williams, E.K. Hemery and D. McCann, Phys.Rev.B 79, 024412 (2009).

[5] M. Jaime,V. Salamon ,V. Pettit, V. Rubinstein, R.E. Treece, J.S Horwitz and D.B. Chrisey, Appl. Phys. Lett. 68, 1576 (1996)

[6] M. Jaime,V. Salamon ,V. Pettit, V. Rubinstein, R.E. Treece, J.S Horwitz and D.B. Chrisey, Phys. Rev.B 54, 11914 (1996).

[7] M. Viret, L. Ranno and J M D Coey, Phys. Rev.B 55, 8067 (1997)

[8] V. H. Crespi, Lu Li, Y.X. Jia , K. Khazeni , A Zetll and M L Cohen Phys. Rev.B 53 14 303 (1996)

[9] Y. X. Jia, Lu Li, K. Khazeniu , D.Yen , C. S. Lee and A. Zettl Solid State Commun. 94 917 (1995)

[10] J. M. D. Coey, M. Viret, L. Ranno and K. Ounadjela, Phys.Rev.Lett.75, 3910 (1995)

[13] M.Born, J.R. Oppenheimer, Ann.Phys.84, 457, (1927)

[14] D.Alder: In Handbook on Semiconductors Vol.1, ed. By W.Paul ,North-Holland, Amsterdam P.805 (1982).

[15] P.W. Anderson, Phys.Rev. 109, 1492 (1958)

[16] Aritra Banerjee, Sudipta Pal, E. Rozenberg and B.K. Chaudhuri, J.Phys.: Matter 13, 9489 (2001).

[17] Y.M. Zhao, X.J. Yang, Y.F. Zheng, D.L. Li, S.Y. Chen, Solid state comm. 115, 365 (2000).

[18] Y.M. Zhao,R.Mahendiran, N. Ngugen, B. Raveau and R.H. Yao, Phys.Rev.B 64, 024414 (2001).

[19] Y. M. Zhao and P. F. Zhou, J. Magn. Magn. Mater. 281, 214 (2004)

[20] N.F. Mott, Phil.Mag. 19,835 (1969)

[21] N.F. Mott, Phil.Mag. 22,7 (1970)

[22] W. Brenig, G.H. Döhler and P. Wolfle, Z. Physik 258, 381 (1973)

[23] V. Ambegaokar, B.I. Halperin and J.S. Langer, Phys.Rev. 4, 2612 (1971)

[24] A.L. Efros J.Phys. C9, 2021 (1976)

[25] S.Srinath , M.Mahesh Kumar, M.L.Post, and H.Srikanth Phys.Rev.B 72, 054425 (2005).

[26] P.S. Prabhu, M. S. Ramachandra Rao, U. V. Varadaraju, and G. V.Subba Rao, ibid. 50, 6929 (1994).

[27] R. K. Nkum, W. R. Datars, Phys. Rev. B 46, 5686 (1992).

[28] S. Mathi Jaya, R. Jagadish, R. S. Rao, and R. Asokamani, Phys. Rev. B **43**, 13274 (1991).

CHAPTER 6

A.C Conductivity in $SrFe_{1-x}Ti_xO_{3-\delta}$ systems

This chapter presents the results of impedance measurement carried out on $SrFe_{1-x}Ti_xO_{3-\delta}$ (x=0 to 0.3) in the frequency range of 40 Hz – 1 MHz from RT to 450°C. Complex impedance spectroscopy data are analyzed based on Cole-Cole type impedance response function and Jonscher's universal power law.

6.1 Introduction

Compounds of the Ruddlesen-Popper type, to which $SrFeO_3$ belong fall close to the colossal magnetoresistive manganites that have similar structural and magnetic properties [1,2, 3]. Such mixed oxide conductors [4,5] can be used as oxygen permeation membranes [6-9] in fuel cells, electrochemical gas sensors [10-12] and catalysts[8]. Fe doped $SrTiO_3$ (STF) [13] due to the interesting transport properties at relatively high temperatures and good thermodynamic stability over a range of temperatures and oxygen partial pressures are considered for application as electrochemical electrodes and also for oxygen sensors [14-18] . STF is a continuous solid solution between strontium titanate ($SrTiO_3$) and strontium ferrite ($SrFeO_3$) [19]. Strontium titanate is a wide-band-gap semiconductor (Eg =3.2 eV at T=0 K) with low conductivity in the undoped state [20] while substitution of Fe for Ti, results in a systematic decrease in band gap and an increase in electron, hole and oxygen vacancy density, providing in turn, mixed conductivity with high levels of electronic and ionic conductivities [21-23].

6.2 Review of the earlier work

Conductivity in Fe doped $SrTiO_3$ (STF) system for low concentration (7 % of Fe) below RT is investigated by Chen.et.al. [24-26]. The temperature dependent conductivity below RT is governed by variable range hopping (VRH) [24] conduction. The presence of disorder arising due to the oxygen vacancies and site disorder [27] resulting because of the random occupation of Fe and Ti determines the conductivity. Variation of temperature coefficient of resistance (TCR) is technologically important for gas sensing applications and is an active area of investigation. The TCR is mainly governed by the concentration and mobility of charge carriers and the band gap. Change in NTCR (negative) to PTCR (positive) is observed in a number of oxide systems by tuning one of the above mentioned properties. In STF solid solution 35% of Fe concentration [8] is reported to have zero TCR for a oxygen pressure range of 10^{-14} to 10^{4} Pa and temperature range of 750 to 1300 °C. In STF system, with increase in Fe concentration the band gap decreases and the Fermi level moves closer to the valence band. For x =0.35 this results, in an exact balance between the negative and positive contributions arising due to the hole concentration and hole mobility [28].

6.3 Experimental details

The impedance measurements were carried out on circular pellets with two identical electrodes (silver paste) applied to the faces of the samples. Agilent 4294A impedance analyzer is used with the frequency range of about 40 Hz to 1 MHz to collect the impedance data.

6.4 Results and Discussion

Figure 6.1 (a)- 6.1(d) shows the plot of real part (z') versus imaginary part (z'') of the complex impedance (Cole-Cole plot) for all the samples at different temperatures. The data shows single semicircular arc. The single arc indicates that the contribution to the impedance is mainly from bulk. The grain boundary contribution [29] is not observed in the measured frequency range. However, the zoomed data shows that the real part of the impedance is shifted from the origin indicating the presence of another arc at higher frequencies arising from the grain boundary region. Due to the limited frequency (of 1 MHz) the grain boundary arc is not seen in the present data. The impedance data can be described using the expression for the complex impedance (z) given by Cole-Cole

$$Z = Z_{\infty} + \frac{(Z_0 - Z_{\infty})}{[1 + (i\omega\tau)^{\alpha}]} \qquad \text{---------- (6.1)}$$

Where Z_0 is the static impedance, Z_∞ is the impedance at high frequencies, ω is the angular frequency, τ is the mean relaxation time and α is the angle of the semicircular arc. The data is fitted using this expression and the various impedance parameters are obtained. Figure 6.2 shows the dc conductivity calculated from the Cole-Cole analysis. It can be seen from the figure that both 20 and 30% Ti doped samples show positive temperature coefficient of resistance (PTCR)

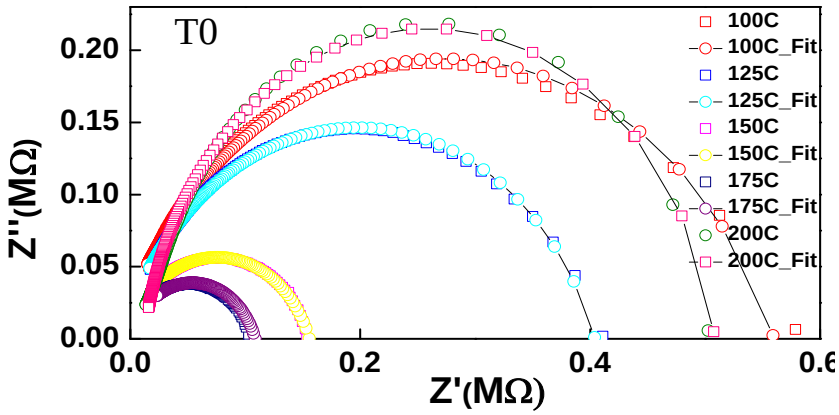

Figure 6.1 (a). Cole-Cole plot of $SrFe_{1-x}Ti_xO_{3-\delta}$ (T0) with NLLS fit based on eqn (6.1) at selected temperatures.

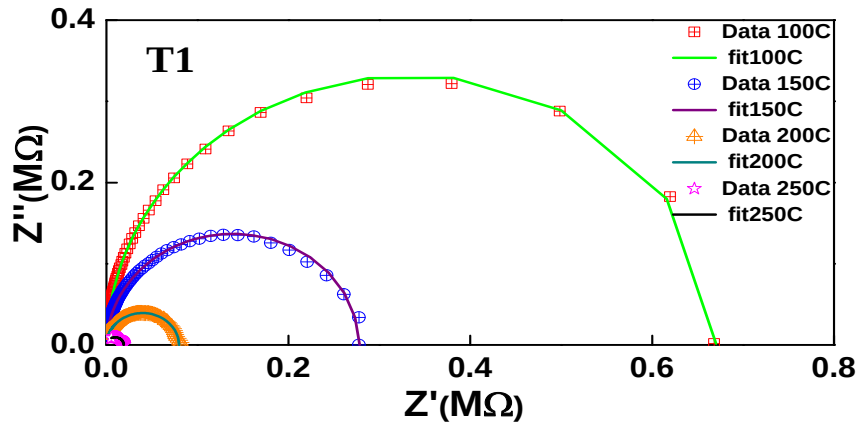

Figure 6.1 (b). Cole-Cole plot of $SrFe_{1-x}Ti_xO_{3-\delta}$ (T1) with NLLS fit based on eqn (6.1) at selected temperatures.

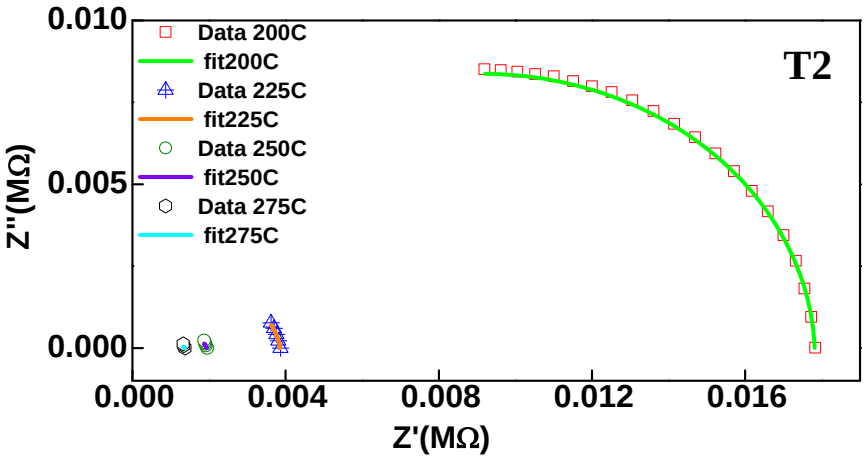

Figure 6.1 (c). Cole-Cole plot of $SrFe_{1-x}Ti_xO_{3-\delta}$ (T2) with NLLS fit based on eqn (6.1) at selected temperatures.

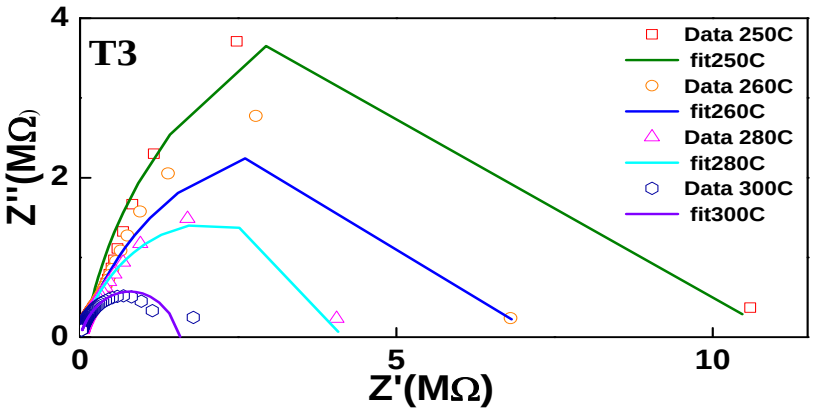

Figure 6.1 (d). Cole-Cole plot of $SrFe_{1-x}Ti_xO_{3-\delta}$ (T3) with NLLS fit based on eqn (6.1) at selected temperatures.

over the temperature range from RT to 175 °C. The conductivity of 30 % Ti doped sample decreases considerably in comparison to the undoped sample.

Ac conductivity is calculated using the expression,

$$\sigma' = Y'(t/A) = [\frac{Z'}{(Z'^2 + Z''^2)}](t/A) \qquad \text{---------- (6.2)}$$

where Z' and Z'' are the real and imaginary parts of impedance, Y' the real part of the admittance, t the thickness (m) and A the area (m^2) of the sample, respectively. Temperature was stabilized (± 0.5 ^oC) at 10^oC intervals, while sweeping Z* as a function of frequency.

The ac conductivity (σ') derived from Eq. (2) is shown in figure. 6.3 as a function of *f* at temperatures $50 \leq T \leq 450^oC$. The low frequency $\sigma'(f, T)$ data show little or no variation, corresponding to the frequency-independent part, σ_{dc}. At higher frequencies, the $\sigma'(f, T)$ spectra show dispersion, indicating the onset of ac conductivity.

The ac conductivity, $\sigma'(f, T)$, is generally described using Jonscher's power laws, which were found to be universal in many materials such as disordered solids and ionic conducting glasses.

$$\sigma'(f) = \sigma_{dc}[1 + (\frac{\omega}{\omega_p})^n] \qquad \text{----------} \quad (6.3)$$

where σ_{dc} is the dc conductivity, ω and ω_p are the applied frequency and the relaxation frequency in radians, respectively, and n is an exponent. A long-range hopping of mobile charges will occur at high temperatures and low frequencies, resulting in a Jonscher-type hopping conduction. Depending on the variation of the conductivity with frequency in

general two regimes are found in the literature, for frequencies $f < f_p$, the ion hopping termed as "diffusive", leading to a

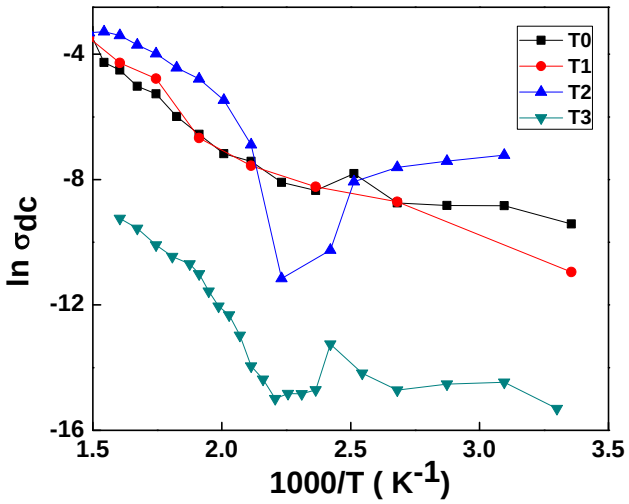

Figure 6.2 DC conductivity estimated from Cole-Cole fit vs 1000/T.

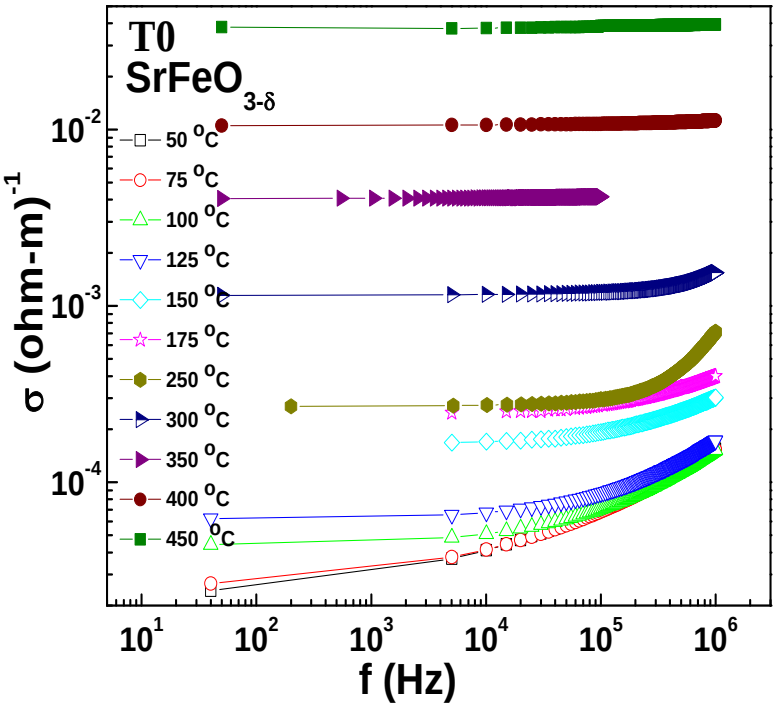

Figure 6.3 Frequency dependent AC Conductivity with Jonscher's fit of T0 at different temperatures.

frequency-independent conductivity σ_{dc}. For $f > f_p$, the frequency dependent dispersion in the conductivity is observed due to the inhomogeneous potential distribution. For the undoped sample in the entire temperature range of 50°C to 450°C the conductivity increases with T and also with increase in frequency. The frequency dependency is described by eqn (6.3) and the fits based on this equation are shown in figure 6.3, with n value lying between 0.5 to 0.6 for temperatures between 50°C and 175°C whereas n value is more than 1 for temperatures in the range of 250-450°C. In the low temperature region (50^oC -175°C) $0 < n < 1$ indicates that the conduction to be of translational hopping motion whereas at high temperatures $1 < n < 2$ indicating the conduction mechanism to be that of well-localized hopping and/or reorientational motion.

T1 sample exhibits a power law behavior of the conductivity and in the entire temperature range there is an increase in the conductivity with both temperature and also with the frequency. The ac conductivity of T2 sample increases with increase in frequency, however the temperature dependence of conductivity shows an interesting behavior. Figure 6.4 shows the ac conductivity as a function of frequency of T2 sample measured at different temperatures. For temperatures < 175°C, conductivity decreases with T whereas for T > 175° C conductivity increase with increase in T. The decrease in conductivity for

temperatures in the range of RT to 175 °C is clearly seen in figure. 6.5 where the temperature dependence of the ac conductivity is plotted as a function of temperature measured at different frequencies. The decrease in ac conductivity with increase in T is termed as positive temperature coefficient of resistance (PTCR). PTCR is earlier reported in STF system by [28]. The change in TCR from negative to positive in this system is reported to be due to the change in band gap with change in Fe content [28]. The PTCR seen in the ac conductivity data matches well with the dc conductivity data obtained from the Cole-Cole analysis based on eq (6.1) which is shown in figure 6.5. In general the electrical conductivity depends

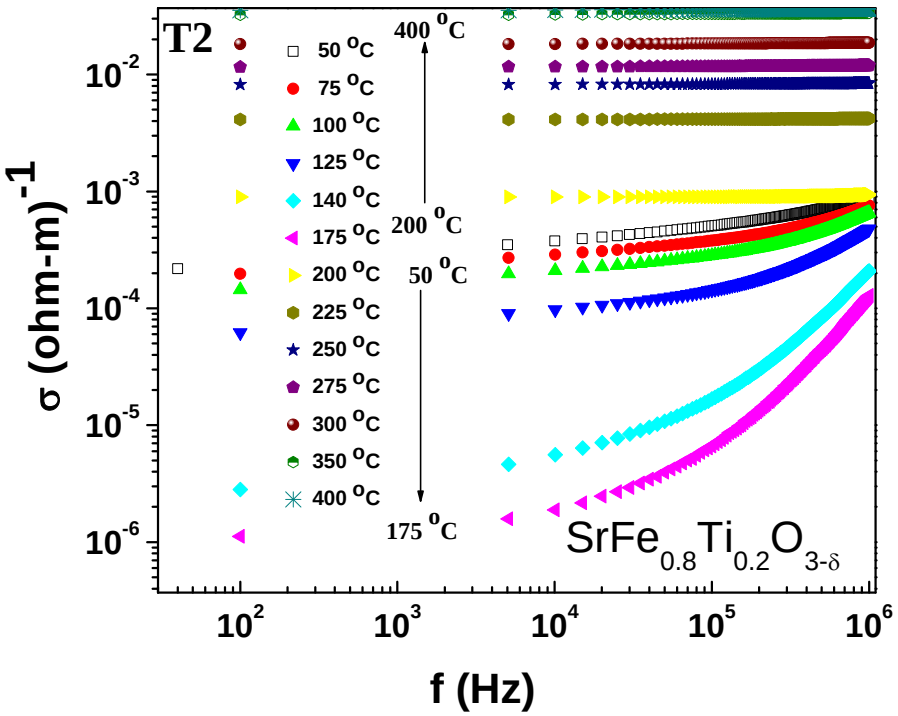

Figure 6.4. Frequency dependent AC Conductivity data of T2($SrFe_{0.8}Ti_{0.2}O_{3-\delta}$) at different temperatures.

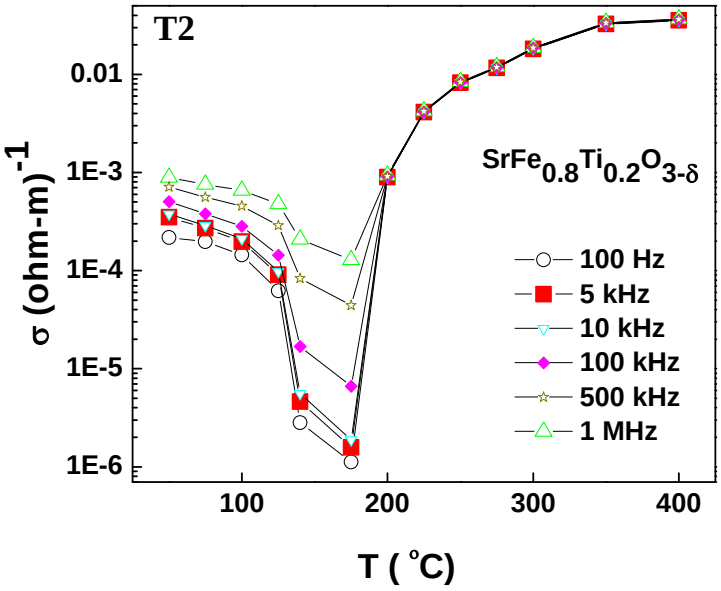

Figure 6.5 Temperature dependent AC Conductivity data of T2

on the mobility and concentration of charge carriers and both of them are temperature dependent. The sign of TCR is decided by the temperature dependence of both the mobility and concentration [28].

The impedance data can also be analyzed in terms of electric modulus. The real and imaginary electric modulus is related to the impedance by $M' = \omega C_0 Z''$ and $M'' = \omega C_0 Z'$ where ω is the angular frequency and C_0

is the geometrical capacitance given by $(\varepsilon_0 A/t)$. Figure 6.6(a) shows the real part of the electric modulus as a function of frequency for T1 at different temperatures. M′ has a small value at low frequencies and increases with increase in frequency. Figure 6.6(b) shows the imaginary part of electric modulus (M′′) versus log (f) at different temperatures. M′′ vs. log f plot shows a peak in M′′ and the peak shifts to higher frequencies with increase in temperature. The low frequency side of the peak is reported to signify the ion hopping from one site to the neighboring site whereas frequencies above the peak signify the localized motion [30]. The relaxation time and the activation energy can be estimated by plotting the variation of peak frequency with temperature. In general, the appearance of peak in the modulus spectrum indicates the conductivity relaxation. Figure 6.7(a) and 6.7(b) show the real and imaginary part of M as a function of frequency for T2. For T2, M′ increases systematically with increase in temperature from RT to 125 °C and then there is a sudden increase in M′ at 140 °C and 175°C, beyond this temperature there is a sudden drop in M′ at 200°C and further decrease in at 225 °C. This is the temperature where change in TCR is observed. M′′ vs. log (f) for T2 sample (figure 6.7(b)) shows that with increase in temperature the peak shifts to lower frequencies from RT to 175°C (in contrast with T1 sample, figure 6.6 (b)) and

beyond 175°C the peak shifts to higher temperature as expected for systems with NTCR.

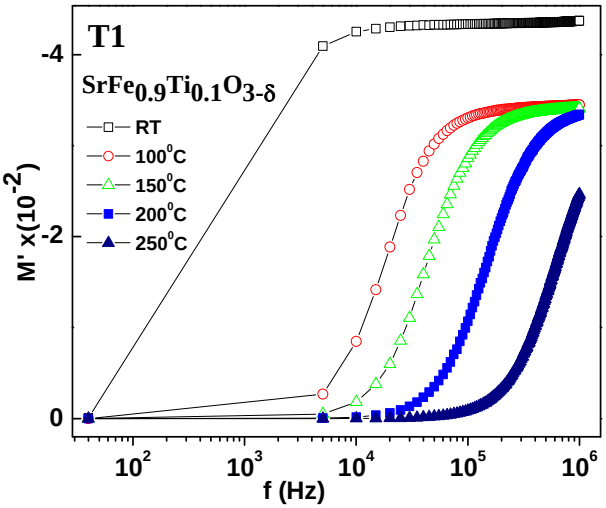

Figure 6.6(a). Real part of electrical modulus of T1

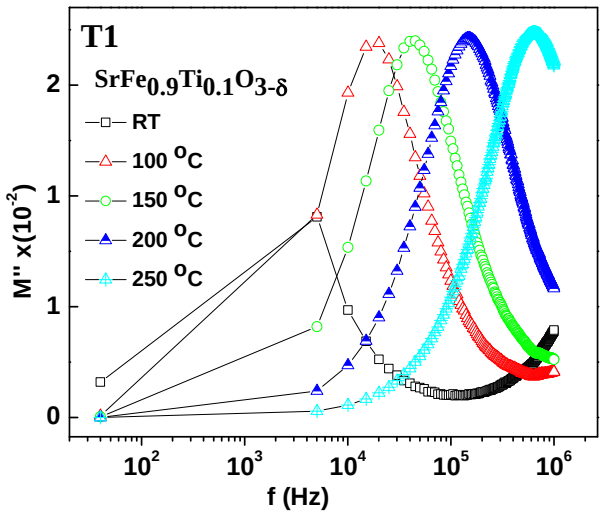

Figure 6.6(b). Imaginary part of electrical modulus of T1

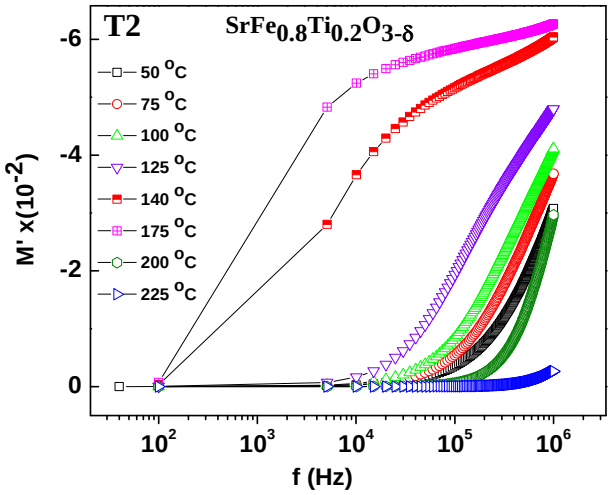

Figure 6.7(a) Real part of electrical modulus of T2.

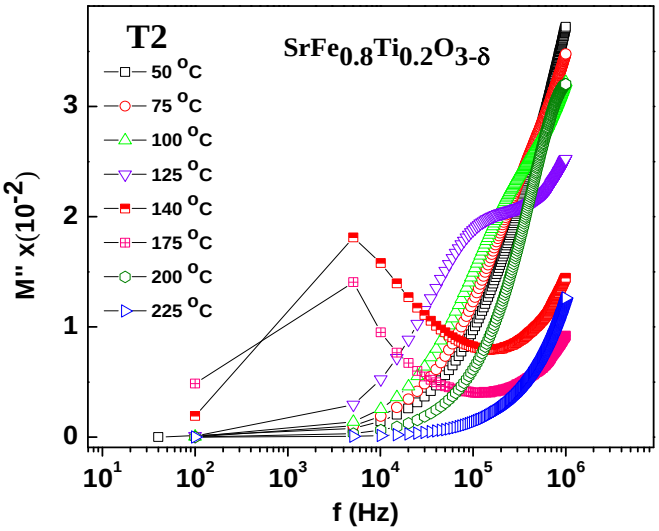

Figure 6.7(b). Imaginary part of electrical modulus of T2.

This clearly shows that the real and imaginary parts of the electrical modulus are also sensitive with change in the sign of the TCR and this is the first report which shows a clear correlation between the electrical modulus and the nature of TCR.

The activation energy calculated from the plot of $\ln\sigma_{dc}$ vs 1000/T is shown in Table 6.1. The activation energy in semiconductors generally depends on hopping distance, disorder and band gap. In this system with the stoichiometric $SrFeO_3$ has a cubic structure and is metallic. The undoped T0 has an oxygen stoichiometry of 2.86 and is tetragonal. The calculated activation energy is found to be 0.046 eV and with increase in Ti doping the bandgap increases. With increase in Ti doping, Ti occupies the Fe site and thereby there will be an additional disorder of Fe and Ti occupying different crystallographic sites apart from the oxygen vacancies present in the undoped system. The decrease in conductivity with increase in Ti doping can be seen from figure 6.2. For T1 there is not much difference in the conductivity but for T3 a drastic reduction in conductivity, which gets reflected in the increase in activation energy value to 0.83 eV. For the doped samples especially for T2 and T3 samples where PTCR is observed in the temperature range from RT to 175 °C the activation energy cannot be calculated. For the T2 sample, in most of the temperature range the conductivity is higher than T0. The variation of these conductivities with change in doping can be

Table 6.1 Activation energy is calculated from σ_{dc} plot.

System	Temp.range(˚C)	Ea (eV)
T-$SrFeTiO_{3-\delta}$ (T0)	150 – 375	0.4587
$SrFe_{0.9}Ti_{0.1}O_{3-\delta}$ (T1)	100-400	0.3817
$SrFe_{0.8}Ti_{0.2}O_{3-\delta}$ (T2)	225-375	0.5073
$SrFe_{0.7}Ti_{0.3}O_{3-\delta}$ (T3)	190-325	0.8313

Table 6.2 Bond length between Fe and O atoms of different crystallographic sites (named as Fe1, Fe2 and Fe3) calculated from neutron diffraction data (number in the brackets indicates number of bonds associated) Reproduced table 3.6

Systems	Fe1-O1(Å) (1)	Fe1-O2 (Å) (4)	Fe2-O2(Å) (2)	Fe2-O3(Å) (2)	Fe2-O4 (Å) (2)	Fe3-O4 (Å) (4)	Fe3-O5 (Å) (2)
T0	1.891	1.881	2.030	1.927	1.964	1.903	1.926
T1	1.959	1.917	1.955	1.942	1.952	1.919	1.939
T2	1.981	1.939	1.941	1.942	1.971	1.908	1.939
T3	1.942	1.925	1.959	1.942	1.942	1.942	1.942

understood in terms of the change in Fe-O distance. In general, the mobility of charge carriers and hence the conductivity will be higher if the Fe (Ti)-O-Fe and Ti-O-Ti(Fe) distance is smaller. From the detailed Rietveld refinement of the neutron data the different bond lengths of Fe1-O1, Fe1-O2, Fe2-O2, Fe2-O3, Fe2-O4 and Fe3-O4 and Fe3-O5 are estimated. Table 6.2 shows the different Fe-O bond lengths obtained from the neutron data analysis. It is found that with increase in Ti concentration initially except Fe2-O2 and Fe3-O4 all the bond lengths increase with increase in Ti up to 20% and with 30% Ti doping there is a decrease in these bond lengths. However, Fe2-O2 and Fe3-O4 have minimum bond lengths for T2 sample in comparison to T3. The higher conductivity observed in T2 sample may be due to the decrease in Fe2-O2 bond length. Apart from this, the site disorder leads to a distribution in band states which may lead to non systematic variation of the band gap resulting in variation of both the conductivity and activation energy. The temperature dependence of conductivity also cannot be described by the simple Arrhenius relation indicating the temperature dependence of the activation energy.

6.5 Conclusions

There are a few earlier reports on this system [21,29,31-38] but this is the first report where in a detailed impedance study is carried out in Ti doped $SrFeO_{3-\delta}$ stabilized in tetragonal structure. Alder.et.al [38] synthesized, high pressure oxygen annealed cubic and air annealed tetragonal structure samples but impedance measurements on tetragonal system are not reported. The present samples are well characterized by x-ray, neutron diffraction and the correct crystal structure is determined through an elaborate Rietveld data analysis. The occupation of the Fe and Ti at different crystallographic sites is established using the neutron data analysis and correlated with Mössbauer measurements. The composition of the samples is established through TGA combined with the compositional analysis using EDAX. The microstructure of the sample shows nanoparticles. The contribution from the grain boundaries arising due to the nanoparticles is inferred through Cole-Cole analysis, even though the expected low frequency semicircle is not seen due to the limited frequency range. 20% and 30 % doped Ti samples show PTCR from RT to 175°C at ambient pressure. Earlier studies report the observation of zero TCR at high temperature of 600 °C and at higher 10^4 Pa Oxygen pressures for samples with Fe concentration close 35% in cubic systems. The change over from NTCR to PTCR observed in this system at high concentration

of 70 to 80% may be related to the tetragonal structure of the present samples and also to the nanoparticle microstructure observed in these systems due to the high energy ball milling. The occurrence of PTCR is independently verified not only from the direct measured data of ac conductivity but also from the calculated dc conductivity obtained from the fits of the measured data. For the first time, the correlation between the electrical modulus and the nature of TCR is clearly brought out.

References

[1] R. von Helmolt, Physical Review Letter 71 , 2331 (1993).

[2] P.K. Gallagher, D.N.Buchanan and J.B. MacChesney, Journal of Chemical Physics 41, 2429 (1964).

[3] M.Uehra, S.Mori, C.H.Chen and S.W.Cheong , Nature (London) 399 560 (1999).

[4] V.V. Kharton, A.P.Viskup, A.V.Kovalevsky, J.R.Jurado, E.N.Naumovich , A.A.Vecher, J.R.Frade, Solid State Ionics,133, 57-65 (2000).

[5] Stephen J. Skinner and John A. Kilner, Materials today, 6, 30 (2003).

[6] A.V.Kovalevsky, V.V. Kharton, F.M.M.Snijkers, J.F.C.Cooymans, J.J.Luyten, F.M.B.Marques, Journal of Membrane Science , 30, 238(2007).

[7] J.R.Jurado , F.M.Figueiredo and J.R.Frade, Solid State Ionics ,122, 197 (1999).

[8] G. Sberveglieri, Sensors and Actuators B: Chemical , 23, 103-109 (1995).

[9] B.C.H Steele, Current Opinion in Solid State and Material Science, 1[5]684-691 (1996).

[10] Avner Rothschild and Harry L. Tuller, J.Electroceramics, 17, 1005 (2006).

[11] Ralf Moss, Wolfgang Menesklou, Hans-Jurgen Schreiner, Karl Heinz Hardtl , Sensors and Actuators B:Chemical , 67, 178(2000).

[12] M. L. Post, J. J. Tunney, D.Yang, X.Du, D.L. Singleton, Sensors and Actuators B:Chemical 59, 190 (1999).

[13] Wolfgang Menesklou, Hans-Jurgen Schreiner, Karl Heinz Hardtl and Ellen Ivers- Tiffee , Sensors and Actuators B:Chemical 59,184(1999).

[14] H. Falcon, J.A.Barbero, J.A.Alonso, M.J.Martinez Lope and J.L.G.Fierro, Chem.Mater 14, 2325 (2002).

[15] A.Nemudry, M.Weiss, I.Gainutdinov, V.Boldyrev and R.Schollhorn, Chem.Mater,10,2403 (1998).

[16] V.V. Kharton, Li Shuangbao, A.V.Kovalevsky and E.N.Naumovich , Solid State Ionics, 96, 141 (1997).

[17] V.V. Kharton , A.V.Kovalevsky, A.P.Viskup, F,M.Figueriredo, J.R.Frade, A.A.Yaremchenko and E.N.Naumovich, Solid State Ionics, 128, 117 (2000).

[18] William C. Maskell, Solid State Ionics, 134 ,43 (2000).

[19] L.H.Brixner, Materials Research Bulletin 3,299 (1968).

[20] G.M. Choi, H.L.Tuller and D.Goldschmidt, Physical Review, 34, 6972 (1986).

[21] Avner Rothschild, Wolfgang Menesklou, Harry L.Tuller, and Ellen Ivers-Tiffee, Chem.Mater.,18, 3651(2006).

[22]Naoaki Hayashi, Takahito Terashima and Mikio Taano, J.Mater.Chem, 11, 2235 (2001).

[23] Ana I. Becerro, Falko Langenhorst, Ross J. Angel, Stefan Marion, Catherine A.McCammon and Friedrich , Phys.Chem.Chem.Phys., 2, 3933 (2000).

[24] Chen Ang , Zhi Yu, Zhi Jing, P.Lunkenheimer and A.Loidl, Physical Review B 61, 3922 (2000).

[25] J.R.Jurado , M.T.Colomer and J.R.Frade, Solid State Ionics, 143 ,251(2001).

[26] Donhang Liu, Xi Yao and L.E.Cross, Journal of Applied Physics, 71,5115 (1992).

[27] N.F.Mott, E.A.Davis, Electronic Processes in Non-Crystalline Materials, Clarendon Press, Oxford (1979).

[28] Avner Rothschild, Scott J.Litzelman, Harry L.Tuller, Wolfgang Menesklou, Sensors and Actuators B:Chemical, 108, 223 (2005).

[29] J.Fleig, Solid State Ionics, 150, 181 (2002).

[30] Moti Ram and S. Chakrabarti, Journal of Alloys and Compounds, 462, 214 (2008).

[31] E.Mashkina, A.Magerl, J.Ollivier, M.Gobbels and F.Seifert, Physical Review B, 74, 214106 (2006).

[32] H.D. Zhou and J.B. Goodenough, Journal of Solid State Chemistry, 177, 1952 (2004).

[33] Hyun –Suk Kim, Lei Bi, Dong Hun Kim, Dae-Jin Yang, Yoon Jeong Choi, Jung Woo Lee, Yun Chang Park, Gerald F.Dionne and Caroline A.Ross, J.Mater.Chem., 21, 10364 (2011) .

[34] S.Srinath , M.Mahesh Kumar, K.Sahner, M.L.Post, M.Wickles, R.Moos and H.Srikanth ,Journal of Applied Physics, 99, 08S904(2006).

[35]. M.Vracar, A.Kuzmin, R.Merkle, J.Purans, E.A.Kotomin, J.Maier and O.Mathon, Physical Review, B 76, 174107 (2007).

[36] A.Wattiaux , L.Fournes, A.Demourgues, N.Bernaben, J.C.Grenier, and M.Pouchard, Solid State Communications, 77, 489 (1991).

[37] V.V. Kharton , A.P.Viskup, A.V.Kovalevsky, J.R.Jurado, E.N.Naumovich, A.AVecher, and J.R.Frade , Solid State Ionics 133, 57 (2000).

[38] Peter Alder and Sten Eriksson, Z.Anorg. Allg. Chem., 626, 118(2000).

CHAPTER 7

Summary and Scope of Future Work

7.1 Summary

In this thesis, we have investigated structural, magnetic, DC/AC transport properties of the parent compound tetragonal $SrFeO_{3-\delta}$ and Ti^{4+} doped $SrFe_{(1-x)}Ti_xO_{3-\delta}$ compounds. The crystal structure and the structural parameters are determined using an elaborate x-ray and neutron data analysis. The Ti doped samples for x up to 0.3 belong to the I4/mmm space group. The cell volume increases with increase in Ti doping, consistent with the increase in size of Ti^{4+} in comparison to the Fe^{4+}. ME studies together with neutron analysis on these tetragonal systems establishes that Fe occupies structurally and also magnetically three different sites.

In Ti doped compounds, low field AC susceptibility and dc magnetization studies do not show any signature of secondary phases present in this system; however in undoped $SrFeO_{3-\delta}$ minor secondary phase is present. Ti doping stabilizes the tetragonal structure. Observation of exchange bias confirms the presence of mixed valence in this system. Arrott plots on Ti doped systems show the absence of long range magnetic order. AC Susceptibility measurements show that there

is shift in susceptibility maxima in Ti doped systems. Volgel-Fulcher model fits indicates the presence of interacting spin clusters. Low temperature (below the peak temperature) neutron diffraction pattern not showing any additional Bragg's reflections in Ti doped system rules out the long range antiferromagnetic order. With 7T field cooled neutron diffraction data at different temperatures show no new peaks and also no change in intensities in any of the reflections in the Ti doped systems confirming the absence of long range magnetic ground state.

Transport measurements show metal to insulator like transition in all the systems. The measured temperature range of Ti doped sytems is far from the magnetic transition temperature and negative magneto-resistance is observed in all systems except T2. In T2 a small positive MR is observed. Three dimensional Variable Range Hopping model best fits the transport data in the paramagnetic state. Higher percentage of Ti doping increases the disorder in the system and localization length is decreasing which is reflected as higher resistivity.

Complex impedance measurements are carried out from room temperature to 450 °C in the frequency range of 40 Hz to 1 MHz. In all the systems Cole-Cole plot show the depressed single semi circle with respect to real part of Z axis indicates single relaxation and contribution of conductivity from grain boundaries only.

In T2 system change in temperature coefficient of resistance from positive to negative around 175 °C at ambient pressure is observed. The temperature dependence of dc conductivity (estimated from Cole-Cole analysis) show Arrhenius relation cannot be applicable indicating the temperature dependence of activation energy. For the first time, the correlation between the electrical modulus and the nature of temperature coefficient of resistance is clearly brought out.

7.2 Scope of Future Work

The work described in the present thesis can be used as an input to carry out further studies like XPS, Electron diffraction and other local probes which can help in better understanding of physical properties of these compounds. The origin of observed PTCR needs to be explored further.

Publications

Papers in Refereed Journals

1. ***Ferromagnetic Resonance in Cobalt nanoparticles***

A.Sendilkumar, Manasi Kasture, PitamberPatel, C.V.Ramama, B.L.V.Prasad, S.Srinath,

53rd DAE Solid State Physics Symposium (2008).

2. ***Investigation of magnetic anisotropy in Co nanoparticles using Ferromagnetic resonance technique***

A.Sendilkumar, Manasi Kasture,Pitamber Patel, C.V.Ramama, B.L.V.Prasad, S.Srinath

Journal of Physics Condensed Matter**:** Conference Series **200 (2010) 072088.**

3. ***Magnetic and ferroelectric properties of Fe doped SrTiO3 film***

A. Sendil Kumar, P. Suresh, M. Mahesh Kumar, H. Srikanth, M. L. Post, Kathy Sahner, Ralf Moos, S. Srinath

Journal of Physics Condensed Matter: Conference Series: **200 (2010) 092010.**

4. ***Synthesis of Nickel nanoparticles by electrodeposition***

A.Sendilkumar, S.P.Mathew ,S.Srinath

Proceedings of 54th DAE Solid State Physics Symposium (2009).

5. ***Magnetization and ESR study of $SrFeO_{3-\delta}$ systems***

A.Sendilkumar and S.Srinath

AIP Proceedings 978, 7354(2010)

6. ***Magnetism and Mossbauer Effect in Tetragonal $SrFeO_{3-\delta}$***

A.Sendilkumar, V.R.Reddy, M.Manivelraja P.D. Babu, A.Gupta and, S.Srinath

AIP Proceedings 1447, 1241-1242(2012**)**

7. ***Growth of crystalline $SrFeO_{2.5}$ thin films by Pulsed Laser Deposition***

A.Sendilkumar and S.Srinath (Under review)

8. ***Investigation of crystal structure and magnetism of $SrFe_{1-x}Ti_xO_{3-\delta}$ systems***

A.Sendilkumar, P.D. Babu, M.Manivelraja, V.R.Reddy, A.Gupta and S.Srinath (Under review)

9. ***AC Conductivity studies of $SrFe_{1-x}Ti_xO_{3-\delta}$***

A.Sendilkumar, P.D.Babu, K.C.James Raju and **S.Srinath** (Under review)

10. Observation of Cluster Spin glass behavior in Fe doped $SrFeO_{3-\delta}$ systems

A.Sendilkumar and S.Srinath (manuscript under preparation)

11. Magnetotransport properties and VRH conduction in $SrFe_{1-x}Ti_xO_{3-\delta}$ systems A.Sendilkumar and S.Srinath (manuscript under preparation)

Conferences/Symposiums Participated

1. 53rd DAE Solid State Physics Symposium (2008) held at BARC,

Mumbai

2. 54th DAE Solid State Physics Symposium (2009) held at Baroda University, Vadodara.
3. International Conference on Physics of Emerging Functional Materials (PEFM-2010), held at BARC, Mumbai.
4. International Conference on Magnetic Materials (ICMM2010) SINP, Kolkata.
5. International Conference on Materials for Advanced Technologies (ICMAT-2011), Suntec, Singapore.
6. 56th DAE Solid State Physics Symposium (2011) held at SRM University, Chennai.